DGK Veröffentlichungen der DGK

Ausschuss Geodäsie der Bayerischen Akademie der Wissenschaften

Reihe C | Dissertationen | Heft Nr. 923

Wen Huang

Enhancing GNSS by Integrating Low Earth Orbiters

München 2024

Bayerische Akademie der Wissenschaften

ISSN 0065-5325 ISBN 978-3-7696-5335-9

Diese Arbeit ist gleichzeitig veröffentlicht in:
DepositOnce – Forschungsdaten und Publikationen der Technischen Universität Berlin
https://doi.org/10.14279/depositonce-15101, Berlin 2022 und
GFZpublic – Publikationsdatenbank Helmholtz-Zentrum Potsdam Deutsches GeoForschungsZentrum GFZ
https://doi.org/10.48440/gfz.b103-21124, Potsdam 2022

DGK Veröffentlichungen der DGK

Ausschuss Geodäsie der Bayerischen Akademie der Wissenschaften

Reihe C Dissertationen Heft Nr. 923

Enhancing GNSS by Integrating Low Earth Orbiters

Von der Fakultät VI – Planen Bauen Umwelt
der Technischen Universität Berlin
zur Erlangung des akademischen Grades
Doktor-Ingenieur (Dr.-Ing.)
genehmigte Dissertation

von

Wen Huang, M.Sc.

München 2024

Bayerische Akademie der Wissenschaften

ISSN 0065-5325 ISBN 978-3-7696-5335-9

Diese Arbeit ist gleichzeitig veröffentlicht in:

DepositOnce – Forschungsdaten und Publikationen der Technischen Universität Berlin
https://doi.org/10.14279/depositonce-15101, Berlin 2022 und
GFZpublic – Publikationsdatenbank Helmholtz-Zentrum Potsdam Deutsches GeoForschungsZentrum GFZ
https://doi.org/10.48440/gfz.b103-21124, Potsdam 2022

Adresse der DGK:

Ausschuss Geodäsie der Bayerischen Akademie der Wissenschaften (DGK)

Alfons-Goppel-Straße 11 ● D – 80 539 München

Telefon +49 - 331 - 288 1685 ● E-Mail post@dgk.badw.de

http://www.dgk.badw.de

Prüfungskommission:

Vorsitzender: Prof. Dr.-Ing. Frank Neitzel

Referent: Prof. Dr. Dr. hc Harald Schuh

Korreferenten: Prof. Dr. Adrian Jäggi (Universität Bern)
Prof. Dr. Urs Hugentobler (TU München)

Tag der mündlichen Prüfung: 23.09.2021

ISSN 0065-5325 ISBN 978-3-7696-5335-9

Acknowledgements

Many people helped me in different aspects to make this study possible. First of all, I want to say thanks to Prof. Harald Schuh, who gave me the opportunity of doing this study at TU Berlin as his student. During my study, I benefited so much from his deep knowledge and rich experience in space geodesy. I am grateful for his guidance on my research directions, suggestions on my investigations, comments on my journal articles and thesis, and support on the funding applications. I am also very grateful to Benjamin Männel who is an expert in my topics, a patient teacher, a considerate working group leader, and a warm-hearted friend to me. Thanks a lot to his supervising and helps. I also thank Prof. Urs Hugentobler and Prof. Adrian Jäggi for being my examiners and giving valuable comments and suggestions on my study. Thanks a lot to my colleagues Andreas Brack, Pierre Sakic, and Gustavo Bento Mansur who shared their creative ideas, deep knowledge, and diverse experience with me. It is a pleasure to work with them in the shared but lovely office. I am also grateful to Thomas Nischan, Markus Brakde, and Andre Brandt for their help on technical problems and guidance on learning new skills. I want to especially acknowledge Prof. Maorong Ge for his support on the PANDA software and unreserved sharing of his rich experience on orbit determination and constructive suggestions on my studies. I also thank a lot to Zhigou Deng for his guidance, especially at the difficult beginning of my study, and his warm help on me and my family during the life in Germany. I am also grateful to Jungang Wang, Haibo Ge, Xuewen Gong, Susanne Glaser, Kyriakos Balidakis, Sadegh Modiri and many other colleagues at GFZ for solving my problems, answering my questions, giving me suggestions, and pointing out my shortcomings. I would like to thank my parents for their effort on my education and encouragement on my study. At last, I give my deepest thanks to my lovely wife Hui You for her support, understanding, meticulous care, and her love, and my beloved son Muxi Huang for being a joy during the thesis writing and pushing me to be better.

Additionally, I am grateful to be funded by Chinese Scholarship Council for this study.

Abstract

This study presents an enhancement to the Global Navigation Satellite Systems (GNSS) by integrating low Earth orbiters (LEOs) to a joint precise orbit determination (POD) processing. The Global Position System (GPS) operated by the United States is studied as a representative of all GNSS. The LEOs equipped with GNSS receivers supplement the receivers of the ground stations, especially for regions with a limited number of employed stations, which can be caused by various reasons. Due to the altitude and high velocity of LEOs, they not only contribute with additional observations, but also with a rapidly-changing observation geometry. Moreover, space-based observations have additional advantages over ground-based observations, e.g., signals are received without the impact of the troposphere. LEOs not only act as kinematic stations for GNSS satellites, but also bring additional orbit dynamics to the integrated system. The constraints caused by these orbit dynamics have an important impact on the determination of the orbits of the GNSS satellites and other parameters beyond that. In this thesis, the following topics are presented: 1) Background information and the basic principles related to the POD of GNSS satellites and LEOs, 2) the separated POD of GNSS satellites and LEOs, 3) the integrated POD, 4) the determination of the antenna phase center offsets (PCOs) of the GPS satellites and other geodetic parameters in the integrated POD.

The orbit modeling and processing configuration used in this study for GNSS satellites and LEOs are verified to be compatible with state-of-the-art studies by the separated POD. The orbits of the GNSS satellites and LEOs reach an accuracy of a few centimeters and are comparable with the state-of-art studies. A more efficient outlier detection method has been developed to improve the position determined by using pseudo-range observations. In the study about the enhancement of the GPS orbits by integrating LEOs, a 26-station ground network in a global and sparse distribution is supplemented by different subsets of seven LEOs including GRACE-A/B, OSTM/Jason-2, Jason-3 and, Swarm-A/B/C. A 34% improvement of the GPS orbit in 1D-mean RMS (from 37.5 mm to 23.9 mm) is achieved by including the seven LEOs. Both the number of space-based observations and the LEOs' orbital geometry affect the GPS orbits where the orbital geometry is shown to be more important. The estimated GPS PCOs are also improved by including LEOs. For the x- and y-components of the GPS PCOs, the formal error is reduced significantly due to the additional observations and expanded nadir angle coverage brought by the LEOs during the periods of large solar-elevation angle. The z-component of the GPS PCOs (z-PCO) are strongly correlated with the scale of the terrestrial reference frame. By introducing the orbit dynamics of the seven LEOs to the processing without applying a no-net-scale constraint, the correlation coefficients between the GPS z-PCOs and the scale are reduced from 0.85 to 0.30. Consequently, the GPS z-PCOs can be estimated independently from the a-priori scale and a purely GNSS-based scale can be

determined as well. A system-specific -25.5 cm offset of the GPS z-PCOs relative to the values offered by the International GNSS Service (IGS) is computed based on the seven-LEO-integrated solution. Another approach based on Galileo also solves this problem. The GPS satellites, multi-GNSS stations, and Galileo satellites with ground calibrated PCOs are processed jointly to calibrate the GPS z-PCOs and simultaneously determine a Galileo-based scale simultaneously. Based on the comparison and cross-check, a good agreement is shown between the LEO-based and Galileo-based methods. There is a slight improvement in the geocenter when including three Swarm satellites to the processing with about 80 ground stations over a half year.

Based on the analysis in theory and the results derived from real data, an obvious enhancement to various aspects of GNSS by the integrated processing with LEOs is shown. More LEOs equipped with GNSS receivers and carefully calibrated PCOs are expected for further missions or even the next generation of GNSS.

Zusammenfassung

In dieser Arbeit wird eine Verbesserung der globalen Satellitennavigationssysteme (GNSS) durch die Einbindung von Satelliten in niedrigen Erdumlaufbahnen (LEOs) in eine gemeinsame präzise Bahnbestimmung (POD) vorgestellt. Das von den Vereinigten Staaten betriebene Global Positioning System (GPS) wird stellvertretend für alle GNSS untersucht. Die mit GNSS-Empfängern ausgestatteten LEOs ergänzen die Empfänger der Bodenstationen, vor allem in Regionen, in denen aus verschiedenen Gründen nur wenige Stationen verfügbar sind. Aufgrund der Orbithöhe und schnellen Bewegung der LEOs tragen diese nicht nur mit zusätzlichen Beobachtungen bei, sondern auch mit einer sich schnell verändernden Beobachtungsgeometrie. Darüber hinaus haben weltraumgestützte Beobachtungen zusätzliche Vorteile gegenüber bodengestützten Beobachtungen, z. B. werden Signale ohne den Einfluss der Troposphäre empfangen. LEOs stellen nicht nur kinematische Stationen für die GNSS-Satelliten dar, sondern bringen auch eine zusätzliche Bahndynamik in das integrierte System ein. Die durch diese Bahndynamik gegebenen Beschränkungen sind sowohl für die Bahnbestimmung der GNSS Satelliten als auch für weitere Parameter äußerst relevant. In dieser Arbeit werden die folgenden Themen behandelt: 1) Hintergrundinformationen und Grundprinzipien der POD von GNSS-Satelliten und LEOs, 2) eine separate POD von GNSS-Satelliten und LEOs, 3) eine integrierte POD, 4) die Schätzung der Antennen-Phasenzentrumsversätze (PCOs) der GPS-Satelliten und anderer geodätischer Parameter in der integrierten POD.

Die separaten PODs bestätigen, dass die in dieser Studie verwendete Bahnmodellierungs- und Prozessierungskonfiguration der GNSS-Satelliten und LEOs mit dem aktuellen Stand der Forschung kompatibel ist. Die Bahnen der GNSS-Satelliten und LEOs erreichen eine Genauigkeit von wenigen Zentimetern. Es wurde eine effizientere Methode zur Erkennung von Ausreißern entwickelt, um die mit Hilfe von Pseudo-Range-Beobachtungen ermittelte Position zu verbessern. Ein Bodennetz mit 26 global dünn verteilten Stationen wird verwendet, um die Verbesserung der GPS-Bahnen durch die Integration von verschiedenen Teilgruppen der sieben LEOs GRACE-A/B, OSTM/Jason-2, Jason-3 und Swarm-A/B/C zu untersuchen. Bei der Einbeziehung aller sieben LEOs ergibt sich eine Verbesserung des 1D RMS Mittelwertes der GPS-Orbits von 34% (von 37,5 mm auf 23,9 mm). Sowohl die Anzahl der weltraumgestützten Beobachtungen als auch die Geometrie der Bahnen der LEOs beeinflussen die GPS-Bahnen, wobei die Orbitgeometrie sich als der wichtigere Faktor erweist. Die geschätzten GPS PCOs werden durch die Einbeziehung von LEOs ebenfalls verbessert. Der formale Fehler der x- und y-Komponenten der GPS PCOs wird durch die zusätzlichen Beobachtungen und die größere Abdeckung des Nadirwinkels, den die LEOs während Perioden eines großen Sonnenstandswinkels mit sich bringen, erheblich reduziert. Die z-Komponente der GPS PCOs (z-PCO) ist mit dem Maßstabsfaktor des terrestrischen Referenzrahmens

stark korreliert. Durch die Berücksichtigung der Bahndynamik der sieben LEOs in der Prozessierung werden ohne Fixierung des Maßstabes (d.h. ohne eine No-Net-Scale Bedingung) die Korrelationskoeffizienten zwischen den GPS z-PCOs und dem Maßstabsfaktor von 0,85 auf 0,30 reduziert. Folglich können zum einen die GPS z-PCOs unabhängig von einem externen Maßstab geschätzt werden und zum anderen kann ein rein GNSS-basierter Maßstabsfaktor bestimmt werden. Mit der integrierten Lösung mit sieben LEOs ergibt sich ein systemspezifischer Versatz der GPS z-PCOs von -25,5 cm relativ zu den vom International GNSS Service (IGS) veröffentlichten Werten. Ein anderer Ansatz basierend auf Galileo löst dieses Problem ebenfalls. Die GPS Satelliten, Multi-GNSS Bodenstationen und Galileo Satelliten mit bodenkalibrierten PCOs werden gemeinsam prozessiert, um die GPS z-PCOs zu kalibrieren und gleichzeitig einen Galileo-basierten Maßstabsfaktor zu bestimmen. Ein Vergleich zur Überprüfung zeigt eine hohe Übereinstimmung der LEO- und Galileo-basierten Methoden. Die Einbeziehung von drei Swarm Satelliten in eine Prozessierung mit etwa 80 Bodenstationen über ein halbes Jahr hinweg zeigt eine leichte Verbesserung des Geozentrums.

Auf der Grundlage der theoretischen Analyse und der aus realen Daten abgeleiteten Ergebnisse zeigt sich eine deutliche Verbesserung verschiedener Aspekte der GNSS durch die Integration von LEOs. Es ist zu erwarten, dass mehr LEOs, ausgestattet mit GNSS-Empfängern und sorgfältig kalibrierten PCOs, für künftige Missionen oder sogar die nächste GNSS Generation eingesetzt werden.

Contents

List of Figures

List of Tables

Introduction and Motivation

The third Newton's laws of motion say: '*When one body exerts a force on a second body, the second body simultaneously exerts a force equal in magnitude and opposite in direction on the first body.*' Besides its original meaning for physics, it can also be interpreted as that we should keep reverse thinking, make full use of data in a round way, and achieve a win-win for both sides. This principle applies to the two main space objects of this study: Global Navigation Satellite System (GNSS) and low Earth orbiter (LEO). GNSS is a well-developed technique that offers a powerful positioning function. The space segment of a GNSS consists of artificial satellites flying in medium-altitude Earth orbits (MEO, about 20,000 km altitude) and geosynchronous orbits (GSO, 37,000 km altitude). MEO satellites are used in the majority of the GNSS constellations as only the GNSS of China (BeiDou) and two regional navigation satellite systems (namely QZSS and NavIC) include satellites in GSO. LEOs are artificial satellites flying in the near-Earth space with a conventionally defined altitude lower than 2000 km. They have a wide range of applications, for example, scientific missions, communication, etc. According to the above-mentioned altitudes of different satellites, a schematic diagram about GNSS MEO satellites, LEOs, and the Earth is presented in Figure 1.1. Taking the most widely used Global Positioning System (GPS) as an example, the bore-sight angle of a GPS satellite, i.e., the angle between the sight direction and the nadir, to a terrestrial station at the limb of the Earth is about 14° (angle *n1*). For a LEO, the bore-sight angle *n2* of the GPS satellite is expanded

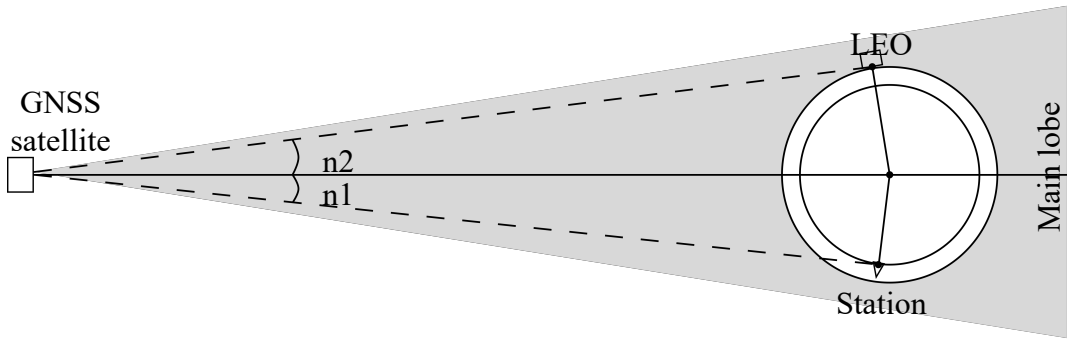

Figure 1.1: Schematic diagram of GPS visibility for LEOs and terrestrial stations; $n1$ and $n2$ are the GPS satellite bore-sight angles with respect to LEOs and terrestrial stations

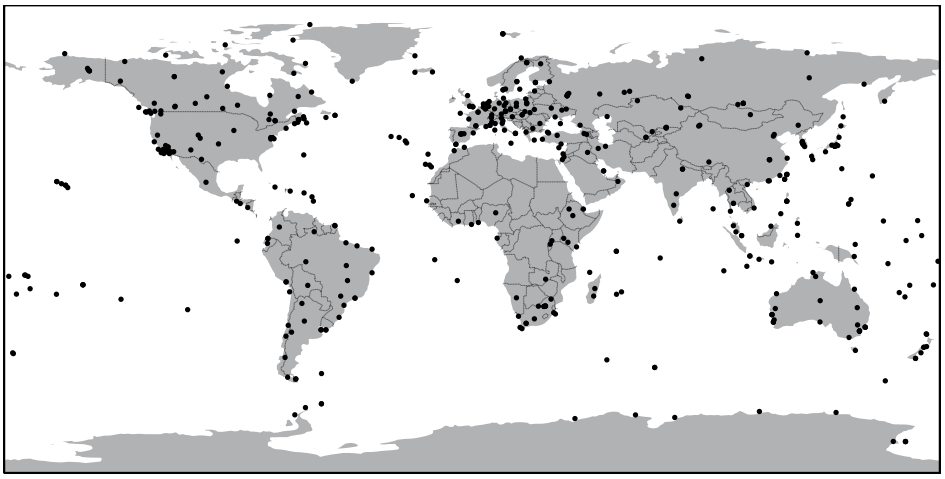

Figure 1.2: Available stations of IGS ground tracking network on 1st, June, 2020.

due to the higher altitude, for example, the OTSM/Jason-2 satellite, with an altitude of about 1,350 km, expands the bore-sight angle of GPS satellites to 17°. Both terrestrial receivers and LEO on-board receivers remain in the main lobe of the signal transmitted by GPS satellites (about 23° for GPS Block IIR and IIR-M). According to the signal strength pattern offered by Marquis and Reigh (2015), compared to the ground receiver at the limb of the Earth, the strength of the GPS signal received by a LEO flying at an altitude of 1,500 km (18° bore-sight angle) is reduced only by up to 5 dB. Therefore, LEOs can access very similar GPS services as terrestrial receivers. Most of the LEOs have GPS observations only. Due to the improved techniques and the requirements for further applications, multi-GNSS receivers are equipped to LEOs launched in recent years. The signal of other GNSS are additionally tracked by the LEOs with multi-GNSS receivers, for example, the FengYun-3C satellite observing BeiDou, the COSMIC-2 satellites observing the GNSS of Russia (GLONASS), and the Sentinel-6 satellite observing the GNSS of Europe (Galileo). Moreover, more and more LEOs were launched in recent years and operate in a common period. Consequently, a GNSS can be observed by more LEOs simultaneously.

In previous studies, the GNSS orbit and clock products are usually used as a priori information to determine the orbits of LEOs. However, LEOs can also contribute to the GNSS by integrated processing of GNSS satellites and LEOs. The integrated processing brings benefits in different aspects. Firstly, it improves the GNSS orbits determined by sparse ground tracking networks. The precise orbit determination (POD) of GNSS satellites is usually performed with ground-based observations by International GNSS Service (IGS, Johnston et al., 2018). The densely and globally distributed ground tracking network of IGS stations (see Figure 1.2) offers observations for a reliable and accurate GNSS POD. By highly constraining the coordinates of datum stations, the geodetic datum is fixed, including the origin, orientation, and unit length of the coordinate system, i.e.,

the terrestrial scale. The GNSS orbits are determined consistent with the defined geodetic datum. Despite the large and dense IGS tracking network in certain circumstances, depending on constellations and frequencies, one might be confronted with large regions without tracking stations, especially over major parts of oceans and Africa. Additionally, IGS stations could be unavailable because of various reasons as the IGS is a voluntary federation of over 300 self-funding agencies, universities, and research institutions in more than 100 countries[1]. The ground segments for controlling and monitoring the GNSS maintained by the providers are more reliable for their operation. However, the ground segments of all GNSS have limited stations and at least partly for political reasons have imperfect distributions. The GPS operated by the United States and Galileo operated by the European Union have globally but sparsely distributed ground segments including less than 20 tracking sites. Besides in major parts of oceans and Africa, GPS and Galileo have no control or monitor station in Russia, China, and the territory of each other. GLONASS and BeiDou only have ground segments located within the territory of their operating countries. Moreover, the ground segment of a GNSS may become partly unavailable for specific reasons, for instance, the detaching of two Galileo sensor stations due to the withdrawal of the United Kingdom from the European Union (Gutierrez, 2018). Besides the IGS stations which are publicly available, companies offering positioning services, e.g., Trimble, Leica, and Hi-Target, also use their own ground tracking stations to determine the GNSS orbits. However, they might still face the problem caused by the gaps in the networks. It is a potential way to supplement the limited ground tracking networks by integrating LEOs which are not restricted by geographic locations. Not only increasing the number of observations, but LEOs also bring additional benefits than terrestrial stations:

1. LEOs brings additional geometry by moving fast, supplementing the regions lacking terrestrial stations, and expanding the bore-sight angle of GNSS signals;

2. except for the shadowing effect on the LEOs with tilted antennas, LEOs have no signal blocking issue which has to be avoided in the setting up of a terrestrial station;

3. due to the altitude of LEOs, there is no signal delay caused by the neutral part of the atmosphere (mainly the troposphere with 13 km height in average) for LEOs;

4. as a consequence of benefits 2 and 3 and considering the near-field multi-path effect of LEOs, a lower elevation cut-off angle (e.g., 3°) than a terrestrial station (e.g., 7°) can be applied to LEOs.

Besides the improvements of GNSS orbits, the orbits of LEOs, the terrestrial reference frame (TRF), and the Earth gravity field, are also improved by the integrated processing

[1] https://www.igs.org/about/

when comparing with a two-step approach in which the orbits of GNSS satellites and LEOs are determined sequentially (Zhu et al., 2004). Benefiting from the different sensitivity of the ground and LEO on-board receivers to the estimates, the integrated or one-step processing is more consistent, homogeneous, and reliable for all the estimated parameters. Considering the overall improvement of GNSS and LEO orbits in the integrated processing, a future GNSS system named 'Kepler' consists of MEO satellites and LEOs is investigated to offer more reliable and accurate GNSS service (Giorgi et al., 2019). With optical frequency references, clocks onboard the satellites, and inter-satellite links, this new GNSS system requires only one station to maintain the alignment with Earth rotation, the synchronization to Universal Time Coordinate (UTC), and the capability of controlling the system. Considering the benefits brought by LEOs and the fast ongoing techniques, the first goal of this study is to investigate how much the LEOs can contribute to the GNSS satellite orbits in integrated processing.

The benefits of integrating LEOs are also reflected in the estimation of the transmitting point of the GPS satellite transmitter antenna. Usually, the phase center of the transmitting or receiving antenna of a satellite does not coincide with the center of mass of the satellite. The position of the phase center relative to the center of mass is represented by a mean offset vector (i.e., PCO) and nadir (and azimuth) dependent phase variations (PVs). It is a very important correction that should be considered in the orbit determination. However, the ground calibrated PCOs/PVs of the GPS satellites before the newest satellites of block GPS III are not available. Therefore, the PCOs of GPS satellites were estimated by constraining the ground stations (Schmid et al., 2007). Whether the estimation of the GPS PCOs can be improved by supplementing the ground stations with LEOs is the second question to be answered in this study.

The third goal of this study is the extension of the second one. When the ground stations are constrained to the a priori coordinates which contain the scale of the TRF determined by other geodetic techniques, the estimated PCOs in the Earth radial direction (z-PCOs) are not independent of other techniques. The influence will be propagated to the further GNSS-based solutions or products. Instead of constraining the scale of the network, the gravitation constraint on the LEOs brings an opportunity to estimate the GPS z-PCO purely based on the GNSS technique. Consequently, the GNSS-based terrestrial scale can be determined and may contribute to the realization of the International Terrestrial Reference Frame (ITRF). With the developing techniques and infrastructure, for example, the 'Kepler' system, this approach is promising to reach the 1 mm scale goal of the Global Geodetic Observing System (GGOS, Plag and Pearlman, 2009). There is another approach to solve this problem. Galileo has released its ground calibrated phase center information to the public. In joint processing of the GPS and Galileo, the z-PCO of GPS satellites can be determined by fixing the Galileo PCOs to

the ground calibrated values (Villiger et al., 2020). The independent z-PCOs of GPS satellites and the corresponding GNSS-based scale are determined by both methods in this study. The comparison and cross-check between the two methods are also performed via different scenarios.

After this introduction, this thesis is structured as follows.

In Chapter 2, some background knowledge related to this study is introduced. Firstly, with a focus on GNSS, some basic information about the four space geodetic techniques are given. Secondly, regarding orbital characteristics, data availability, and applications, various previous or active missions with LEOs are presented. Especially, the seven LEOs used in this study are introduced in detail. Moreover, a comparison between the MEO satellites and LEOs is given. Thirdly, the two important reference frames in space geodesy and the transformation between them are briefly expounded. Then the basic principle of kinematic and dynamic POD are described. The equations of GNSS observations, the processing configuration in this study, and the estimated parameters in different cases are given in the end.

Chapter 3 presents the results of the dynamic POD of GNSS satellites and LEOs separately. Before the discussion about POD solutions, an improved outlier detection method is presented. The determined orbit quality of GPS, GLONASS, Galileo, and LEOs is validated by internal and external comparison. The orbit of LEOs is validated by Satellite Laser Ranging (SLR) observations additionally.

In Chapter 4, the integrated POD of GNSS satellites and LEOs is investigated. Based on theoretical analysis and case studies using real data, the improvement of GPS satellite orbits by including LEOs is shown and discussed from different aspects.

The estimation of GPS PCOs, GNSS-based terrestrial scale, and the geocenter by two different approaches are performed and analyzed in Chapter 5. Firstly, a more detailed explanation about the existing limitations and strategies and related studies in the literature are discussed. Then the two methods of GPS z-PCO determinations are introduced. As an important issue for the study, a discussion on two different datum definitions is given. The algorithm and the comparison between the coordinate constraint and the free-network constraint are presented. Using real data, the GPS PCOs improvement by including LEOs are shown, the comparison and cross-check between the LEO-based and Galileo-based approaches are performed, the indirect geocenter results are discussed generally as an additional outcome.

The conclusions of this study and the outlook for further investigation are addressed in Chapter 6.

Background of precise orbit determination

Before the discussion of investigations, some important background knowledge is introduced in this section. In Section 2.1, the operational GNSS are introduced by focusing on their space segments and potential weaknesses in their ground segments. The other three space geodetic techniques are briefly introduced in Section 2.2. Section 2.3 contains the information of various LEO missions, including their orbital characteristics, the availability of on-board GNSS data, and a general comparison with GNSS MEO satellites. The seven LEOs used in this study are introduced with more details. As the key to connecting the orbit dynamics and the geodetic observations, the terrestrial and the celestial reference systems and the transformation between them are introduced in Section 2.4. The principle of kinematic and dynamic POD are discussed in Section 2.5. In section 2.6, several important aspects of POD processing, including the equations of GNSS observations, the linking between the observations and the motion equations, the processing configuration, and estimated parameters for different cases are presented.

2.1 Global and regional satellite navigation systems

The global navigation satellite system is a space geodetic technique that uses satellite constellation with global or regional coverage to provide autonomous positioning and navigation service. The GNSS technique is widely used in different applications, such as navigation and tracking, mapping and surveying, precise time reference, communication, geodetic science, etc. The satellites provide signals from space that transmit positioning and timing data to receivers in a way that the receiver positions can be computed simply based on the received data. Until now, there are three GNSS in full operation (GPS, GLONASS, and BeiDou), one GNSS scheduled to reach the full operation status soon (Galileo), and two regional navigation satellite systems (QZSS and NavIC) in operation. The GNSS satellites mainly transmit signals in L1 and L2 frequency bands. With the modernization of GPS and GLONASS and the newer systems, more signals in different frequencies are used. Different aspects including space and ground segment which are

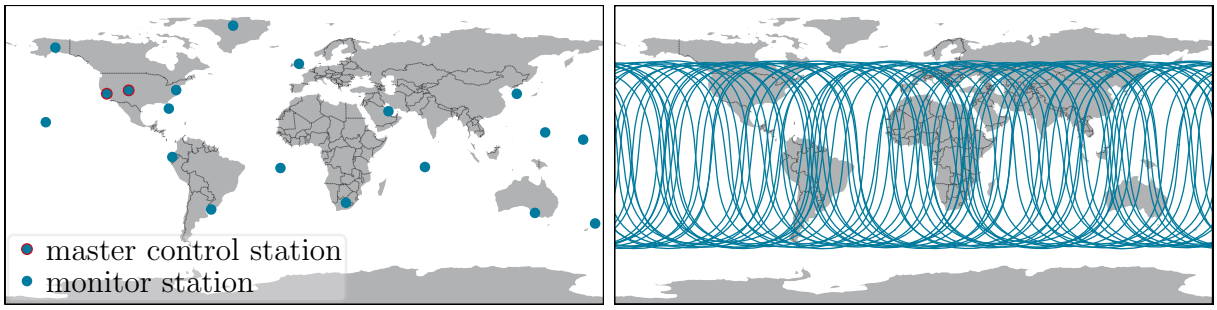

Figure 2.1: Master control stations and monitor stations of the GPS. (*left*)The monitor stations include Air Force Monitor Stations and National Geospatial-Intelligence Agency (NGA) Monitoring Stations. Ground tracks of the GPS satellites on day 37 of year 2021 (*right*)

relevant for the later POD investigations are discussed in the following.

GPS, officially Navstar GPS, is operated by the United States. It was declared to be the first fully operational GNSS in 1995. The nominal GPS constellation consists of 24 satellites in six MEO. In recent years, the constellation includes additional satellites (eight currently) in operation. Some of them are placed in the expanded slots of the nominal constellation. The others are placed close to the satellites that will be replaced soon. The ground track of the 32 operating satellites for day 180 of 2020 is plotted on the right panel of Figure 2.1. The approximate distribution of the master stations and monitor stations of GPS is shown on the left panel of Figure 2.1 based on the information offered by Malys (2012). Although nearly all of the IGS stations can obtain the signals from GPS satellites, the globally distributed monitoring network for the operation of the GPS is very sparse. Not only in the major parts of the oceans and Africa but also in China, Russia, and Europe, there is no available station for the GPS.

GLONASS is the second fully operational and global navigation satellite system. It was deployed by Russia to full operational capability with 24 MEO satellites in 1995. Although the number of active GLONASS satellites decreased to seven in 2001 due to insufficient replenishment, it achieved 24 satellites again in 2011 and keeps full operation onward. Compared to GPS, GLONASS satellites are distributed evenly within three orbit planes. The ground track of the whole constellation on day 180 of the year 2020 is shown on the right panel of Figure 2.2. The ground segment of GLONASS includes the system control center and the central clocks, the telemetry, tracking and command stations, and the up-link stations, one-way monitoring stations, and SLR stations. The whole ground segment is located within the Russian territory. The control center, monitor stations (13), and SLR stations (nine) are shown on the left panel of Figure 2.2. The locations of the stations are roughly offered by Menshikov and Solovyev (2006). To modernize and enhance GLONASS, a system for different correction and monitoring (SDCM) is under development. As reported by Stupak (2012) the SDCM will include 40 reference stations

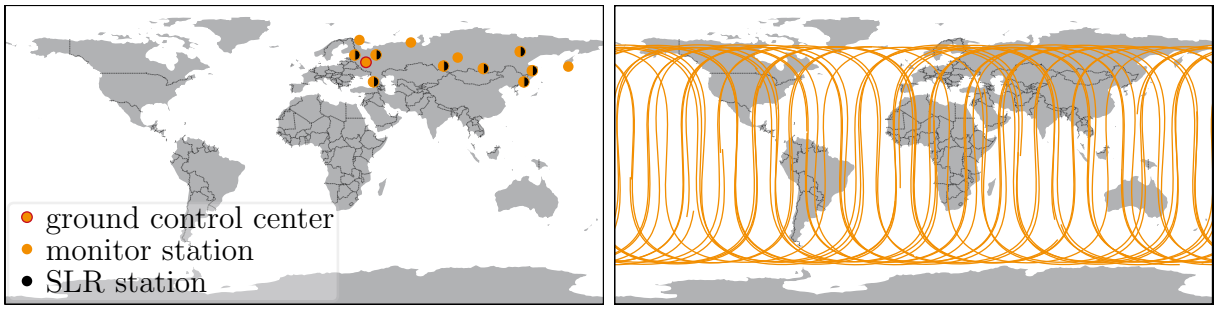

Figure 2.2: Ground control center, satellite laser ranging stations, and monitor stations of GLONASS. (*left*). Ground tracks of the GLONASS satellites on day 37 of year 2021 (*right*)

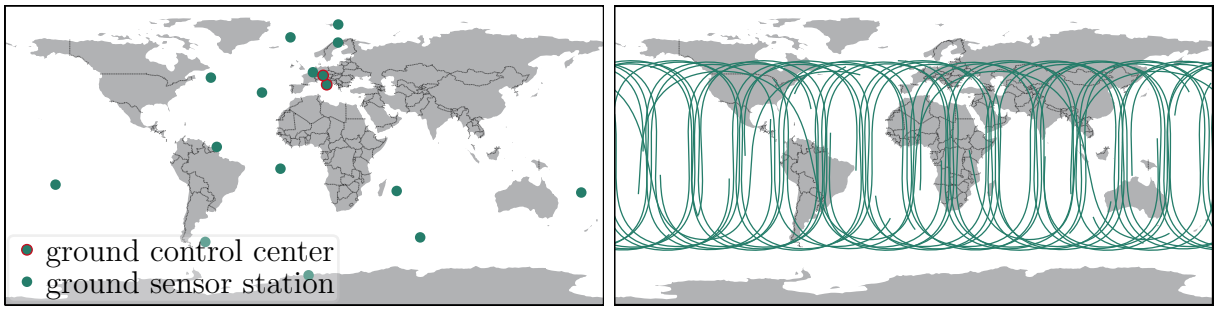

Figure 2.3: Ground control centers and ground sensor stations of Galileo. (*left*). Ground tracks of the Galileo satellites on day 180 of year 2020. (*right*)

within the Russian territory and 23 external stations to achieve global distribution. The signal frequency of GLONASS satellites is more special compared to the frequency of other GNSS. GLONASS has been transmitting frequency division multiply access (FDMA) signals on L1 and L2 since the first launch and introduced additional code division multiple access (CDMA) modulation signals on L3 to the replenishment satellites from 2011. The FDMA signals use a set of different channels for different signals which have about 0.5 MHz difference between neighboring channels while the other GNSS have a unique frequency in each band. The inherent inter-frequency biases do not allow the usually used ambiguity fixing for the phase observations. However, this problem will be solved by applying CDMA to L1, L2, and L3 signals for the future GLONASS-K2 satellites.

Galileo is the European GNSS which currently has a close to complete constellation. It has a normal constellation of 24 MEO satellites in three orbital planes and up to six spare satellites. The current constellation includes 24 satellites in operation. On the right panel of Figure 2.3, the ground tracks of the 24 operational satellites are plotted. Based on the available information [1], the distribution of the monitoring part of its ground segment is shown on the left panel of Figure 2.3. Similar to the GPS, the monitoring network of Galileo in a global and sparse distribution which has no stations in North America,

[1]https://www.esa.int/Applications/Navigation/Galileo_s_ground_control_segment_contracted_for_upgrade

(a) BeiDou (b) QZSS

Figure 2.4: Ground tracks of the constellations of BeiDou and QZSS on day 37 of year 2021

China, Russia, and Southern Africa.

The Chinese BeiDou system is a GNSS with a history of three generations. The three generations of BeiDou have different goals. The first generation (BeiDou-1) was an experimental regional system consists of four geosynchronous equatorial orbital (GEO) satellites (three in operation and one as backup) and very limited positioning functions within the territory of China. It was decommissioned in 2012. The second generation of BeiDou (BeiDou-2, formerly called COMPASS) was aimed to offer better positioning and navigation service over the Asia-Pacific region than BeiDou-1. Its constellation includes four MEO satellites, six GEO satellites, and six inclined geosynchronous orbital (IGSO) satellites. The first BeiDou-2 satellites were launched in 2007 and most of the BeiDou-2 satellites are still in operation together with the third generation (BeiDou-3). The constellation of BeiDou-3 was completed with reaching a global coverage in 2020. The geostationary satellites are on purpose to enhance the performance of BeiDou in the Asia-Pacific region. It includes 24 MEO satellites, three GEO satellites, and three IGSO satellites. The ground track of the BeiDou satellites (BeiDou-2 and BeiDou-3) is shown in Figure 2.4a. The 'dot' and '8' pattern trajectories of the GEO and IGSO satellites are obviously visible. Although the space segment of BeiDou is well developed, the ground segment of BeiDou is all located within Chinese territory (see Figure 10.22 in Teunissen and Montenbruck, 2017).

The two regional navigation systems have much fewer satellites in their constellations. The full name of NavIC is Navigation with Indian Constellation. The constellation of NavIC consists of three GEO satellites and four IGSO satellites. It is an independent system providing navigation service for India and surrounding regions with a transmitted signal in L5 and S frequency bands. Another regional navigation satellite system is the Japanese Quasi-Zenith Satellite System (QZSS). The name is a good explanation for its constellation which currently includes three satellites orbiting in highly inclined and slightly elliptical geosynchronous orbits (three more in the future) and one GEO satellite.

The ground track of the four operating satellites is shown in Figure 2.4b. To ensure the visibility of the satellites within the territory of Japan, the IGSO satellites have smaller inclination angles (43°±4°) than those of BeiDou (55°). This design leads to the asymmetrical '8' pattern of their ground track. Unlike the stand-alone NavIC, being compatible with GPS, QZSS provides highly precise and stable positioning services in the Asia-Oceania region.

The constellations of the four GNSS now have global coverage. However, the accuracy and reliability of their orbits and clocks are of central importance for positioning and navigation applications. Only based on their own ground segments, the orbit quality can only archive a limited level due to the limited observations and geometry. Although the ground segments are sufficient for the broadcast, much higher accuracy is required for the orbits by many applications. Including more and well-located ground stations (e.g., IGS stations) is the common way to improve the orbits. The integrated processing with LEOs is another solution that will be carefully discussed in Chapter 4. The characteristics of the LEOs are introduced in the next section.

The IGS is a voluntary federation of worldwide agencies dealing with the maintenance of ground stations, the collecting and processing of data, and the generating of products of all the GNSS. In general, the IGS is the highest-precision international civilian GNSS community. It has more than ten analysis centers (ACs) contributing to the products of orbits, clocks, ionosphere, station coordinates, etc. Due to the changes in the parameterization, orbit modeling, and observation modeling led by the development in methodology and techniques, the reprocessing starting at the observation level of the historical data has been done three times by the IGS ACs. The third IGS reprocessing campaign (repro3) is finished recently on February 10, 2021. The conventions and modeling for repro3 are mentioned in various places in this study.

2.2 Other space geodetic techniques

To study the shape, gravity, and rotation of the earth as well as their evolution in time of the earth, four space geodetic techniques are available. They are GNSS, SLR, Very Long Baseline Interferometry (VLBI), and Doppler Orbitography and Radiopositioning Integrated by Satellite (DORIS). They are all organized within the space geodetic services of the International Association of Geodesy (IAG) and entities within GGOS. They are all applied in various topics of the study about the solid Earth and its ocean and atmospheric systems. Some detailed information on the GNSS is given in the previous section. The other three techniques and the co-location of the different techniques are briefly introduced in the following.

SLR is a technique using short-pulse lasers, optical receivers, and timing electronics

to measure the two-way time of flight (distance consequently) from ground stations to retro-reflector arrays on Earth-orbiting satellites. Laser ranging activities are organized under the International Laser Ranging Service (ILRS) which provides global satellite and lunar laser ranging data and their derived products (Pearlman et al., 2002). VLBI technique measures the time difference between the arrival of a radio wavefront emitted by a distant quasar at two Earth-based antennas. As the time difference measurements are the precision level of a few picoseconds, the determined relative positions of the antennas achieve a precision of a few millimeters. The International VLBI Service (IVS) is the international collaboration of organizations that operate and support VLBI components (Schlüter and Behrend, 2007). Only SLR and VLBI contribute to the realization of the scale of ITRF until now. DORIS is a dual-frequency Doppler system that has been included as a host experiment on various space missions with LEOs, e.g., HY-2A and Jason-2. It is in the opposite configuration of a GNSS. The microwave signals based on the Doppler principle are transmitted by the ground-based radio beacons and received by the space-based receivers. The organization in charge of DORIS is the International DORISE Service (IVS, Willis et al., 2010). It has to be mentioned that GNSS, SLR, and DORIS as satellite techniques all can be used for the orbit determination if the corresponding sensors are installed on the spacecraft. VLBI is used for deep-space navigation. If suited equipment was installed on a satellite, VLBI can also contribute to its orbit determination.

In this study, SLR is mainly used for the orbit validation of LEOs and the scales of the TRF derived by VLBI and SLR are used to validate the GNSS-based solution. Therefore, the discussion about the four techniques is not going deeper. More detail introduction, comparison, and co-location of the four geodetic techniques are given by Coulot et al. (2007); Plag and Pearlman (2009); Männel (2016); Kodet et al. (2018).

2.3 Satellite missions in low Earth orbits

A LEO is an object orbiting the Earth in a low orbit which has a conventionally defined altitude lower than 2,000 km. Most of the artificial spacecraft are LEOs. Unlike the GNSS satellites which focus on offering the positioning service, LEOs are launched for many different purposes. Regarding the different purposes and usages, the LEOs fly in orbits with different altitudes (usually 250 to 1300 km) and inclinations (from equatorial to polar). The comparison between LEOs and MEO (limited to GNSS orbits) satellites is presented in Table 2.1. The period and velocity differences between the two orbiters are caused by their altitude difference which is larger than one order of magnitude. The daily ground track of a GPS satellite and a LEO is shown in Figure 2.5. The advantage of the LEOs are:

Table 2.1: Characteristics of LEOs and GNSS MEO satellites

	LEOs	MEO satellites (GNSS)
altitude	<2000 km	19,130∼23,222 km
orbit period	<128 minutes	11∼14 hours
velocity	6.90∼7.73 km/s[a]	3.67∼3.95 km/s
inclination	0° ∼180°	55° ∼65°
ground coverage	small	large
signal received by ground[b]	strong	weak
orbit stability	unstable	stable
cost	low	high

a. altitude-dependent
b. assuming the same transmission pow

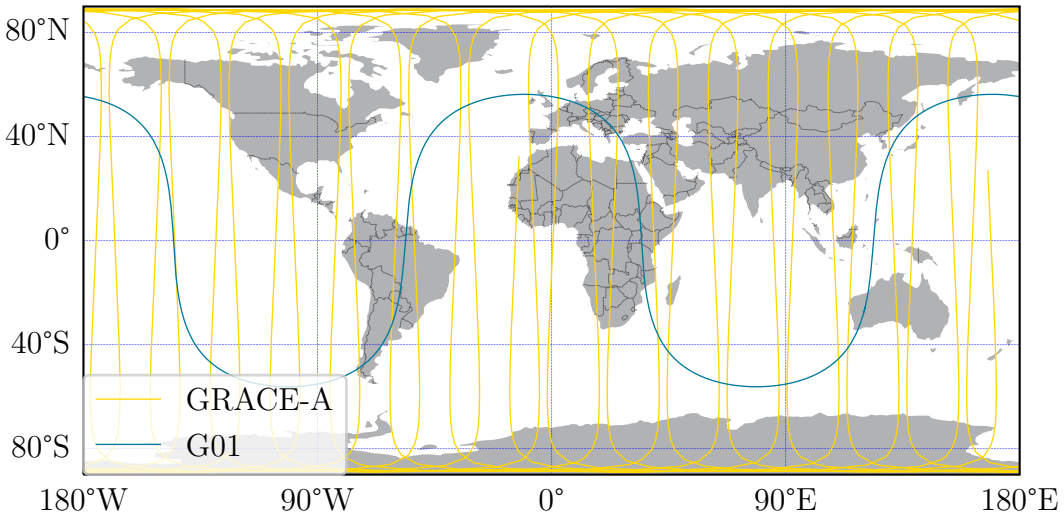

Figure 2.5: One-day ground track of GRACE-A and one GPS satellite (G01)

- the short period and low attitude of LEOs are suitable for the observing of the Earth in high resolution, e.g., the realization of the gravity field and geomagnetic field;
- the rapid movement of LEOs makes the observing geometry more diverse;
- with same transmission power, the signal from a LEO is much stronger than that of a MEO satellite to a ground receiver (Ramsey and Ziebart, 2020);
- LEOs have higher observing resolutions to the ground;
- the launch of a LEO is much easier and cheaper than that of a MEO satellite.

The disadvantages also exist due to the low altitude:

- the rapid movement of a LEO may introduce some problems to the data down-link when it flies over the receiving station in a few minutes, consequently more receiving stations are needed;

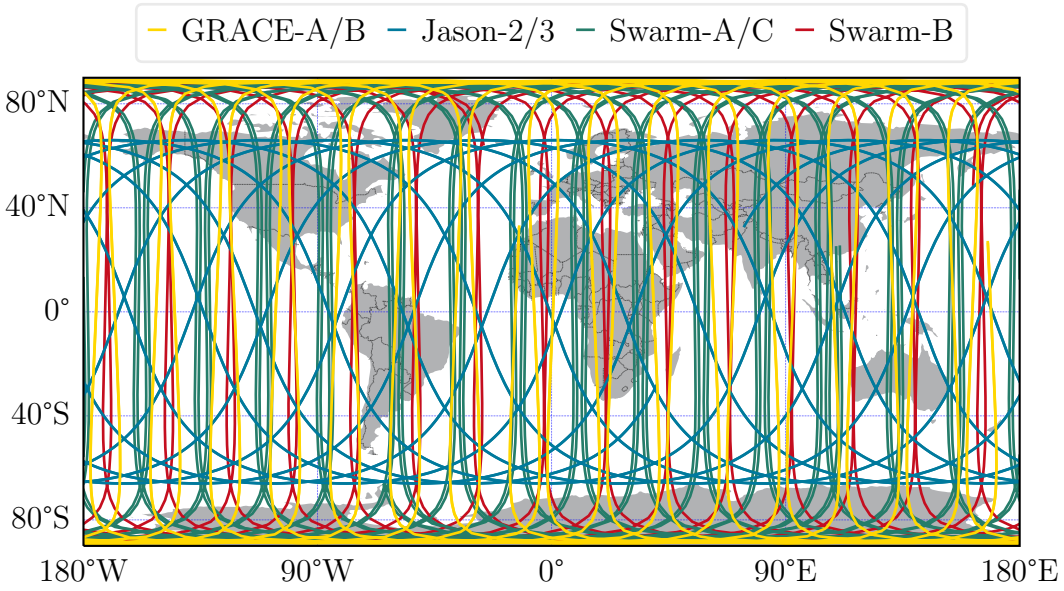

Figure 2.6: Ground tracks of the seven LEOs used in this study

- LEOs are visible to a very limited region on the ground, therefore more LEOs are required to achieve a global-coverage constellation;
- the much stronger atmosphere drag in low altitude leads to more complicated orbit modeling and more fuel usage for more maneuvers;
- related to the previous disadvantage the service life of a LEO is usually shorter than that of a MEO satellite.

In this study, the LEOs equipped with GNSS receivers, i.e., obtaining space-based GNSS observations, are focused. Seven of the LEOs are selected for these studies based on real data in Chapters 3, 4, and 5. They are selected due to their good availability of GPS observations, attitude data, precise orbit products, and antenna phase center corrections. Moreover, they are simultaneously available in the year 2016 and 2017, and this is very important for the studies about integrated processing. The seven used LEOs are introduced below and their daily ground tracks are presented in Figure 2.6. There are more LEOs fulfill the conditions mentioned above, for example, the satellites of the sentinel missions. However, they are not implemented into the software during my study. Moreover, there are other LEOs with available metadata and high quality data available in earlier and recent years, for example, CHAMP, COSMIC, GRACE-FO, etc. They will be included in future studies with long term processing.

The Gravity Recovery and Climate Experiment (GRACE) was a geodetic mission with the overall objective to obtain long-term data for global (high-resolution) models of the mean and the time-variable components of the Earth's gravity field (Tapley et al.,

2004). By mission definition, the two satellites were operating in the same orbital plane by one leading another with an along-track distance of about 170 km to 270 km. Their orbital plane was a nearly polar orbit with an 89° inclination and its initial altitude was about 500 km. As the two satellites were equipped with BlackJack GPS receivers, they obtained space-based GPS observations. The inter-satellite K-band observations between the two satellites contributed to the Earth gravity field determination. They were also equipped with a laser retro-reflector array and an accelerometer instrument. The twin satellites ended their service life in October 2017. In May 2019, another twin satellites were launched for the follow-on mission of GRACE (GRACE-FO, Kornfeld et al., 2019). The data of the twin satellites of the GRACE mission in 2016 are used in this study.

The Ocean Surface Topography Mission Jason-2 (OSTM/Jason-2) program contributed to the studies in oceanography, marine meteorology, seasonal prediction, and climate monitoring. Especially, the OSTM/Jason satellite made observations of ocean topography for investigations into sea-level change and the relationship between ocean circulation and climate change (Lambin et al., 2010). It was the third satellite in a series started in 1992 by the TOPEX/Poseidon mission (Fu et al., 1994) and continued by the Jason-1 mission (Ménard et al., 2003) launched in 2001. OSTM/Jason-2 flew in an inclined orbit plane (66°) with an altitude of about 1330 km which is higher than the other LEOs equipped with GNSS receivers. Besides the Turbo Rogue Space Receiver for obtaining GPS observations, OSTM/Jason-2 was also equipped with an altimeter, microwave radiometer, receiver for DORIS, and laser retro-reflector array. OSTM/Jason-2 ended its service life in October 2019. Its follow-on satellite Jason-3(Vaze et al., 2010) was launched in January 2016. Jason-3 flew about one minute behind OSTM/Jason-2 as a tandem mission in the first few months after launching, thus double coverage of the global ocean and improved data resolution were achieved. Due to the aging of OSTM/Jason-2, the decommissioned spacecraft was then moved from the shared orbit to a 27 km-lower orbit. The move is designed to safeguard the orbit for Jason-3 and its successor Sentinel-6 Michael Freilich (formerly Jason-CS A) which was launched in November 2020 and obtaining GPS and Galileo observations. The data of OSTM/Jason-2 and Jason-3, especially when they were sharing the orbit in 2016, is used in this study.

Swarm is a mission designed for the study of geomagnetic field (Friis-Christensen et al., 2006). The constellation consists of three satellites (Swarm-A/B/C) equipped with a vector field magnetometer, an absolute scalar magnetometer, an electric field instrument, an accelerometer, a laser range reflector, and a dual-frequency GPS receiver. Swarm-A and Swarm-C fly side-by-side (20 to 200 km cross-track separation) as a pair at an initial altitude of 470 km and 87.35° inclination angle. Swarm-B flies in a higher orbit (510 km initial altitude) with 87.75° inclination. Therefore, the orbital plan of Swarm-B drifts relative to that of the Swarm-A/C by about 25° per year (Sieg and Diekmann, 2016;

Table 2.2: Orbit information of LEOs with GNSS observations. SP3c codes are maintained by the International Association for Geodesy to identify the spacecraft.

LEO	altitude [km]	inclination [◦]	launch mass [kg]	objective	SP3c
TOPEX/Poseidon	1350	66	2400	oceanography	L01
GPS/MET	715	70	74	remote sensing	L02
GFO	784	108	416	oceanography	L03
Ørsted	630-850	96	61	geomagnetic	L04
CHAMP	300-500	87	500	geoscience	L06
Jason-1	1336	66	500	oceanography	L08
GRACE	483-508	89	487	gravity field	L09
ICESat	586-594	94	970	remote sensing	L11
SAC-C	705	98	485	geoscience	L07
COSMIC	500	72	70	meteorology	L21-L26
MetOP	817	99	4093	meteorology	L14
TerraSAR-X	514	97	1230	radar imaging	L13
OSTM/Jason-2	1336	66	510	oceanography	L27
GOCE	255	97	1077	gravity field	L15
C/NOFS	405-800	13	384	ionospheric	n/a
Swarm-A/C	460	87	468	geomagnetic	L47
Swarm-B	530	88	468	geomagnetic	L48
Sentinel-1	693	98	2300	radar imaging	L70/71
KOMPSAT-5	550	98	1400	remote sensing	n/a
Sentinel-2	786	99	1140	optical imaging	L72/73
Sentinel-3	814	99	1150	optical imaging	L74/75
Jason-3	1336	66	553	oceanography	L39
TanDEM-X	515	97	1340	radar imaging	L20
Sentinel-5P	834	99	900	atmospheric	n/a
PAZ	508	97	1341	radar imaging	L66
GRACE-FO	482-506	89	600	gravity field	L64
COSMIC-2	520-550	72	300	meteorology	L76-L87
Sentinel-6A	1320	66	1362	oceanography	n/a

Montenbruck et al., 2018). The space-based GPS data of Swarm-A/B/C in 2016 and 2019 is used in this study.

Besides the seven LEOs introduced above, many other LEOs were or are obtaining space-based GNSS observations. In Table 2.2, some orbit information and the main objective of 26 previous or active missions are listed. These LEO missions are designed for various purposes, for example, the studies on oceanography, geomagnetic, gravity field of the Earth, radar imaging, etc. Their altitudes, orbital inclination, and launch mass vary from 255 km to 1336 km, 13°to 108 °, and 61 kg to 4093 kg, respectively. The SP3c code is listed in the spacecraft ID correspondence table for orbit exchange files maintained

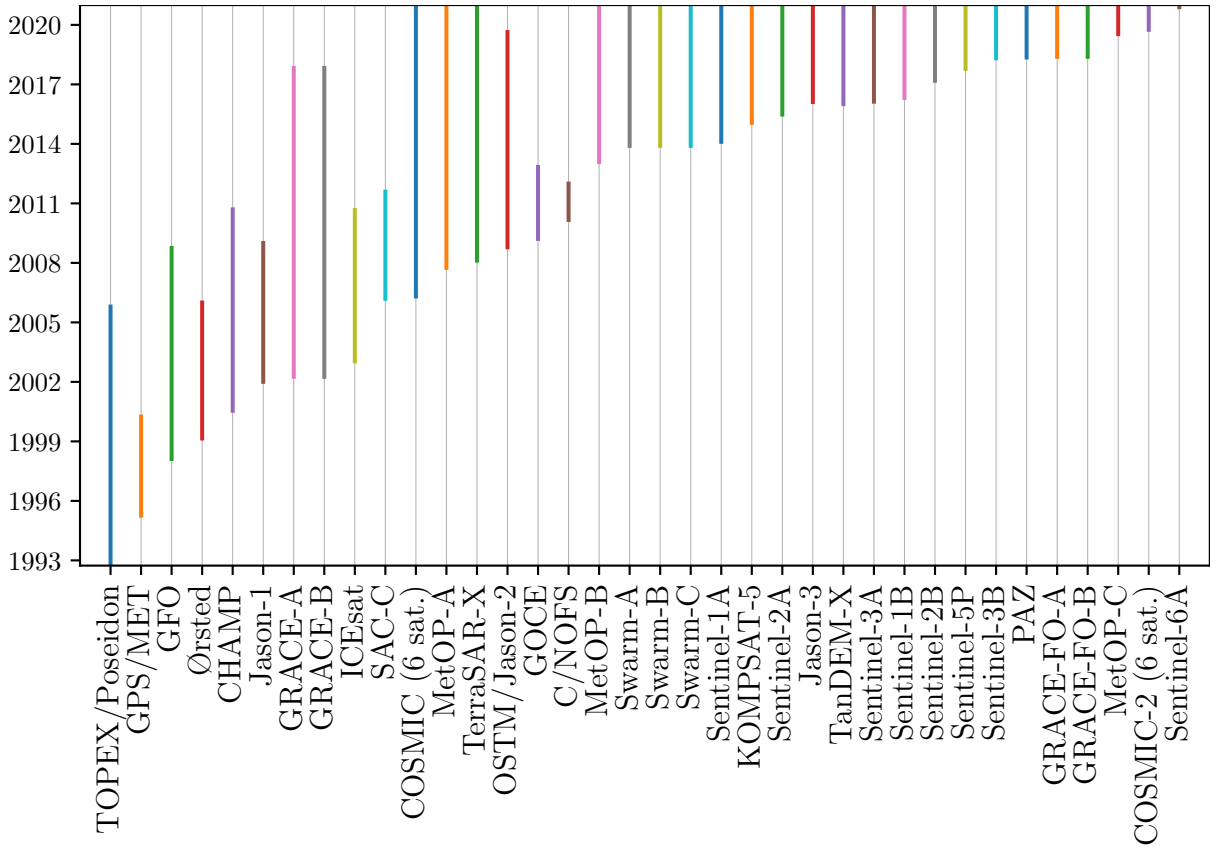

Figure 2.7: Long-term status of the space-based data of the LEOs.

by IAG.[2] The letter 'L' stands for non-GNSS spacecraft. The SP3c codes of all GNSS satellites are identical to the codes used in the RINEX data and navigation message files. New missions can submit code requests to the IAG and then be approved by IGS, ILRS, and IDS. According to my study experience, the SP3c code is not commonly used, for example, missing from the header of their observation file or scientific orbit file. However, in the consideration for processing, the SP3c code is useful to identify the different LEOs in joint processing. Therefore I implemented the SP3c code in the software used for this study and highly recommend it.

The space-based GNSS observations mainly contribute to the precise orbit determination of the LEOs. The LEOs can also contribute to the GNSS as a rapid-moving station, especially considering the continuity and simultaneous availability of the space-based GNSS data shown in figure 2.7. In recent years, more and more LEOs are equipped with GNSS receivers and operating simultaneously. It makes the joint processing of the GPS and multi-LEOs based on real data come true in this study.

[2]https://cddis.gsfc.nasa.gov/Techniques/sp3c_satlist.html

2.4 Reference systems and frames

There are two types of reference systems commonly used in the study of astronomy, geodesy, physical geodesy, etc. They are International Celestial Reference System (ICRS) and International Terrestrial Reference System (ITRS). Both systems are defined based on the purpose that the geodetic observations can be represented as functions of parameters. These reference systems are realized by a set of coordinates of markers, i.e., reference frames. The above-mentioned reference systems and frames are introduced in this chapter.

To valid Newton's laws of motion, the motion of objects should be described in an inertial reference system. To describe the motion of the Earth, planets, and artificial spacecraft, an inertial reference system can be realized by observing radio sources outside the Milky Way galaxy, i.e., extragalactic objects. Due to the distance of the extragalactic radio sources, they are apparently stationary based on our current technology. Therefore, the inertial system is space-fixed. The barycentric celestial reference system (BCRS) is a typical inertial system with the center of mass of the solar system used as its origin. The ICRS (Feissel and Mignard, 1998) is the conventional version of the BCRS. The axes of the ICRS are defined by the directions of the extragalactic radio sources. ICRS is mainly used for objects outside the gravitational vicinity of Earth. More details are given by the IERS 2010 Conventions (Petit and Luzum, 2010). The ICRS is represented by the International Celestial Reference Frame (ICRF) which is realized by VLBI estimates of equatorial coordinates of a set of extragalactic compact radio sources (Ma et al., 1998). The latest update is the third realization (ICRF3, Charlot et al., 2020). The Geocentric Celestial Reference System (GCRS) is used to describe the position and motion of near-earth objects, e.g., artificial spacecraft, which are orbiting around the Earth (Nothnagel et al., 2010). The origin of GCRS is shifted from the Barycenter to Earth's center which is the center of mass of Earth including the mass of the solid Earth, the cryosphere, the ocean, the continental hydrosphere, and the Earth's atmosphere. The orientation of the GCRS coincides with that of the BCRS. However, due to the gravitational attractions of the Sun, the Moon, and the planets the GCRS is not absolute inertial. The effect of Earth's revolution and the geodetic precession and nutation should be taken into account when describing the motion of objects in GCRS. The dynamic equations of motion of GNSS satellites and LEOs are generated under the ICRF.

A Terrestrial Reference System (TRS) is a spatial reference system co-rotating with the Earth. The positions of points attached to the solid surface of the Earth only have small variations with time. The variations are caused by geophysical effects, for example, tectonic or tidal deformations. This reference system is obviously accelerated, i.e., not inertial. According to the characteristics of the TRS, it is a well-defined system to describe positions or small movements of objects on the Earth's surface. The ITRS

is the conventional version of the TRS. According to the IERS conventions (Petit and Luzum, 2010), the ITRS is defined as below. It is a geocentric system with the origin in the center of mass of the Earth. The unit of length of the ITRS is meter. The time of the ITRS consistent with the geocentric coordinate time (TCG). The orientation of the ITRS is constrained by applying a no-net-rotation condition to the horizontal Earth surface. The ITRF is the most important realization of the ITRS. It includes the coordinates and velocities of a set of selected stations which are computed by combining the solutions of four space geodetic techniques, including VLBI, SLR, GNSS and, DORIS. The latest update is ITRF2014 (Altamimi et al., 2016). There are another two TRF, namely DTRF2014 (Seitz et al., 2016) and JTRF2014 (Abbondanza et al., 2017), released by the German Geodetic Research Institute in Technical University of Munich (DFGI-TUM) and the Jet Propulsion Laboratory (JPL), respectively.

The coordinates in the two systems are normally connected by geodetic observations, for example, the inertial orbits of GNSS satellites and the coordinates of ground stations are linked by the ground-based GNSS observations. Therefore, a transformation between the TRS and CRS is important for the processing including the coordinates in terrestrial and inertial systems. The transformation from the TRS to the CRS and its reverse processing can be applied in two approach. The first one is the so-called equinox method which uses the Greenwich apparent sidereal time (GAST) for the angle of Earth's rotation and the traditional precession and nutation series, given by

$$\boldsymbol{r}_{\mathrm{TRS}} = \mathbf{W}^{\top}\mathbf{R}_3(\mathrm{GAST})\mathbf{NPB}\boldsymbol{r}_{\mathrm{CRS}} \tag{2.1}$$

$$\boldsymbol{r}_{\mathrm{CRS}} = \mathbf{B}^{\top}\mathbf{P}^{\top}\mathbf{N}^{\top}\mathbf{R}_3^{\top}(\mathrm{GAST})\mathbf{W}r_{\mathrm{TRS}} \tag{2.2}$$

where $\boldsymbol{r}_{\mathrm{TRS}}$ and $\boldsymbol{r}_{\mathrm{CRS}}$ are the vector of coordinates in TRS and CRS, $\mathbf{W}$ is the polar motion matrix,$\mathbf{R}_3$ is the elementary rotation matrix about the z-axis, $\mathbf{N}$ and $\mathbf{P}$ are transformation matrices of nutation and precession, and $\mathbf{B}$ is a small rotation to account for the bias of the frame. Based on Celestial Intermediate Origin (CIO), IAG resolved another approach by defining the origin for right ascension in the intermediate celestial system by the non-rotating origin. The nutation and precession transformations are combined with the Earth rotation in the CIO-based approach, given by

$$\boldsymbol{r}_{\mathrm{TRS}} = \mathbf{W}^{\top}\mathbf{R}_3(ERA)\mathbf{Q}^{\top}\boldsymbol{r}_{\mathrm{CRS}} \tag{2.3}$$

$$\boldsymbol{r}_{\mathrm{CRS}} = \mathbf{Q}\mathbf{R}_3^{\top}(ERA)\mathbf{W}\boldsymbol{r}_{\mathrm{TRS}} \tag{2.4}$$

where ERA means Earth rotation angle, $\mathbf{Q}$ is the combined rotation matrix and defined by IERS Conventions 2003 as the rotation from the system of the instantaneous pole and origin to the reference system. More details about the transformations can be found in

many literatures. The CIO-based approach is applied to the processing in this study.

2.5 Precise orbit determination technique

Precisely determined orbits are the prerequisites for further applications of the satellites, especially for the applications in geodesy and other earth science. Based on the ground- and space-based observations of geodetic observing techniques, there are two main POD approaches. The first one is kinematic POD which is based only on the geometry information of observations. Another approach is called dynamic POD as the forces acting on the satellites and the physical properties of the satellites are modeled to describe the motion of the satellites. An enhanced approach of the dynamic POD is achieved by introducing empirical parameters or stochastic pulses to reduce the impact of deficiencies modeling on the orbits. This enhanced approach is called reduced dynamic POD and is mainly applied to LEOs due to the larger and more variable perturbations.

The POD technique has been deeply studied during the past decades. The detailed introduction of POD can be found in previous studies (Montenbruck and Gill, 2000; Bock, 2003; Jäggi et al., 2007). The kinematic POD and (reduced) dynamic POD are briefly introduced in Sections 2.5.1 and 2.5.2. Although the observations of GNSS, SLR, and DORIS are used in POD (Luthcke et al., 2003; Bury et al., 2020), only GNSS observations are used for POD in this study, and SLR observations will be used for external validation.

2.5.1 Kinematic POD

If a station, a vehicle, or a spacecraft is equipped with a GNSS receiver, its epoch-wise position can be computed based on the obtained GNSS code and phase observations. The kinematic positioning of artificial satellites is also called kinematic POD. It is mainly applied to LEOs. It can also be applied to GNSS satellites by fixing the coordinates of ground stations, but the positioning quality is much worse than that of LEOs and ground stations (Švehla and Rothacher, 2005a) caused by the correlation between radial position and clock due to the small nadir angles of the observations. In kinematic POD, additional information about the forces acting on the object is not needed. Therefore, the precision of the solution is only based on the precision of the observations, their geometry, and the GNSS orbit and clock products used. The processing is done in an Earth-fixed frame. As there are three coordinates and one receiver clock unknowns in each epoch, the observations for at least four GNSS satellites are required to derive a solution. As the kinematic orbit is discrete due to the epoch-wise solution, the position of the object at a non-observation moment needs to be interpolated. The processing includes three steps in general. Firstly, by using Bancroft method (Bancroft, 1985) or code-observation-based

positioning, i.e., single point positioning (SPP), or both, the initial positions (accuracy in meters) of the satellite is computed without any a priori information. Secondly, after the outliers detection and editing of the observations based on the initial positions, the orbit is updated by another round of SPP. This step is performed repeatedly to clean the observations and update the results. In the last step, the code and phase observations are used together. The time-difference phase observations are generated to solve the phase ambiguities. The final orbit is determined by combining the positions derived by code observations and the position differences (accuracy in mm to cm) derived by phase observations. The detailed introduction of the above-mentioned approach is given by Bock (2003); Chen (2007). As the focus of this study is on the dynamic POD that will be introduced below, more detailed information and discussion about kinematic POD are not given. Švehla and Rothacher (2003) compared the kinematic and dynamic POD performance on LEOs in detail. Moreover, the kinematic POD of LEOs are also applied to determine the gravity field of the Earth which is another hot topic (Švehla and Rothacher, 2005b; Jäggi et al., 2016; Ren and Schön, 2018).

2.5.2 Dynamic POD

The dynamic POD is the common approach for LEOs and GNSS satellites. Besides making full use of the GNSS observations, the motion of the satellites which is led by different dynamic forces is modeled as accurately as possible. The motion of a satellite consists of the Keplerian motion due to the gravitational force originating from a central body (two-body problem) and the perturbing accelerations due to different reasons. Accordingly, the equation of the motion in the inertial reference system is given by

$$\ddot{\boldsymbol{r}} = -\frac{GM\boldsymbol{r}}{R^3} + \boldsymbol{a}(\boldsymbol{r}, \dot{\boldsymbol{r}}, t, p_1, p_2, ..., p_i) \tag{2.5}$$

where $\boldsymbol{r}$, $\dot{\boldsymbol{r}}$, and $\ddot{\boldsymbol{r}}$ are the vectors of the position, the velocity, and the total acceleration of the satellite at time t, R is the distance between the satellite and the central body (the Earth), G is the universal constant of gravity and M is the mass of the Earth, $\boldsymbol{a}$ denotes the perturbing accelerations which is a function about the satellite state ($\boldsymbol{r}$ and $\dot{\boldsymbol{r}}$,), the time, and the modeling parameters $(p_1, p_2, ..., p_i)$. The perturbations include gravitational and non-gravitational ones. The gravitational perturbations are caused by gravity field issues including the oblateness of the Earth, the attraction of Sun, Moon, and planets (i.e., N-body perturbation), the tides of solid Earth, ocean, and pole, and relativity issue. The non-gravitational perturbations are caused by the atmosphere drag, the solar radiation pressure, the Earth radiation pressure, etc. The above-mentioned perturbations are modeled based on nature physics. The modeling equations are given by many previous studies (Rothacher, 1992; Bock, 2003; Chen, 2007; Männel, 2016). A

Table 2.3: Orbit modeling for GNSS satellites and LEOs in this study

Perturbations	Models applied in this study
Gravitational	
Earth gravity field	EIGEN-GRACE02S (Reigber et al., 2005); 12×12 for GNSS satellites; 120×120 for LEOs
N-body perturbation	JPL DE405 (Standish, 1998)
Relativity	IERS conventions 2010 (Petit and Luzum, 2010)
Solid Earth, pole tide	IERS conventions 2010
Ocean tide	FES2004 (Lyard et al., 2006)
Non-gravitational	
Atmospheric drag	DTM94 (Berger et al., 1998); only applied to LEOs
Solar radiation pressure	reduced ECOM (Springer et al., 1999) for GPS and GLONASS; a priori box-wing model + reduced ECOM (Montenbruck et al., 2015) for Galileo; box-wing macro models (Marshall et al., 1992) for LEOs
Earth albedo radiation	analytical, box-wing model; only applied to GNSS

general introduction of the perturbations and the dynamic models applied in this study (listed in Table 2.3) is given below.

The gravity field of the Earth is usually represented by spherical harmonic functions. The modeled gravity field consists of a set of the estimated coefficients of the function. There are 176 available static gravity field models from 1966 to now[3]. The models are estimated based on different data sources including altimetry data, satellite-based data, ground-based data, and topography. They also have different maximum degrees and orders and time varying components. EIGEN-GRACE02S as the default model in PANDA software is applied for the POD in this study. It is up to degree and order 150. Although it is not the newest model, it is based on the data of the GRACE mission, thus it is sufficient for the POD of GNSS satellites and LEOs. Depending on the attitude of the satellites, different gravity field coefficients have to be considered. Bock (2003) concludes that the Earth gravity field has to be up to degree and order 8×8 for GNSS satellites and up to degree and order 120×120 for LEOs. Therefore, degree and order 12×12 are applied for GNSS satellites, and 120×120 is applied for LEOs. The perturbation caused by the attracting of the sun, moon, and planets is computed based on the JPL planetary and lunar ephemerides. The tidal perturbations are modeled by following the current IERS conventions. The global ocean tide model FES2004 generated by Lyard et al. (2006) is applied to the processing.

The non-gravitational perturbations require a joint consideration for the characteristics of the forces and the mass, geometry, surface optical properties, and attitude of the

[3]http://icgem.gfz-potsdam.de/tom_longtime

satellites. Therefore, they are more complicated to be modeled than the gravitational ones. In this study, three main non-gravitation perturbations are applied for the POD. The first one is the perturbation due to atmospheric drag. It depends on the atmospheric density along the orbit, the cross-sectional area of the satellite in the relevant direction for the air drag, the mass of the satellite, and the velocity of the satellite. The drag temperature model described by Berger et al. (1998) is used to estimate one drag coefficient parameter per interval. This perturbation is mainly applied to LEOs, especially for the LEOs that fly lower than 1000 km, due to the dense atmosphere at a lower altitude. The second one is the solar radiation pressure (SRP) acting on the satellite area which is illuminated by the sunlight. The SRP is the largest non-gravitational perturbation acting on GNSS satellites. The shape (geometry of different components) and attitude of the satellite decide the size of the illuminated area and the force direction. The reflection characteristics of the satellite surface impact the pressure. The SPR models for GNSS satellites and LEOs are listed in Table 2.3. By introducing the coefficients of the SRP in three directions of a Sun-oriented reference frame as parameters, the empirical CODE (Center for Orbit Determination in Europe) orbit model (ECOM) is developed for GNSS satellites (Beutler et al., 1994). The reduced ECOM (Springer et al., 1999) and the enhanced ECOM (Arnold et al., 2015) are developed to cope with different deficiencies of classical ECOM. Using a similar approach, empirical GPS solar pressure models (GSPM, Bar-Sever and Russ, 1997) were developed at JPL. The ECOM models are popularly used within the IGS. The reduced ECOM with five parameters is used for all GNSS in this study. To model the atmosphere drag and SRP one LEOs, a box-wing macro-model (Marshall et al., 1992) is applied to the LEOs. The macro-models of different LEOs are taken from different sources (Bettadpur, 2012; Cerri and Ferrage, 2015; Montenbruck et al., 2018). Additionally, an enhanced ECOM model (Montenbruck et al., 2015) by introducing a box-wing a priori model is applied to Galileo to improve the solution. The Earth radiation is the third one. It contains the solar radiation reflected by the Earth's surface and clouds and the re-emitted radiation due to the absorbed solar radiation. This perturbation acting on a box-wing satellite is computed by using the functions programmed (Rodriguez-Solano, 2009). It is also used by the IGS third reprocessing campaign [4]. The analytical approach (Rodriguez-Solano, 2009)by using a constant Earth Albedo(0.3) is applied to GNSS satellites in this study. The perturbation caused by the Earth radiation is not implemented to LEOs yet. Although the acceleration of LEOs due to the Earth Albedo is normally smaller than the other perturbations (Bock, 2003; Männel, 2016), it should be considered to determine the orbits more precisely. According to previous studies in literature, the average accelerations of GNSS satellites and LEOs caused by the above-mentioned three perturbations are summarized in Table 2.4. No

[4] http://www.acc.igs.org/repro3/repro3.html

Table 2.4: Average accelerations $[m/s^2]$ caused by non-gravitational perturbations

Sat.	Altitude [km]	Atmosphere	SRP	Earth radiation
GOCE[a]	255	1.6×10^{-6}	2.7×10^{-8}	7.0×10^{-8}
GRACE-A[a]	490	1.5×10^{-8}	5.1×10^{-8}	1.6×10^{-8}
OSTM/Jason-2[a]	1330	2.2×10^{-10}	1.5×10^{-7}	1.8×10^{-8}
GPS[b]	20,200	-	1.0×10^{-7}	9.8×10^{-10}
Galileo[b]	23,200	-	1.0×10^{-7}	1.4×10^{-9}
IGSO[b]	37,000	-	1.0×10^{-7}	7.0×10^{-10}

a. taken from Männel (2016);
b. taken from Teunissen and Montenbruck (2017);

pseudo-Stochastic pulse (Jäggi et al., 2007) is applied in this study.

2.6 Observation equations, processing configuration, and parameters

The observation equations between GNSS satellites s and ground- or space-based receivers r (Teunissen and Montenbruck, 2017) are written as:

$$\begin{aligned} p_r^s &= \rho_r^s(\boldsymbol{r}^s, \boldsymbol{r}_r) + c(dt_r - dt^s) + T_r^s + I_r^s + e_r^s, \\ \varphi_r^s &= \rho_r^s(\boldsymbol{r}^s, \boldsymbol{r}_r) + c(dt_r - dt^s) + T_r^s - I_r^s + \lambda M_r^s + \epsilon_r^s, \end{aligned} \tag{2.6}$$

where p_r^s and φ_r^s are the pseudo-range and carrier-phase observations, ρ_r^s is the geometric range between the transmitter (position $\boldsymbol{r}^s$) and the receiver(position $\boldsymbol{r}_r$), c is the speed of light, dt_r and dt^s are the receiver and satellite clock offsets, T_r^s and I_r^s are the tropospheric and ionospheric propagation delays, e_r^s and ϵ_r^s are the unmodeled errors of the observations. To eliminate the error of the first-order ionospheric delay, the ionosphere-free linear combination $L_3 = \frac{1}{f_1^2 - f_2^2}(f_1^2 L_1 - f_2^2 L_2)$ is performed. Depending the processing purpose, different terms in the equations are treated as estimates or a priori information. The configuration and parameterization for separate and integrated POD of GNSS satellites and LEOs are introduce in Table 2.5. The stochastic model for the ground-based GPS observations is the elevation-dependent weighting model. The space-based observations are equally weighted as the ground-based observations with 90-degree elevation angles. The pseudo-observations defining the constrains are weighted based on the a priori uncertainties. The Position and Navigation Data Analysis (PANDA, Liu and Ge, 2003) software is used for the processing in this study. The PANDA software is a well developed software for orbit determination and positioning in real-time and post-processing. Besides the general information shown in Table 2.5, more details about integer ambiguity fixing strategy and the empirical parameters of LEO POD should be

given. An integer fixing of the ambiguities is performed on the double-difference level and requires data over a longer time interval. Therefore, ambiguity fixing can only be applied for baselines between ground stations or between LEOs in formation flying. As the double-difference ambiguity fixing has very slight impact on the dynamic orbits of LEOs (Guo et al., 2020), it is only applied with the ground stations. The parameters of empirical accelerations are estimated once per revolution in three directions (along-track, cross-track, and radial). In different topics, the parameterization has some difference. In the POD studies, the accelerations in three components are estimated. In the studies about the antenna phase center offsets and the scale, only parameters in along- and cross-track directions are estimated. The LEO orbits are more dynamic than the ones derived by the former configuration. Therefore, the gravitational constraint from the LEOs can be introduced to the studies in Chapter 5 effectively.

The solutions based on the observation equations only can be called kinematic. In the dynamic POD, the observation equations are combined with the motion equations. The initial state of satellite $\boldsymbol{x}_0$, i.e., satellite position $\boldsymbol{r}_0$ and velocity $\dot{\boldsymbol{r}}_0$ at the initial epoch time t_0, and the n force modeling parameters $\boldsymbol{p}_{1,\ldots,n}$ are the unknowns. The satellite state $\boldsymbol{x}_i$ at any time t_i can be derived by the numerical integration from the initial state. The state equation (Montenbruck and Gill, 2000) reads

$$\boldsymbol{x}_i = \boldsymbol{T}(t_i, t_0)\boldsymbol{x}_0 + \boldsymbol{S}(t_i, t_0)\boldsymbol{p}_{1,\ldots,n} \tag{2.7}$$

where $\boldsymbol{T}(t_i, t_0)$ and $\boldsymbol{S}(t_i, t_0)$ are transition matrices and sensitivity matrices formed by truncated Taylor series of Equation 2.5. The estimation is performed by inserting Equation 2.6 to linearized Equation 2.7. The accurate initial epoch states and force modeling parameters are estimated in a least-squares adjustment.

Table 2.5: Configurations and parameterization for different topics in this study

	Common configurations
Software	PANDA software (Liu and Ge, 2003)
Arc length	24 hours (30 hours for overlapping comparison)
Cut-off elevation	7° for ground stations and 3° for LEOs
Observations	zero-difference ionosphere-free phase and code measurements
Weighting	ground-based observations: elevation-dependent weighting model; space-based observations: equally weighted as ground observations with 90° elevation
LEOs attitude	antenna position and star camera based spacecraft attitude (quaternions data provided by operators)
LEOs PVs	not applied
GNSS PV	*IGS.atx* (Schmid et al., 2016)

Station PCOs/PVs	*IGS.atx*
Ambiguity fixing	double-difference; only within ground stations
	GNSS POD
Sampling rate	5 minutes
GPS PCO	known; *igs14_2086.atx*
GNSS orbit	estimated; initial epoch state vector and five solar radiation pressure parameters; initial orbital elements are generated from broadcast ephemeris
Earth Orientation	estimated; IERS EOP as a priori; 24h interval; piece-wise linear modeling
Tropospheric delay	estimated; for each ground station; piece-wise constant zenith delays for 1h intervals; piece-wise constant horizontal gradients for 4h intervals
Station coordinate	estimated; constrained by a priori uncertainties; datum defined by tightly constrained core stations
Clock offset	estimated; satellites and receivers; epoch-wise; pre-eliminated
	LEO POD
Sampling rate	30 seconds
GNSS PCO	known; *igs08_1930.atx* or *igs14_2086.atx* (depending on year)
LEO PCO	fixed to known values
GPS orbits/clocks	known; IGS final products as known information and datum
LEO orbits	estimated; initial epoch state vector; piece-wise empirical accelerations and atmosphere drag parameters; initial orbital elements are generated from official orbit products
Clock offset	estimated; on-board receivers; epoch-wise; pre-eliminated
	Integrated processing
Sampling rate	5 minutes for GPS and LEOs
GNSS PCO	fixed to *igs08_1930.atx* for the study of integrated POD, fixed to *igs08_1930.atx* or *igsR3_2057* or freely estimated for the studies about PCO and scale
LEO PCO	fixed to known values or estimated
GPS orbit	estimated; same as GNSS POD
LEO orbit	estimated; same as LEO POD
Earth Orientation	estimated; same as GNSS POD
Tropospheric delay	estimated; same as GNSS POD
Clock offset	estimated; GNSS, LEOs,and stations; epoch-wise; pre-eliminated
Station coordinate	estimated; same as GNSS POD for integrated POD study; no-net-rotation to a priori for PCO study)

Dynamic POD of GNSS satellites and LEOs

In Chapter 2, some background knowledge and the theory of POD are introduced. The results of dynamic POD for GNSS satellites and LEOs are presented in this Chapter. The processing strategy and some experiment solutions for the dynamic POD of GPS, GLONASS, and Galileo are discussed in Section 3.1. An improved outlier detection method for pseudo-range observations is presented in Section 3.2. By using this method, the initial orbits of LEOs or the SPP solution of a ground-based receiver are improved due to the healthier data used. The POD of seven LEOs are discussed in Section 3.3.

3.1 Precise orbit determination of GNSS satellites

The POD of GNSS satellites is mainly performed with ground-based observations by a dynamic approach (e.g., Montenbruck and Gill, 2000; Hackel et al., 2015; Zhao et al., 2018). The weighted RMS of individual GPS orbit products provided by the IGS ACs with respect to the combined solution is 6.3 mm to 11 mm (Choi, 2014). In this section, the dynamic orbits of GNSS satellites are determined based on the modeling introduced in Section 2.5.2 and the parameterization introduced in Section 2.6. The processing including seven steps:

1. data preparing for broadcast ephemerides, for ground observations, for corrections(e.g., antenna phase center corrections), data related to modeling, etc.;
2. data cleaning for observations based on TurboEdit (Blewitt, 1990);
3. generating the initial orbits by applying orbit integration to the broadcast ephemerides;
4. iterative least-squares (LSQ) estimation;
5. data cleaning based on the residuals of observations and orbit updating based on the estimate after each iteration;

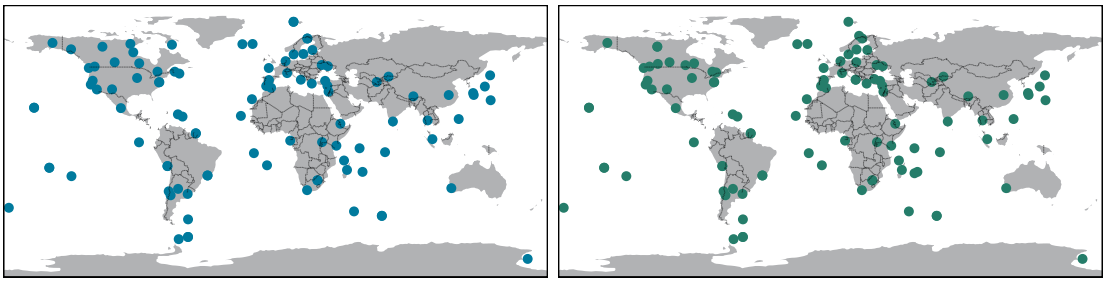

(a) GPS and GLONASS (b) Galileo

Figure 3.1: Selected IGS stations for GNSS POD

Table 3.1: 1D RMS [mm] of GNSS orbits averaged over satellites and 30 days

System	Without Transformation			With Transformation		
	along	cross	radial	along	cross	radial
GPS	41	39	18	20	15	14
Galileo	47	42	22	24	17	19
GLONASS	58	81	35	52	50	19

6. integer ambiguity fixing between ground stations;

7. one more iteration of LSQ estimation and orbit updating.

The processing period is the first 30 days of 2020. BeiDou is excluded due to the ongoing implementation of BeiDou-3 satellites into PANDA software. To compared the orbits between different GNSS, two nearly identical ground station networks are selected. They are presented in Figure 3.1. The left one is used for GPS and GLONASS and includes 100 IGS stations. The right one is used for Galileo and includes 101 IGS stations. The selected stations have precise a priori coordinates provided by the IGS final products in Solution Independent Exchange (SINEX) format, therefore all the stations contribute to the datum due to the strong constraints. The stations of the networks are selected as evenly distributed as possible by using a self-developed script. The script has three steps of selection. First, using the information about observations file offered by Operational Data Centre (ODC) of GFZ AC in JavaScript Object Notation (JASON) format, the multi-GNSS stations obtaining GPS, Galileo, and GLONASS observations are selected for each day. Second, the stations which are always available during the 180 days are selected. At last, based on the coordinates and the selected stations, the stations which are closest to the centers of the geodetic blocks divided by intervals of longitude and latitude are selected. The density of the network can be adjusted by change the intervals of longitude and latitude. Although this is not an optimized algorithm due to the different sizes of the blocks, it is sufficient for the POD according to the experience. The selected two networks have 91 common stations. Therefore, the datum, the number of observations, and the distribution of the two networks are very similar. The determined orbits of the GPS and

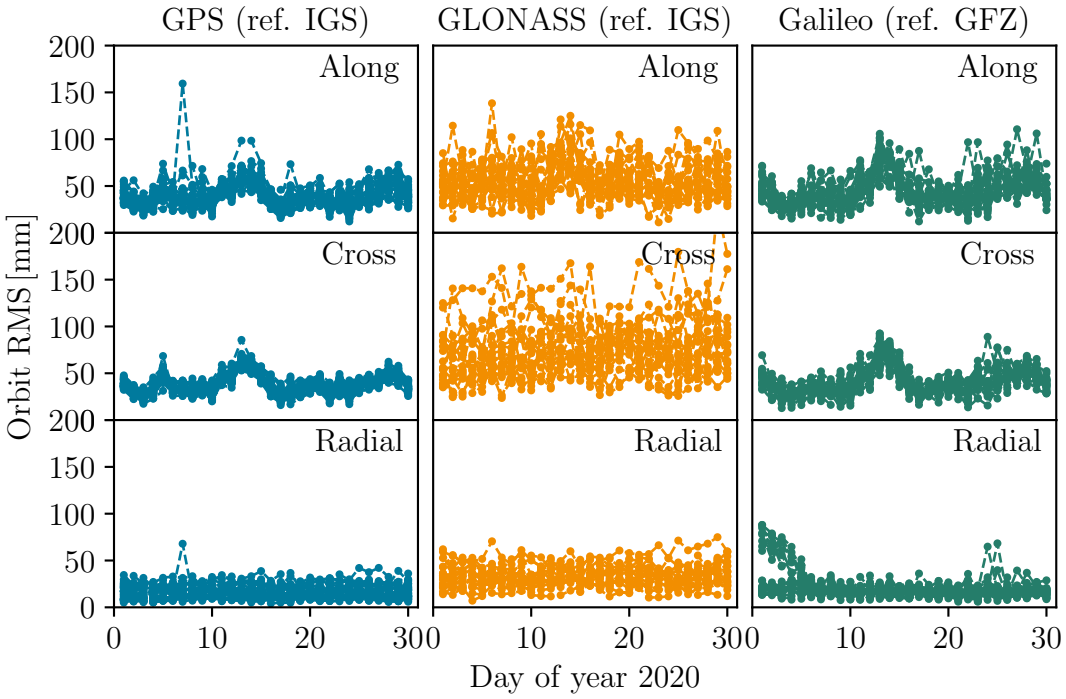

(a) No Helmert transformation

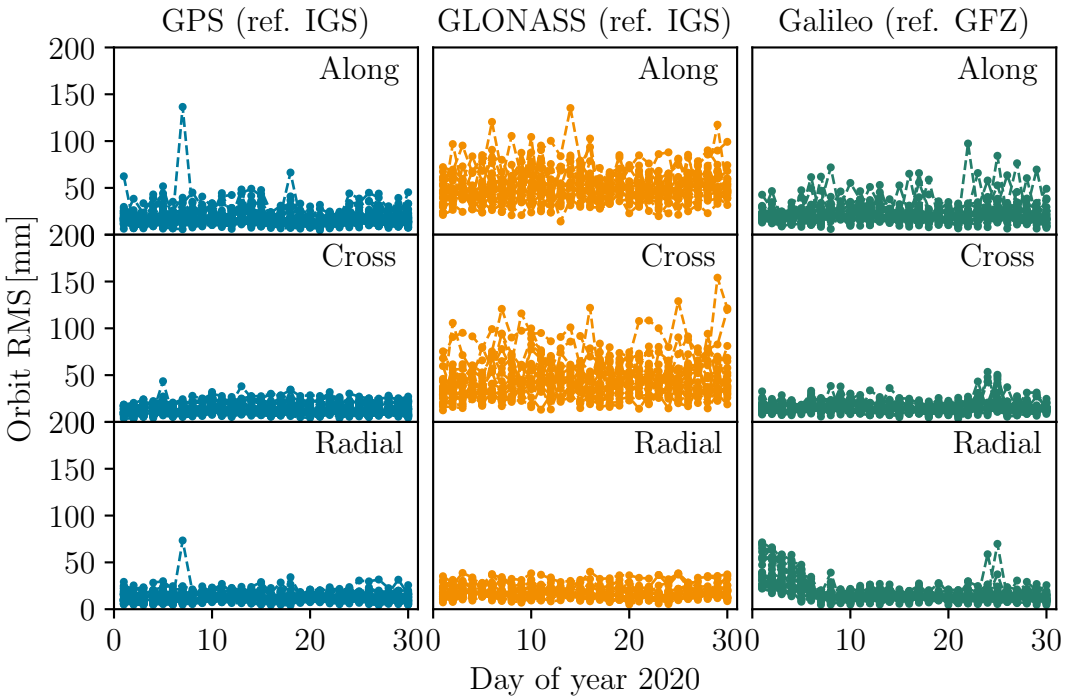

(b) With Helmert transformation

Figure 3.2: Orbit comparison with external products. Helmert transformation is applied in (b). Orbits of GPS and GLONASS are compared with IGS final products. The orbits of Galileo satellites are compared with MGEX products from GFZ

GLONASS satellites are compared with IGS final products (International GNSS Service, 2020). The orbits of Galileo are compared with the MGEX products of the GFZ AC (Deng et al., 2016). The orbit comparison is done in two ways. One is a direct computation of the position differences. In the other one, the seven Helmert transformation parameters are computed simultaneously with the orbit differences in each daily arc. Figure 3.2 presents the root mean square (RMS) of the orbit differences compared to external orbit products in along-track, cross-track, and radial directions. Each curve denotes the time series of one satellite. Table 3.1 shows the 1D RMS averaged over satellites and 30 days.

No matter whether the Helmert transformation is applied, the RMS of GPS and Galileo are smaller than that of GLONASS in three directions. This is mainly caused by the ambiguity fixing issue due to the FDMA signal of GLONASS (see Section 2.1) and by modeling uncertainties of the GLONASS satellites (e.g., PCOs, Dach et al., 2019).

In the comparison without applying Helmert transformation, all satellite orbits have the smallest RMS (two to three centimeters) in the radial direction. Galileo has a slightly larger RMS (three to six millimeters) than GPS in three directions. However, the different sources of the reference orbits have been mentioned above. The GLONASS orbits have 17 mm, 42 mm, and 17 mm larger averaged 1D RMS than the GPS orbits in along-track, cross-track, and radial directions, respectively. Unlike GPS and Galileo having the largest RMS in the along-track direction, GLONASS has the largest RMS in the cross-track direction (81 mm). Moreover, the variation between different satellites of GLONASS is much larger than that of GPS and Galileo. It is also related to the ambiguity fixing issue and modeling uncertainties of GLONASS. Same peaks appear in the time series of RMS in along-track and cross-track directions for GPS and Galileo (also visible in GLONASS). It is caused by the different datum definition between this study and external products.

When the seven Helmert transformation parameters are estimated, the systematic differences caused by the datum definition and the Earth rotation parameters (ERP) are removed. The orbits of all satellites have smaller RMS in three directions than the comparison without applying Helmert transformation. GPS and Galileo have similar reductions with about 20 mm, 25 mm, and 5 mm in the along-track, cross-track, and radial directions, respectively. Consequently, for GPS and Galileo, the orbits of all satellites have similar accuracy in cross-track and radial directions which is higher than the along-direction. It can be explained by the orbit dynamic constraints on the cross-track and radial directions. The reductions of GLONASS orbit RMS are small in along-direction (6 mm in average) but significant in cross-track(31 mm) and radial (26 mm) directions. The variation between different satellites of GLONASS is reduced as well. As a result of removing the impact of datum differences, the peaks in the times series are all gone.

There is an outlier GPS satellite with space vehicle number (SVN) G062 on day seven with obviously larger RMS in along-track and radial-track directions than the other

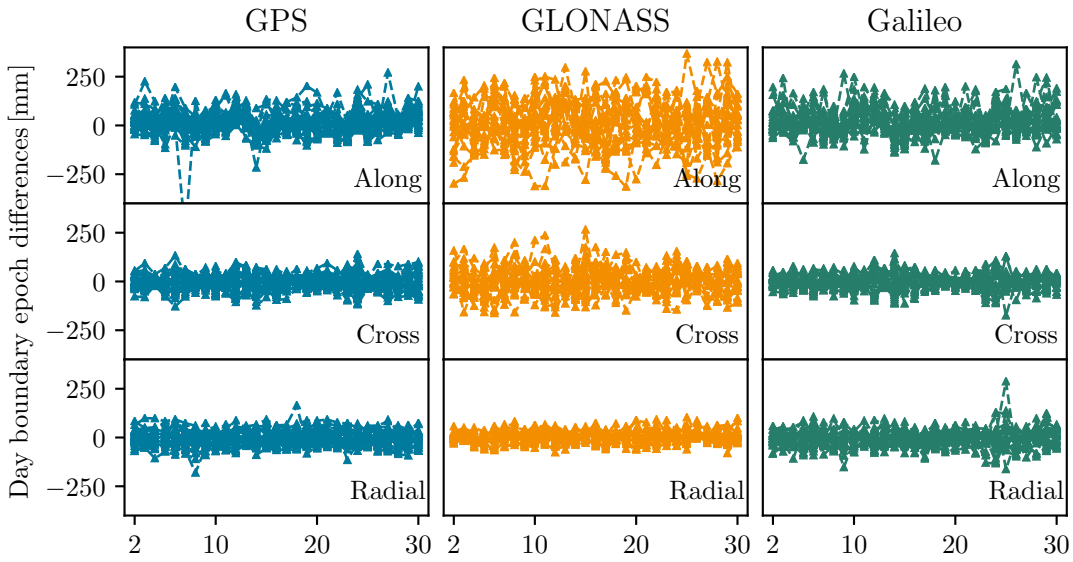

Figure 3.3: Day boundary epoch differences of GNSS orbits

satellites. It is also visible in the day boundary epoch comparison results shown in Figure 3.3. The residuals of its phase observations are three millimeters (average over stations) larger than the other satellites. However, no outlier station is visible. A deeper investigation is needed to find out the reason. Without applying Helmert transformation, eight Galileo satellites have larger RMS in the radial direction than the other satellites in the first six days. Moreover, the RMS in the radial direction of the eight satellites decreased by time and reached the same level as other satellites on the 7th day. Applying Helmert transformation can not remove this issue, therefore it is not a systematic issue. It has been found out that the eight Galileo satellites flew in the same orbital plane (A) with a very small solar elevation angle during the first six days. The orbital solar elevation angle increased from 8° on the first day to 13° on the seventh day. The larger RMS in the radial direction for the eight satellites can be explained by the modeling of the SRP during the eclipse season.

Besides the external comparison, an internal comparison based on the overlapping differences at the day boundary epoch is performed. All the 24-hour orbits are extended by one epoch with orbit integration. The satellite position differences at the overlapping epoch of the two adjacent arcs are computed in three directions. The results are shown in Figure 3.3. Again the position difference RMS of the along-track component is larger than the other components and GLONASS has a large variation between satellites and worse solution than the other system. The external and internal comparisons agree with each other. The POD quality for GNSS satellites in our study is comparable with official products.

3.2 Outlier detection for pseudo-range observations

The GNSS data quality is a very important issue for processing. In the PANDA software and some other GNSS processing software packages, the data quality control is mainly based on TurboEdit in the pre-processing and the iterative data cleaning based on the residuals of carrier phase observations (Blewitt, 1990). However, as any technical issue can hardly be solved perfectly, the outlier may not be detected in special situations. For example, in the integrated orbit determination study discussed in Section 4.3, the outliers in the pseudo-range observations of a ground station are not successfully detected for three days, thus the determined GPS orbits have a much worse accuracy compared with the other days. It may also happen to the data cleaning for the positioning of moving receivers. Therefore, an improved outlier detection method is developed for the pseudo-range observations to make the whole processing more robust. This method can be applied to static and kinematic ground stations and LEOs to improve the accuracy of their positions or initial orbits in the SPP solution. The flowchart of this method is shown in Figure 3.4. In general, it is an algorithm removing only the bad observations based on traversal calculation of epoch-wise position by employing different four-observation subsets and inverse checking of the other observations. The detailed steps are as follows. In the first step, the epoch-wise SPP of a ground station or a LEO is performed by using pseudo-range observations. In the SPP processing, the broadcast ephemerides of GNSS satellites are used as a priori information. The coordinates in three components and the clock correction of the receiver are the four parameters estimated. Meanwhile, the residuals of the pseudo-range observations are computed. This method can be applied when at least five observations are available. To save the computation time, the detection should be applied only to the epochs that potentially have outliers. Whether the maximum residual of all observations is larger than 30 m is the criterion for an epoch with outliers. The next step is to get all four-observation subsets of all the observations (n) in the current epoch. Using the four observations of each subset, SPP is processed again to compute the position and clock correction of the receiver. With a forward step, the distances between all observed GNSS satellites and the derived receiver position are computed. Then the differences in absolute values ($d_{1,\ldots,n}$) between the distances derived in the previous step and the corresponding pseudo-range observations are computed. The mean of $d_{1,\ldots,n}$ ($\overline{d}$) is used to set up the thresholds based on experience. All differences $d_{1,\ldots,n}$ are compared to the empirical thresholds $2\overline{d}$ and $4\overline{d}$. If there is only one d_i larger than $4\overline{d}$ and the remaining $d_{1,\ldots,n-1}$ values are smaller than $2\overline{d}$, the observation with the largest d_i is the outlier. Otherwise, the outlier is not detected in the current subset, then start the processing with the next four-observation subset in the current epoch until the outlier is detected.

This method is on purpose to detect unique but extreme outlier in one epoch. When

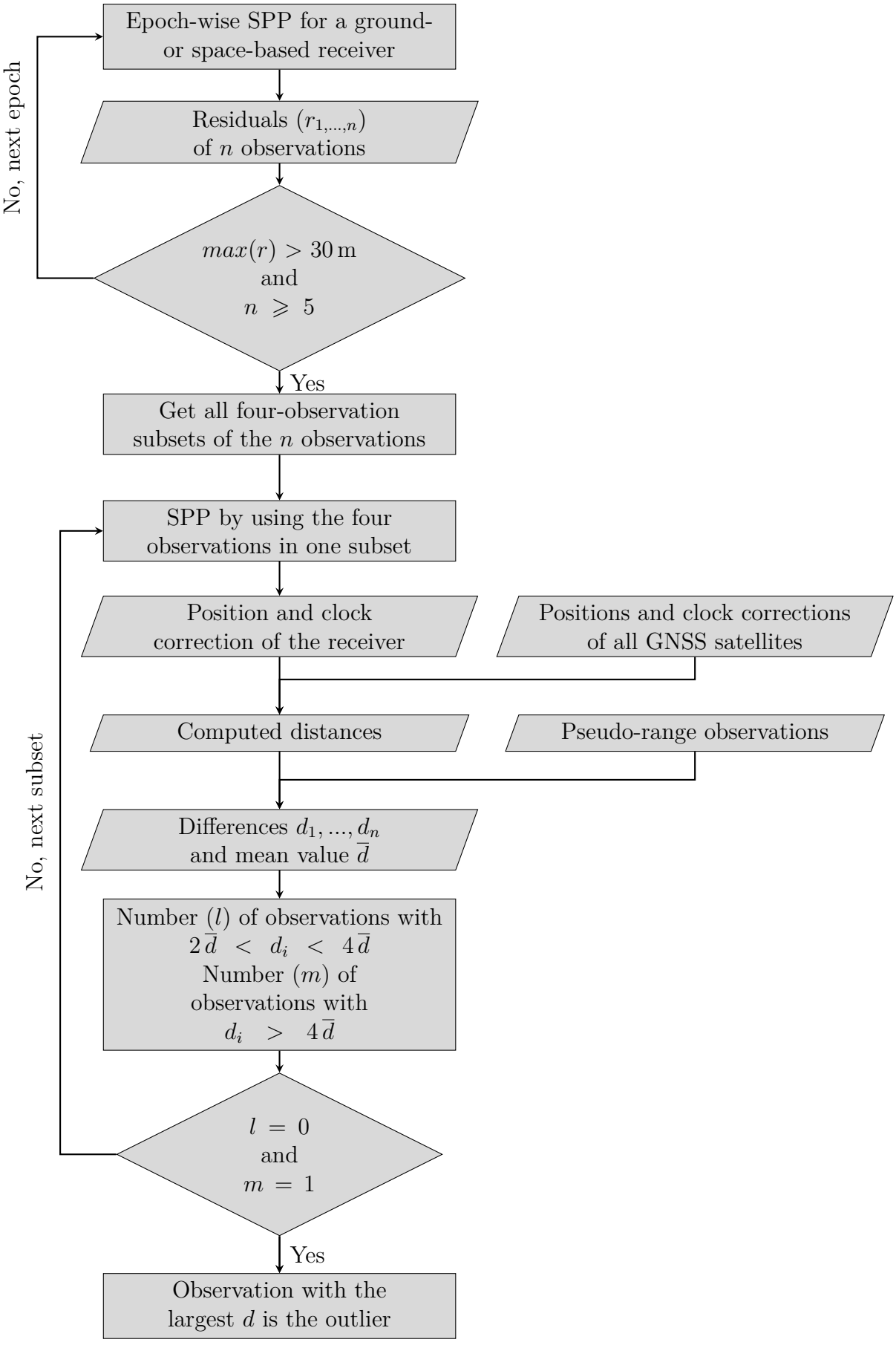

Figure 3.4: Flowchart of improved outlier detection for pseudo-range observations

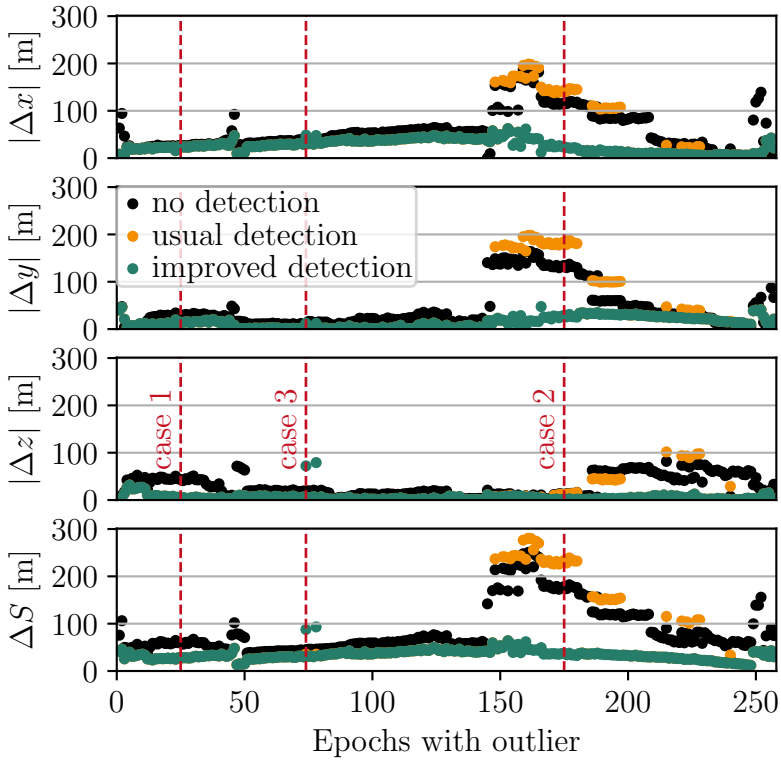

Figure 3.5: Comparison of outlier detection methods based on an one-day SPP solution of GRACE-A satellite, including absolute coordinate differences in three directions (x,y ,and z) and the position differences (ΔS). 257 epochs are detected to have potential outliers. The dashed vertical lines highlight the examples of three cases with different performance of the three methods

the four observations in the processing subset are all healthy and in good geometry, the computed position and clock correction of the receiver is convinced. If there is only one outlier existing, the outlier is reflected in its correction computed by using the solution mentioned above. However, when there are more than one large outliers in the same epoch, this method will probably fail. The thresholds $2\overline{d}$ and $4\overline{d}$ are designed based on practical experience.

By comparing the SPP results of the GRACE-A satellite in three different schemes, the improvement of this outlier detection method is presented below. Based on the 30 m criterion for the maximum residual of pseudo-range observations in one epoch, there are 257 epochs with potential outliers detected on September 16, 2016, for the GRACE-A satellite. In SPP scheme A, no outlier detection procedure is performed. In scheme B, the usually used method (usual detection) by excluding the pseudo-range observation with the largest residual is performed. Scheme C includes the outlier detection method of this study(improved detection). The SPP solutions are compared with the official orbit product of GRACE-A. The position differences and their components in three directions of the Earth-fixed system of the 114 outlier-epochs are shown in Figure 3.5. In general, the improved outlier detection derived the best solution except for a few epochs. Three

Table 3.2: Statistics of the SPP solutions using three outlier detection schemes

	A no detection	B usual detection	C improved detection
$\|\Delta x\|$ mean/STD [m]	76.2/66.2	60.9/76.1	19.0/18.9
$\|\Delta y\|$ mean/STD [m]	69.0/59.0	71.3/72.7	23.3/15.8
$\|\Delta z\|$ mean/STD [m]	37.6/30.9	13.5/23.9	5.4/11.2
ΔS mean/STD [m]	121.4/59.4	99.7/92.7	34.0/12.9
correction rate [%]	-	56.7	97.4
error rate [%]	-	49.3	1.8
failure rate [%]	-	-	0.8

epochs are highlighted as example cases to discuss the three different situations. For epoch 25 (highlighted as case 1), the solutions derived by the usual and improved detection are identical and better than that of no detection applied, because both detection methods exclude the outlier successfully. For epoch 175 which is marked as case 2, the expected solution is presented. By applying the usual detection, instead of the real outlier, another observation with the largest residual is excluded. Since the outlier remains and healthy observations are reduced, the usual detection leads to an even worse solution than that of no detection applied. The improved detection excludes the outlier successfully and improved the solution significantly in case 2. Epoch 74 (marked as case 3) presents the worse result derived by scheme C than by schemes A and B. It is caused by the threshold selection which is difficult to be chosen perfectly. However, there are only two epochs in this case. Additionally, the improved detection method failed for one epoch, thus it is not visible in the plot. The statistic of the three solutions is presented in Table 3.2. Without outlier detection, the solution differs from the precise orbit products significantly (about 120 m in averaged position differences) with a large standard deviation(STD) to the mean (about 60 m). By applying the usual detection implemented in TurboEdit, the solution has smaller averaged position differences (about 100 m), but the absolute differences in the y-direction are (2 m) larger than that of scheme A. Moreover, the STD in x- and y-directions and position differences are 10 m, 13 m, and 33 m larger than those of scheme A. These phenomenons are caused by the above-discussed case 2 which leads to an error rate of 49.3%. The solution derived by the improved detection scheme has significant and overall improvements. It is obviously seen from the mean differences and STD in all components. Consequently, the improved detection scheme has a 97.4% correction rate (37% higher than the usual detection) and merely 1.8% and 0.8% rates for error and failure epochs.

The improved detection is more efficient and reliable than the usual method. Although a larger computation is required by the algorithm, it is not a critical issue for powerful computation processors nowadays. The algorithm improves not only the quality control of

observations but also the initial orbits of LEOs. It is meaningful to the recently launched and future LEOs equipped with multi-GNSS receivers, e.g., FengYun-3C (GPS+BeiDou) and Sentinel-6 (GPS+Galileo). As mentioned before, the selected thresholds impact a lot on the performance of this method. The current thresholds are selected base on the experience from limited experiments. It is an open question about the optimization of the thresholds.

Another outlier detection method based on majority voting is introduced by Bock (2003). By fixing the position of the receiver to the a priori coordinate, only clock corrections are the unknowns in the observation equation. The satellite-specific receiver clock corrections ($cr_{1,\ldots,n}$) are computed. The STD of the difference between two cr parameters is defined by propagation from the STD of the observations. Using three times of the STD as a criterion, all the clock corrections are assigned to different groups via a comparison between each other. The mean value of the group with the most elements is used as a second criterion to re-check all the receiver clock corrections with another manually selected threshold. Comparing with the method in this study, the method from Bock (2003) is more efficient for the epoch with multiple outliers. However, it needs more consideration. Its first criterion related to the STD of the observations depends on the quality of the date. The rejection thresholds should be selected carefully depending on the situation. What is more, the accuracy of the a priori coordinate of the receiver is the key factor limiting the performance, while the method of this study is not affected by this issue. In summary, as solutions to make the processing more robust, both methods have their own advantage, weakness, and specific goals. The combination of both methods to improve the cleaning of data is worth to be studied.

3.3 Precise orbit determination of LEOs

Based on the LEOs on-board observations and a reduced dynamic strategy (Wu et al., 1991), the orbit of the LEO can be determined by precise orbit determination (POD) technique reaching an accuracy level of 1 to 3 cm (e.g., Haines et al., 2004; Jäggi et al., 2007; Montenbruck et al., 2018). The precise determination of the orbits of LEOs guarantees the success of the missions, for instance, Earth gravity field monitoring, sea-level monitoring, geomagnetic field monitoring, etc. The implementation of new LEOs into PANDA software and dynamic POD experiments of different LEOs are introduced in this section.

3.3.1 Implementation of new LEOs in PANDA software

As the purpose of the study is on the enhancement of GNSS orbits and geodetic parameters by integrating LEOs, the implementation of as many as LEOs in our software is a pre-requirement. This is mostly a technical issue that is very important and requires a lot of experience, implementation work, and testing. Until now, besides the already implemented GRACE-A/B and CHAMP satellites, other LEOs, e.g., Jason-1, OSTM/Jason-2, Jason-3, and Swarm-A/B/C satellites, have been added into the PANDA software. More LEOs will be implemented soon in the project entitled 'Integrated GNSS Processing for Earth System Monitoring' (InGE) funded by Deutsche Forschungsgemeinschaft(DFG)[1], and all LEOs with available data will be added in the future. The key points of implementing new LEOs are:

1. data formatting of observations, quaternions data for attitudes, and precise orbit products as the Level-1b data offered by mission operators are normally not in the IGS standard formats, especially for attitude information and precise orbits (to sp3 format);

2. correcting or adding satellite information, e.g., receiver type, satellite name, sp3c code, etc., in the header of the observation files and orbit files; adding the corresponding information to the software;

3. searching and adding available and reliable antenna phase center corrections of the on-board receiver antenna to the software;

4. adding the available macro-model for the LEOs;

5. checking the identification of different LEOs based on satellite names and SP3c codes;

6. testing the performance of the POD with at least one-month data;

7. validating the determined orbits with different methods:

   (a) checking the residuals of observations;

   (b) comparing with external solutions, e.g., the precise products offered by mission operators;

   (c) internal comparison for the overlapping orbits or the day boundary epochs;

   (d) validation based on the residuals of SLR observations.

[1]https://gepris.dfg.de/gepris/projekt/446282290

Besides the common key procedures for all LEOs, the same LEOs might have special issues that should be considered. For example, the quaternion data describing the attitude of Swarm satellites are relative to the TRS while that of other LEOs is relative to the CRS. This is found out in the validation for the first implementing. For the orbit validation, some experiments with real data are discussed in the next section.

3.3.2 Experiments and results

Based on the modeling presented in Table 2.3 and the configurations in Table 2.5, the dynamic POD of the seven LEOs are performed exemplary for one hundred days in 2016 (day 115 to 214). The combined GPS orbit and clock products provided by the IGS are used as a priori. Figure 3.6 presents the RMS of orbit differences compared with official precise orbit products (Case et al., 2002; Dumont et al., 2009, 2016; Olsen, 2019) in along-track, cross-track, and radial directions. Each dot denotes the RMS over all epochs during a whole day. The averaged value over the days and the empirical STD to the mean are also shown in each subplot. For all LEOs, the orbits in cross-track direction have the best accuracy. The satellites of the GRACE and Swarm missions have RMS values of less than 20 mm and STD of less than 10 mm in the cross-direction while OSTM/Jason-2 and Jason-3 are large in this direction with 22±7 mm and 50±13 mm. In the along-track direction, expect the Jason-3 with obviously larger RMS (50 mm), the orbits of the other six satellites have similar RMS (34 to 40 mm). The orbit accuracy in the radial direction is similar for the seven satellites with 30 to 36 mm RMS. The two GRACE satellites have larger STD in along- and cross-track directions than the other satellites and slightly different accuracy between themselves. This is probably caused by the decreased data quality due to the aging of the spacecraft as the processing period is at the end of their service life. Further investigation is needed to find out the real reason. To identify the reason for the less accurate orbits of OSTM/Jason-2 and Jason-3 satellites, the residuals of the observations are checked. The residuals are larger for the two Jason satellites than the other satellites. There might be some modeling issues, e.g., the un-implemented Earth radiation (see Table 2.4) and biased PCOs (different values given by available sources). The epoch-wise orbit differences relative to the precise product for day 141 of 2016 are plotted in Figure 3.7. The larger variation of the epoch-wise orbits of the Jason satellites is also obvious, especially in the cross-track direction. Table 3.3 presents the 3D RMS of LEO orbits in this study and previous studies in the literature. The solutions in this study have slightly lower accuracy than the others. It is mainly caused by the missing modeling for the Earth radiation and stochastic pulses.

Many LEOs are equipped with laser retroreflector arrays, therefore ILRS stations can obtain SLR observations for the LEOs which are independent of GNSS. Moreover, the optical distance measurements of SLR have a mm-to-cm level precision. Therefore, the

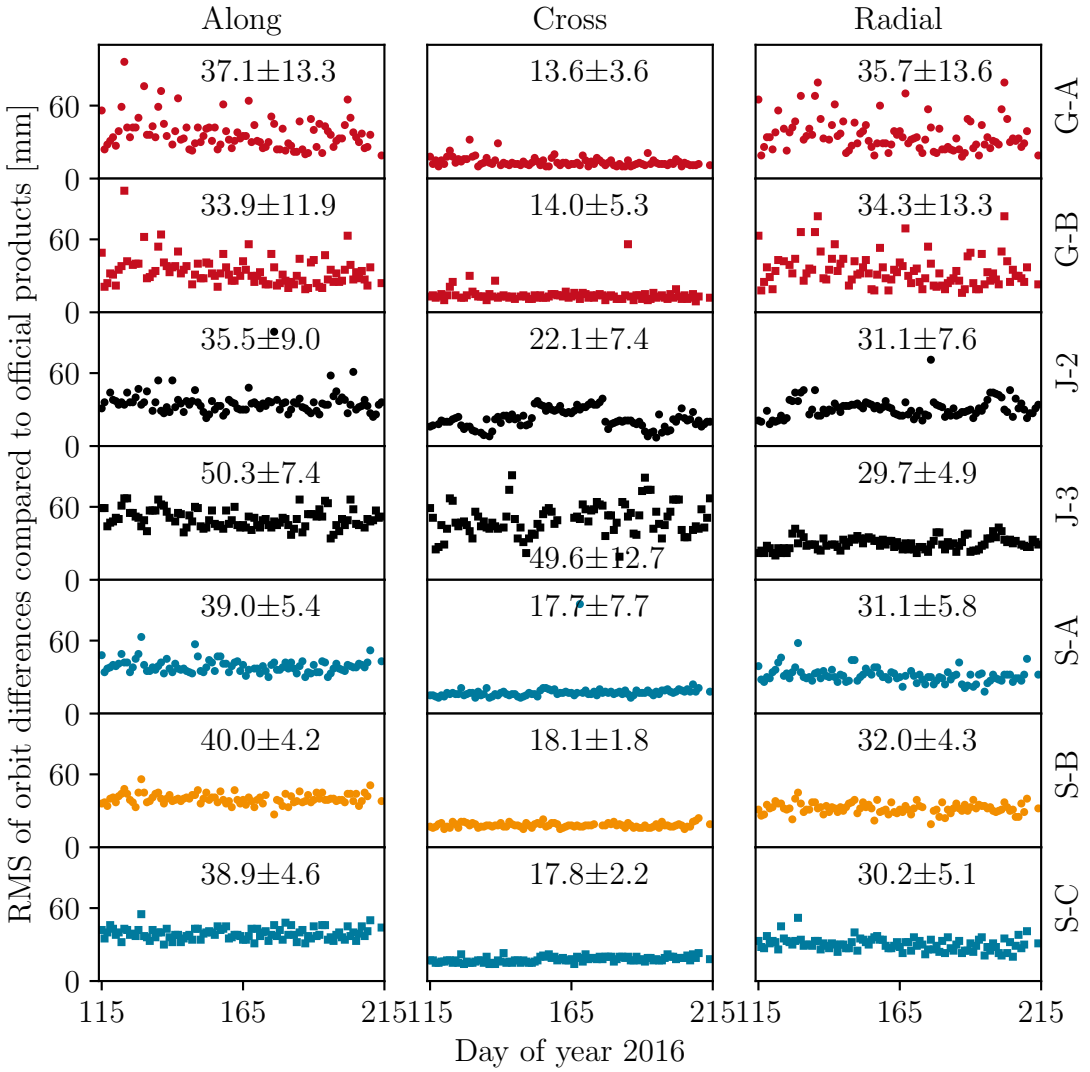

Figure 3.6: RMS of daily orbit differences of LEOs compared to precise orbit products; the satellites fly in the same or similar orbital planes are shown in the same color but different symbols(dots and bins)

Table 3.3: Orbit accuracy of LEOs compared with previous studys. The listed results are 3D RMS [mm] with respect to external orbit products

	GRACE-A/B	OSTM/Jason-2	Jason-3	Swarm-A/B/C
This study	53/50	52	77	53/54/52
Other studies	48[a]	44[b]	33[c]	-[d]

a. Montenbruck et al. (2005) GRACE-B; reduced-dynamic
b. Männel and Rothacher (2017) compared with the products of ESOC.
c. Liu et al. (2019); estimated PCO/PV; ECOM2 for solar radiation pressure model
d. no study founded

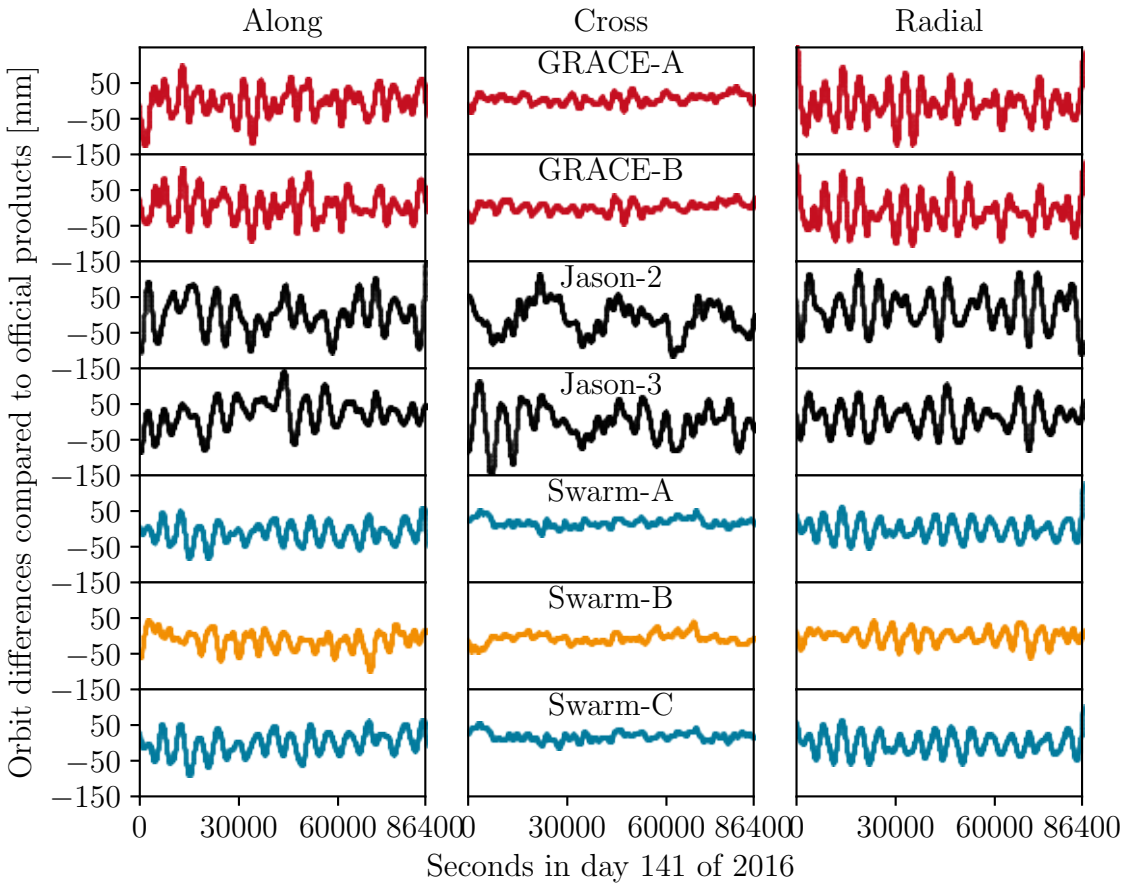

Figure 3.7: Epoch-wise orbit difference compare to precise orbit products in one day

SLR residual, i.e., differences between the range measured by SLR and the range computed from GNSS-based LEO orbits, can be used as an independent and reliable measure for the validation of the determined orbits. The SLR validation for the orbits of the seven LEOs is performed by using all the passes tracked by the Yarragadee station in Australia in the 100 days. Yarragadee is one high-quality SLR station producing usually the highest number of normal points within the ILRS network. The results are presented in Figure 3.8. The number of epochs, the residuals averaged over epochs (mean, i.e., systematic offset), and the STD with respect to the mean are listed in the subplots. Again, Jason-3 satellite has the largest offset (−13.6 mm) and STD (31.3 mm). The three Swarm satellites have the smallest mean value (smaller than 3.5 mm) and most stable residuals (about 20 mm STD). The solutions agree to the external orbit comparison discussed above. The SLR validation for the LEOs in this study is compared with previous studies in Table 3.4. GRACE-A and three Swarm satellites are at a similar level with other studies. GRACE-B has a slightly larger systematic offset (10.0 mm). The OSTM/Jason-2 and Jason-3 satellites have worse solutions compared with the state-of-art. Although the orbits of Jason satellites could be improved, the current orbit accuracy of the seven LEOs is sufficient for the quantitative studies in Chapters 4 and 5.

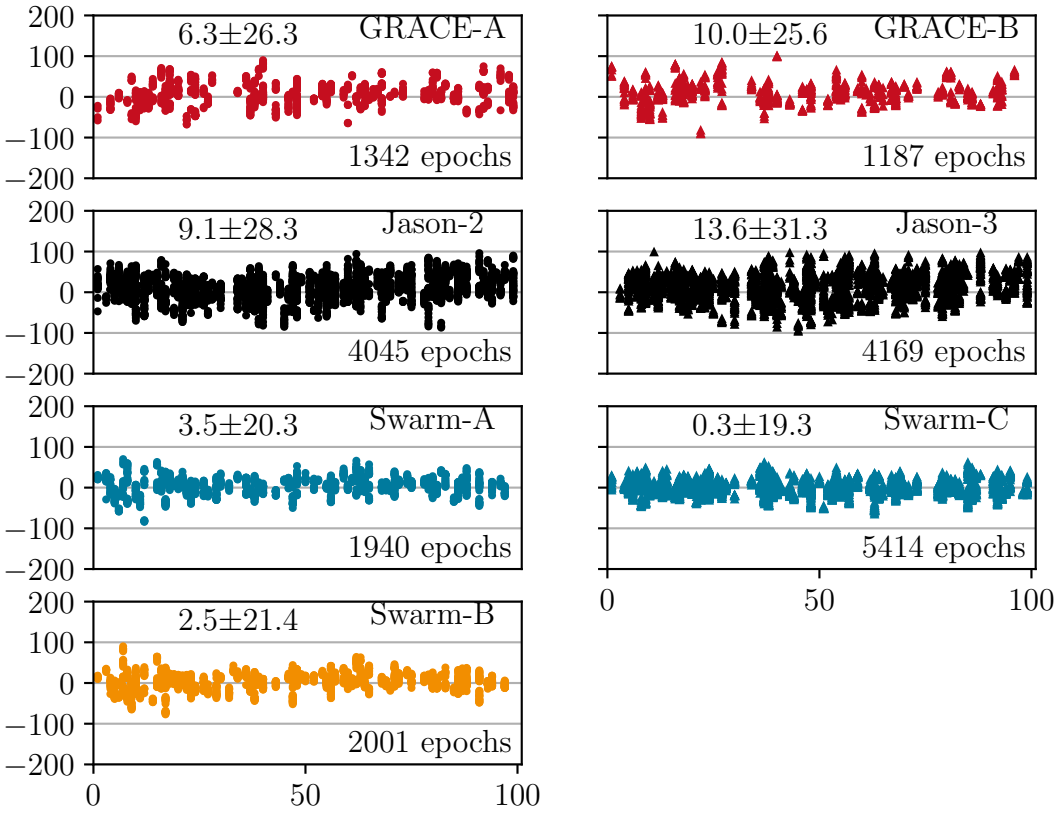

Figure 3.8: SLR observation residuals [mm] for the seven LEOs for all passes tracked by the Yarragadee station in Australia. The gaps are caused by missing SLR observations

Table 3.4: SLR residuals(mean and STD [mm]) of LEO orbits compared with other studies

LEOs	this study	other studies	
GRACE-A	6.3±26.3	-5.1 ± 15.2^{a}	0 ± 24.4^{e}
GRACE-B	10.0±25.6	-3.3 ± 18.8^{a}	3.8 ± 24.7^{e}
OSTM/Jason-2	9.1±28.3	4.8 ± 6.8^{b}	—
Jason-3	13.6±31.3	3.3 ± 20.1^{c}	—
Swarm-A	3.5±20.3	1.2 ± 7.9^{d}	-0.6 ± 24.3^{f}
Swarm-B	2.5±21.4	-0.6 ± 7.4^{d}	-0.6 ± 21.1^{f}
Swarm-C	0.3±19.3	0.5 ± 8.1^{d}	1.2 ± 23.8^{f}

a. Mao et al. (2019); 30 days in 2015; Yarragadee station only.
b. Bertiger et al. (2010); JPL GPS only solution; July 2008 to May 2009; 4 ILRS stations.
c. Liu et al. (2019); 270 days in 2016.
d. Montenbruck et al. (2018); November 2013 to the end of 2017; 14 ILRS stations.
e. Jäggi et al. (2007); 335 days in 2003; 19 ILRS stations.
f. van den IJssel et al. (2015); November 2013 to the end of 2014; 18 ILRS stations.

GPS orbit improvement by integrating LEOs

In chapter 3, the POD of GNSS satellites and LEOs were introduced and discussed separately. The integrated processing of ground and space-based GNSS observations for the jointly POD of GNSS satellites and LEOs is presented in this Chapter. Due to the limitation in space-based observations of other GNSS, only GPS is currently suitable for this study. The main goal of this chapter is to present the improvement of GPS orbits by integrating LEOs, especially for the solutions with sparse and small ground networks. In section 4.1, the concept and method of the integrated POD are introduced. Some theoretical analysis regarding additional observations and geometry from LEOs is given in section 4.2. A study based on real observations is presented in section 4.3 to show the GPS orbit improvement by including LEOs in practice. This study has been published in the Journal of Geodesy (Huang et al., 2020). Section 4.4 gives a summary of the study and some discussion about the technical feasibility of some trending topics, for example, the GNSS augmented by large LEO constellations and the LEO enhanced GNSS-based positioning.

4.1 Introduction of integrated POD

Several studies integrated the LEOs with GNSS in a joint POD processing. Zhu et al. (2004) and König et al. (2005) compared two POD approaches for GPS, the GRACE and the CHAMP satellites. In the first approach named 'one-step', the orbits of the above-mentioned satellites are estimated simultaneously. In the other approach with two steps, the orbits of the GPS satellites and the LEOs are determined sequentially. The authors concluded that the orbits of GPS satellites and LEOs, the geocenter, and the gravity field have a better solution in the 'one-step' approach. Especially, the GPS orbits derived by the 'one-step' approach 27 mm smaller RMS than that of the 'two-step' approach. Geng et al. (2008) shown that the GPS satellite orbits derived by supplementing a 21-station network with GRACE and CHAMP satellites are more accurate than the solution based on a 43-station network (53 mm versus 80 mm in 3D RMS). Otten et al. (2012) combined

various GNSS satellites and LEOs at the observation level including GNSS, DORIS, and SLR. Zoulida et al. (2016) and Zhao et al. (2017) performed an integrated POD for OSTM/Jason-2 and FengYun-3C with GPS and BeiDou, respectively. Since Zoulida et al. (2016) used 121 IGS stations, the improvement of GPS orbits by including only OSTM/Jason-2 satellites is not significant (0.2 mm on average). These studies reported the benefits of integrating LEOs into the POD in different aspects. However, only one or two LEO missions that have GNSS data were considered in the above-mentioned studies. As introduced in Section 2.3, this study integrates seven LEOs to the joint POD with GPS satellites, including GRACE-A/B, Jason-2/3, and Swarm-A/B/C. Based on the integrated processing of different subsets of the ground stations and the LEOs, the impact of integrating LEOs on the GPS orbit improvement is discussed.

The method of the integrated POD applied in this study is known as the one-step method (Montenbruck and Gill, 2000). Figure 4.1 presents the flowchart of the whole processing. The approximate initial epoch status of GPS satellites and LEOs are computed from broadcast ephemerides and by SPP, respectively. Before the one-step estimation, all the observations are cleaned based on the TurboEdit. Several iterations of estimation are performed to improve the solution. After each estimation, the orbits of GPS satellites and LEOs are updated by orbit integration based on the new solution of initial epoch states and force model parameters. Meanwhile, the data are cleaned based on the residuals of observations. After completing the data cleaning, the ambiguities of the ground station observations are fixed to improve the solution. After one more iteration of estimation and orbit updating, the final orbits of GPS satellites and LEOs are determined.

Most of the above-mentioned studies and this study use the approach of processing zero-differenced GNSS observations in one least-squares adjustment to combine the LEOs and ground network. Some other approaches are necessary to be mentioned. Kang et al. (2006) and Jäggi et al. (2007) formed double-differenced observations between LEOs and ground stations. Jäggi et al. (2009) added zero-differenced LEO normal equations to zero- or double-difference ground network normal equations. This is an alternative way for the one-step approach.

4.2 Theoretical analysis based on observations status

Before the studies based on real data, some theoretical analysis based on the number and the geometry of the observations can be done. Some statistics about the visible LEOs for GPS satellites are performed on DOY 115 of 2016. According to orbital characteristics

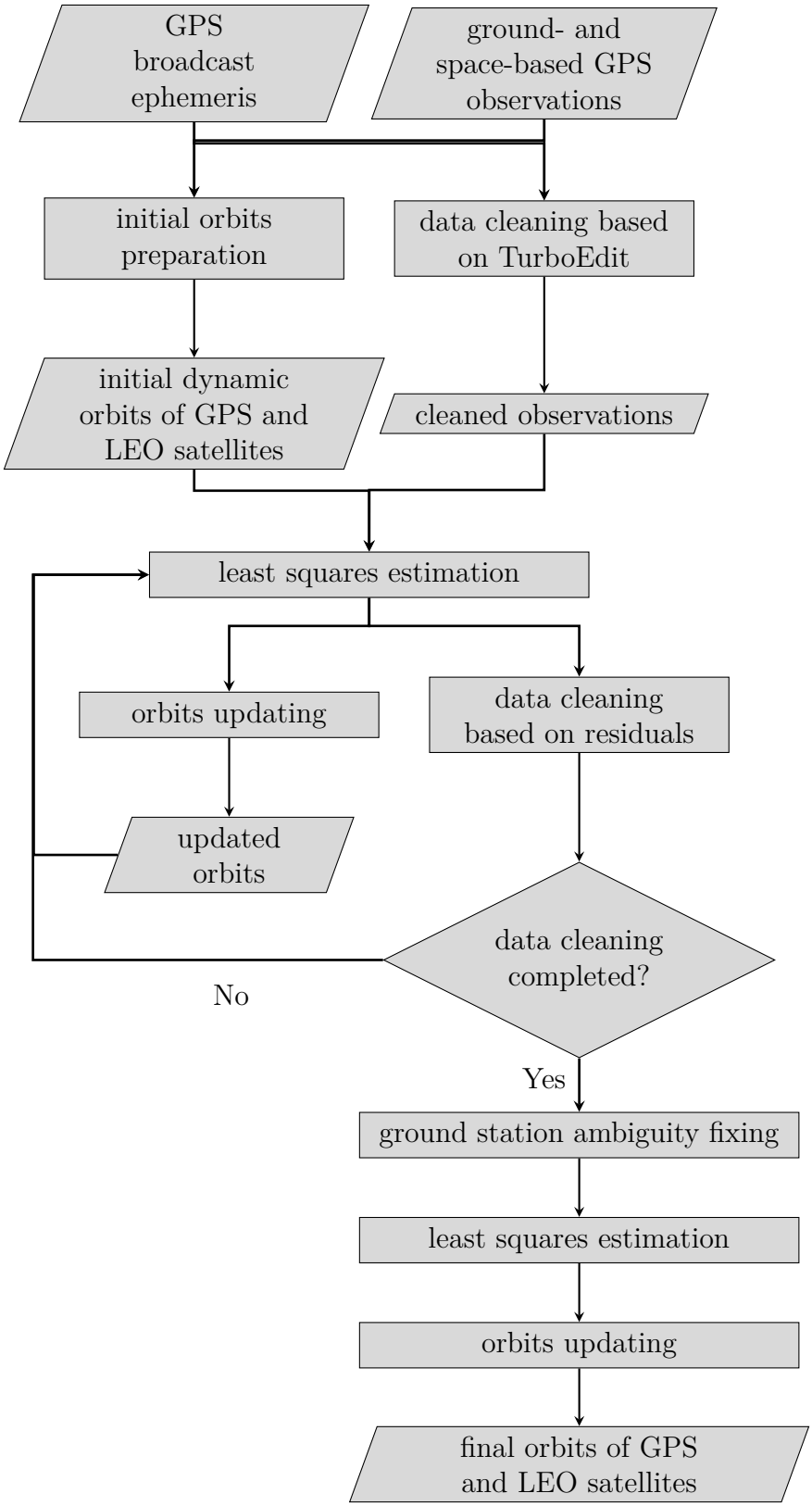

Figure 4.1: Flowchart of the integrated POD

of the seven LEOs introduced in Section 2.3, GRACE-A and GRACE-B flew in the same orbital plane, OSTM/Jason-2 and Jason-3 were sharing the same orbit, and Swarm-A and Swarm-C are twin satellites flying close to each other. Therefore, considering the observation geometry with respect to GPS satellites, the seven LEOs were flying in four orbital planes. The study in the next section takes the same consideration for the analysis.

A 30-second sample rate (2880 epochs per day) is used for the space-based observations of the seven LEOs. Taking one GPS satellite as an example (G12 here), the number of visible LEOs, LEO-visible epochs, and ionosphere-free combined observations (one per measurement) in one day are presented in Figure 4.2. The subplots show the results of cases including different subsets (on the top of each plot) of the seven LEOs. The different colors denote the number of orbital planes occupied by the current LEO subsets. For example, the subplots in black include one LEO or two LEOs in the same orbital plane. The total visible epochs and observations are also listed in each subplot. In subsets 1 to 4, due to the different trajectories of the four LEOs in different orbital planes with respect to that of G12, the visible observations (equal to epochs) vary from 595 of OSTM/Jason-2 to 1098 of GRACE-A. After adding one LEO in the same orbital plane, i.e., comparing subsets 5 to 1 (GRACE-A/B versus GRACE-A), 6 to 2 (Jason-2/3 versus Jason-2), and 7 to 3 (Swarm-A/C versus Swarm-A), the number of observations increase to double or even more while the visible epochs increase only slightly. However, if the added LEO flies in another orbital plan, for example, comparing subsets 2 and 8 (Jason-2 versus Jason-2+Swarm-A), the increase of the visible epochs are more significant (708 when 889 observations are added). It means that if the additional LEO flies in another orbital plan, the majority of the additional observations contribute to the additional visible epochs. Comparing between subsets 12 (three LEOs in three orbital planes) and 13 (four LEOs in two orbital planes) or between subsets 15 (four LEOs in three orbital planes) and 16 (five LEOs in three orbital planes), the subsets with more observations of one more LEO have even fewer visible epochs. It is also caused by the different orbital planes. For subsets 15, 17, 18, and 19, with significantly increasing observations (3613 to 6280), the visible epochs increase very slightly (2338 to 2410). The reason is that the four subsets all include satellites in four different orbital plans, thus the enhancement to the visible epochs is close to saturated (2880 epochs maximum). A further enhancement should be considered as adding more LEOs in different orbital planes.

Figure 4.3 is the histogram of visible LEOs from all GPS satellites during the same day. Seven LEOs are all included. GPS satellite with PRN G04 is not included in any observation files offered by the mission operators. This is probably related to the unstable data quality of G04 in 2016 that will be discussed in Section 4.3.1. Although there are some differences between the GPS satellites, the number of visible epochs and observations are proportional. Thanks to the rapid movement of LEOs, the seven LEOs are offering a

stable enhancement to the GPS constellation. With more LEOs included, the differences between different GPS satellites can be removed.

4.3 Integrated POD based on real data

A study based on real data is presented in this section. The orbit modeling for LEOs and GNSS satellites is given in Table 2.3. The configuration for the processing and the estimated parameters has been introduced in Table 2.5. As a pre-processing, the selection of ground stations and the data status of ground- and space-based data are introduced in the first part. Then the results of 26 different scenarios integrating different subsets of LEOs are discussed via external and internal comparison and geolocated visualization. Additionally, the improvement by supplementing a regional distributed ground network by LEOs is presented. At last, to give a reference, the sparse network+LEOs solution is compared with a solution derived by a 62-station ground network.

4.3.1 Data status and ground station selection

Since the processing includes seven LEOs of four missions, the availability of the LEOs' data is a major limitation when defining the processing period. After checking the data availability of the seven LEOs, I choose the day of the year (DOY) 115 to 260 in 2016 as our processing period. In this period, all seven LEOs were in operation. GRACE satellites were at the end of their operating life, while Jason-3 was launched on 17 January 2016 and its quaternion data started to be available from DOY 115 in 2016. To check the LEOs' data quality, a daily POD of each LEO is processed with a 300-second data sampling rate. The IGS final orbit and clock products are introduced as a priori information. Missing data (onboard GPS observation or attitude) for some days is noticed. Some additional days were excluded for maneuvering or low data quality caused by spacecraft problems. Please note that I excluded these days completely also in the following integrated processing. In the integrated processing, I also excluded maneuvering GPS satellites based on the information provided in the GPS NANU Messages. Based on the information offered by the sensor meta information system (semisys[1]) of GFZ, the G04 signals were not available in the first two months of 2016 and changed three times among reserve satellites with SVN G036 (Block IIA), G038 (Block IIA), and G049 (Block IIRM). Therefore, G04 was excluded completely due to the unstable data quality. Finally, 112 days are selected for the integrated processing and are indicated by green dots in Figure 4.4.

There are 319 IGS stations available during the selected 112 processing days. I selected a sparse and homogeneously distributed subset from the 319 available IGS stations to

[1]https://semisys.gfz-potsdam.de/semisys/

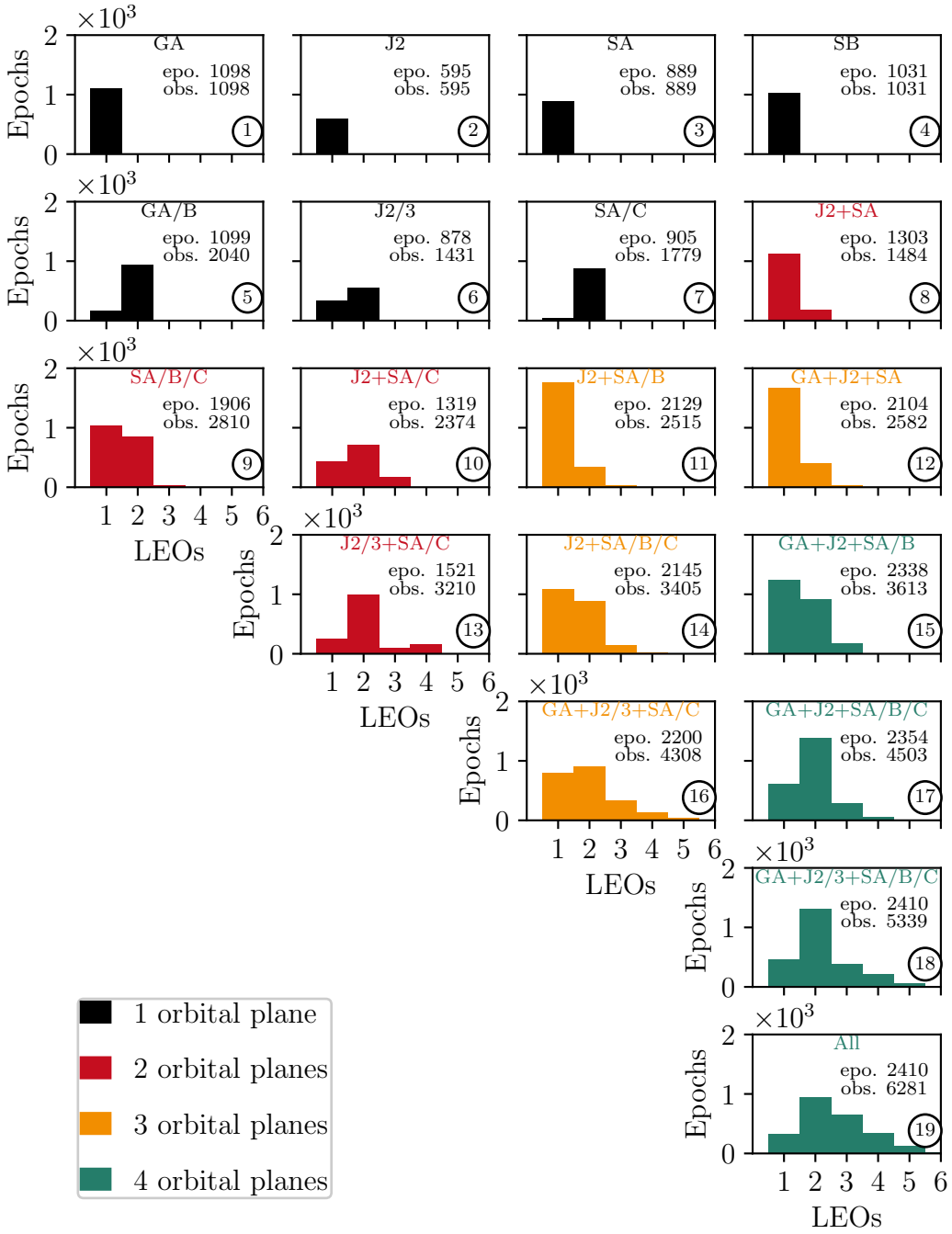

Figure 4.2: Histogram of visible LEOs from one GPS satellite during a day when different subsets of LEOs are included. The included LEOs are shown on the top of each subplot. The numbers of LEO-visible epochs and ionosphere-free combined observations, i.e. one observation per measurement, are listed in each subplot

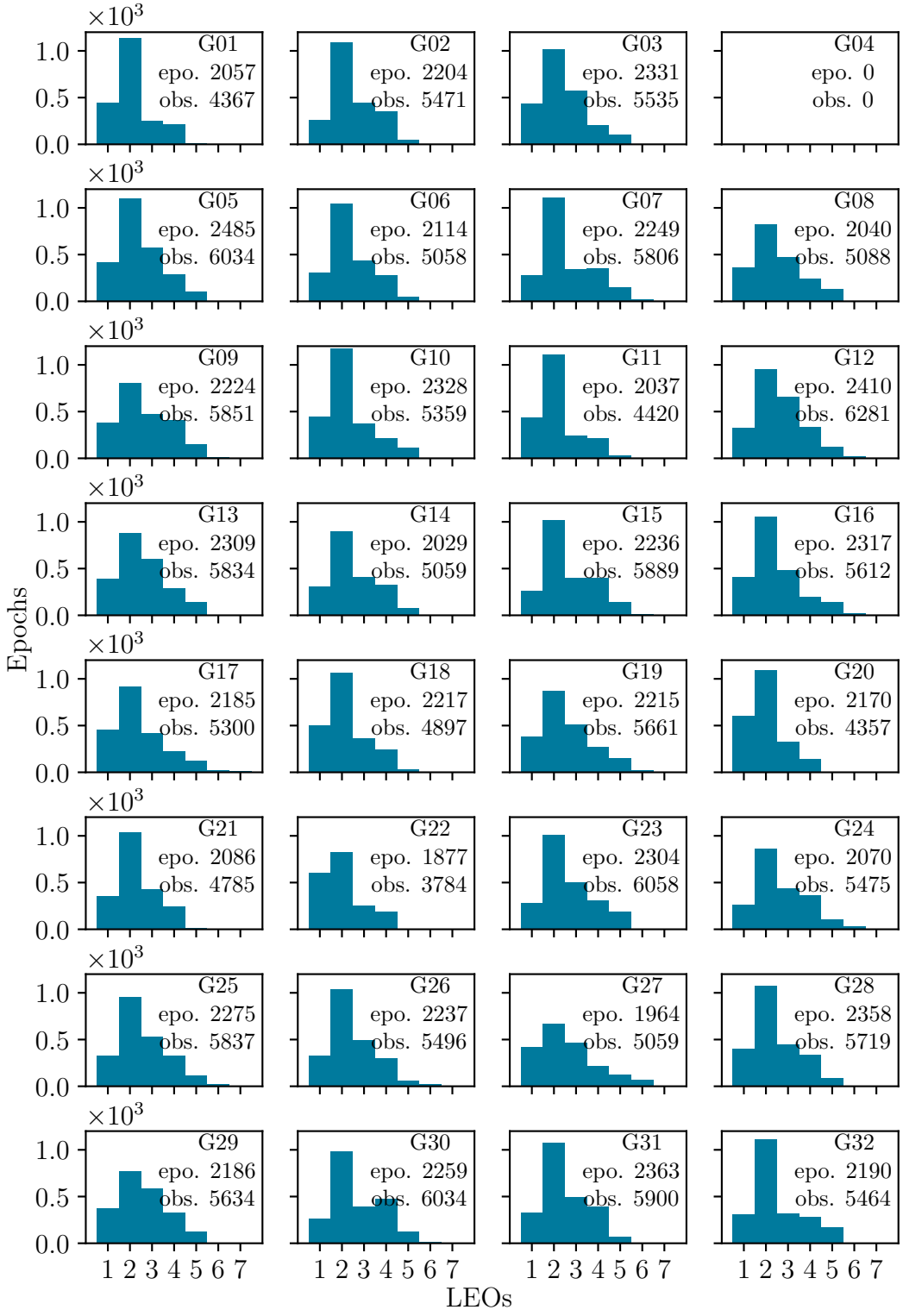

Figure 4.3: Histogram of visible LEOs from all GPS satellites during a day. Seven LEOs are included. The numbers of LEO-visible epochs and the ionosphere-free combined observations, i.e. one observation per measurement, are listed in each subplot

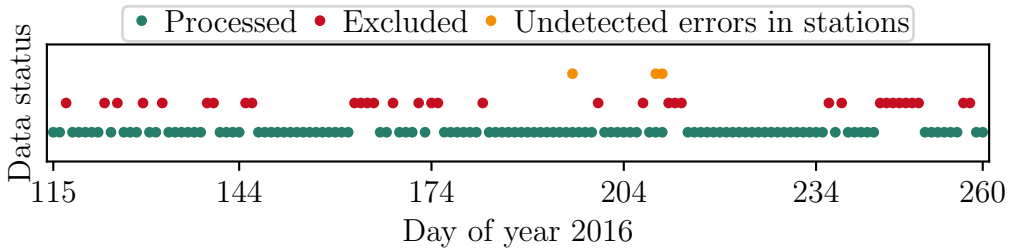

Figure 4.4: Data status for the study of integrated POD

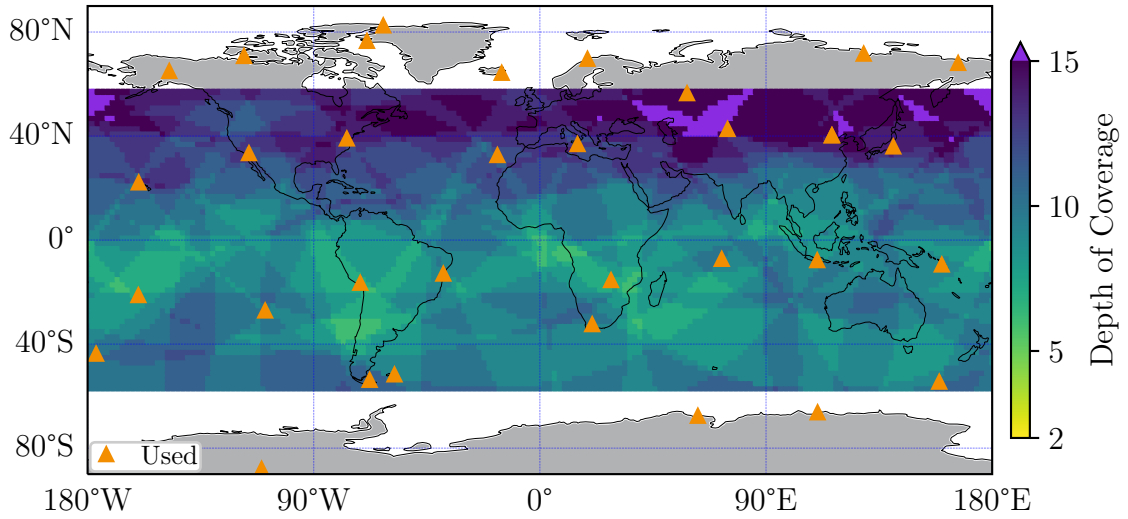

Figure 4.5: A subset of the available IGS stations including 33 homogeneously and sparsely distributed stations (orange triangles). The number of stations in sight of a potential GPS satellite position (Depth of Coverage) is presented as a colored bin (2° × 2° resolution, 20,200 km altitude)

study the sparse-network-based POD. This network contains 33 stations which are plotted as orange triangles in Figure 4.5. The color of the bins in Figures 4.5 and 4.6 presents the number of stations in sight of a potential GPS satellite position with an altitude of 20,200 km and an inclination of 57° (i.e., depth of coverage, DoC). In general, more than five stations are visible, and this is also what I expected based on the selection criteria.

Despite the large and dense IGS tracking network in certain circumstances, depending on constellations and frequencies, one might be confronted with large regions without tracking stations, especially over the oceans and Africa. Although IGS stations are globally available, there are regions with only a few tracking stations. Moreover, IGS stations could be unavailable for various reasons, and it might happen to the ground segment of GNSS as well, for instance, caused by the withdrawal of the United Kingdom from the European Union (Gutierrez, 2018). To investigate how the LEOs could contribute to the GPS POD, I selected a sparser station network (see Figure 4.6) by excluding seven (red triangles) of the 33 stations mentioned above. Consequently, gaps

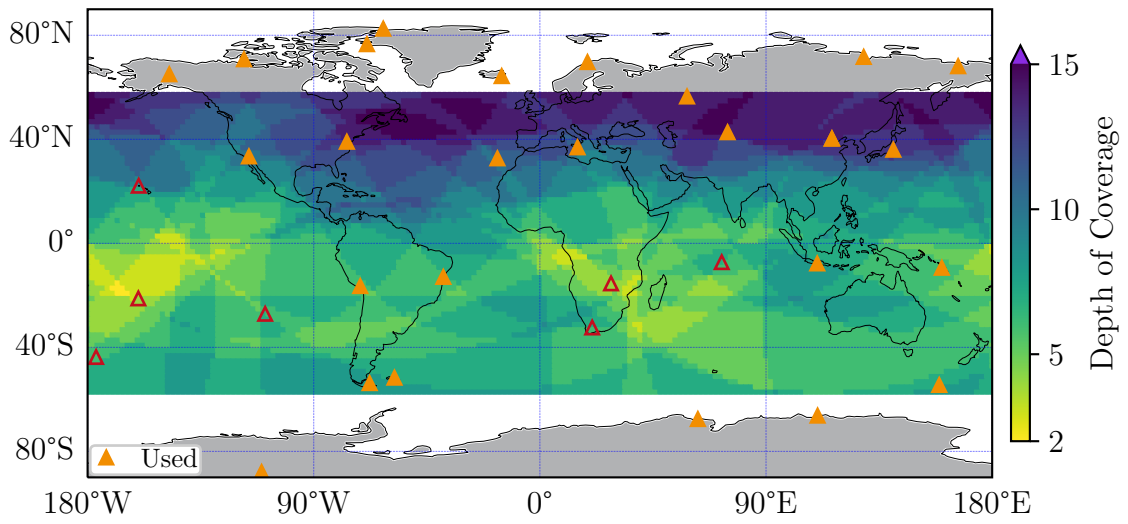

Figure 4.6: A subset of the available IGS stations including 26 non-homogeneously and sparsely distributed stations (orange triangles). The red hollow triangles are the seven excluded stations. The number of stations in sight of a potential GPS satellite position (Depth of Coverage) is presented as a colored bin ($2° \times 2°$ resolution, 20,200 km altitude)

in some regions of the Pacific Ocean, the Indian Ocean, and Africa are visible. There are large areas where a fictitious GPS satellite could be tracked by only two to four (yellow bins) stations. Although two simultaneous observations can support the estimation of satellite clock corrections and orbit parameters in a dynamic solution, fewer observations still lead to a reduced contribution.

4.3.2 Results and analysis of 26 scenarios

To investigate the impact of the number of integrated LEOs and their orbital planes on the determined GPS satellite orbits, a total of 26 different scenarios are applied for the POD processing. All the scenarios are summarized in Table 4.1. The first two are the GPS-only POD (i.e., without LEOs) by applying the two sparse station networks which are described above. The other 24 scenarios are the integrated POD of GPS satellites and LEOs, and all of them supplement the sparser network with 26 stations by including different subsets of the seven LEOs. The estimated GPS satellite orbits of all scenarios are compared to the IGS final products to show the orbit quality and the differences between the scenarios. Due to a large number of satellites and scenarios, statistical measures of the orbit comparisons are computed to quantify the result of each scenario. The statistical computation is shown in Figure **??**. For each daily orbit comparison, the RMS of orbit differences in three orbital directions (along-track, cross-track, and radial) and the 1D-mean RMS are computed. The RMS in three orbital directions is computed over epochs and satellites. The 1D-mean RMS is computed over epochs, satellites, and the three

Table 4.1: Statistical results of the GPS satellite orbit differences w.r.t. the IGS final products from 26 scenarios. The first two scenarios are ground-based only solutions. In the other 24 scenarios, the 26-station network is supplemented by different subsets of LEOs. The colored symbols present the different orbital planes. The mean and STD (relative to the mean) of the orbit RMS (direction-specific and 1D-mean) time series are listed in four columns. The last column is the 1D-mean improvement w.r.t. scenario 1

Sce.	Sites	G-A	G-B	J-2	J-3	S-A	S-C	S-B	orbital planes	Mean/STD of orbit RMS [mm] Along	Cross	Radial	1D-mean	Impro. [%]
1	26								0	50.9/22	31.6/5	22.0/3	37.5/13	-
2	33								0	34.5/6	24.2/3	16.5/2	26.7/4	27
3	26	■							1	41.3/14	27.0/3	19.4/3	31.2/8	16
4	26		■						1	42.7/15	27.7/4	19.7/3	31.7/9	15
5	26			●					1	41.9/13	27.9/3	19.9/2	31.7/8	14
6	26				●				1	39.7/14	27.4/3	19.5/2	30.6/8	17
7	26					▲			1	41.0/10	27.8/4	19.6/2	31.3/6	14
8	26						▲		1	40.9/8	27.7/3	19.6/2	31.4/4	14
9	26							▲	1	40.8/8	28.4/3	19.5/2	31.2/5	14
10	26	■	■						1	39.1/11	26.3/3	18.9/3	29.9/6	19
11	26			●	●				1	39.2/12	27.2/3	19.6/2	30.4/7	17
12	26					▲	▲		1	39.8/7	27.7/3	19.5/2	30.7/4	16
13	26					▲		▲	2	36.2/4	26.8/3	18.3/2	28.6/3	21
14	26				●	▲			2	34.9/6	25.3/3	18.1/2	27.5/4	24
15	26		■			▲			2	36.0/5	25.5/3	18.2/2	28.1/3	23
16	26					▲	▲	▲	2	35.6/4	26.9/3	18.2/2	28.3/3	22
17	26				●	▲	▲		2	34.3/5	25.2/2	17.9/2	27.2/3	25
18	26				●	▲		▲	3	32.1/3	24.9/3	17.2/2	26.0/2	28
19	26	■			●	▲			3	31.1/4	23.6/2	17.0/2	25.1/2	31
20	26			●	●	▲	▲		2	34.0/4	25.1/2	18.0/2	27.0/3	25
21	26				●	▲	▲	▲	3	31.7/3	24.9/2	17.1/2	25.8/2	29
22	26	■			●	▲		▲	4	29.8/3	23.7/3	16.5/2	24.4/2	32
23	26	■		●	●	▲	▲		3	30.6/3	23.5/2	17.0/2	24.9/2	31
24	26	■		●		▲	▲	▲	4	29.6/3	23.7/2	16.5/2	24.4/2	32
25	26	■		●	●	▲	▲	▲	4	29.5/3	23.6/3	16.5/2	24.3/2	33
26	26	■	■	●	●	▲	▲	▲	4	28.9/3	23.2/3	16.4/2	23.9/2	34

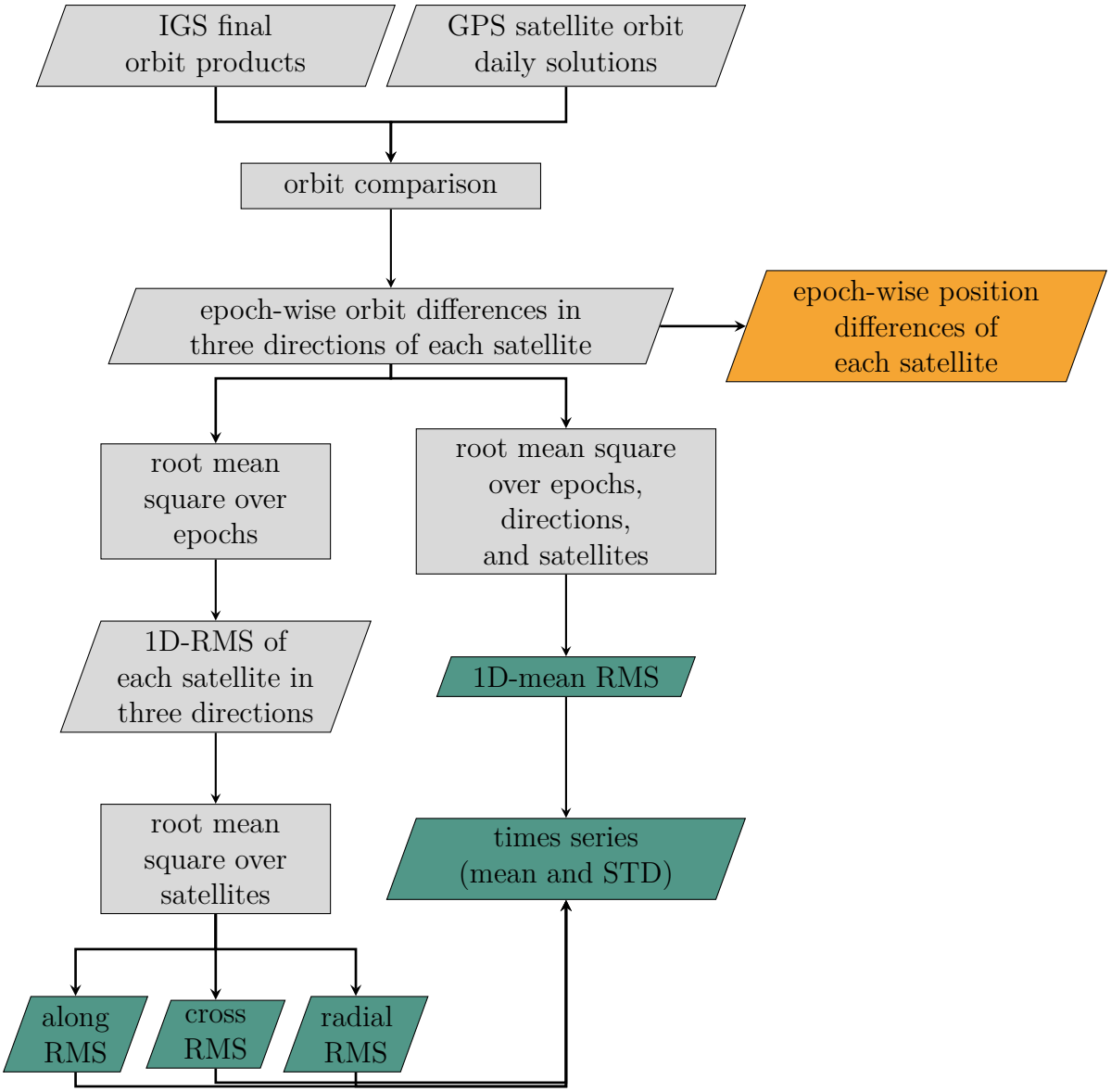

Figure 4.7: Flowchart of the statistical computation. The green and orange outputs are the values used in the analysis of this study.

orbital directions. Based on the 112-day solutions, the mean and STD (relative to the mean) of the time series of the above-mentioned RMS values are computed. The statistical measures mentioned above are highlighted in green in Figure **??**, and the analysis below is mainly based on these measures.

Besides the mean and STD of the time series of orbit RMS listed in Table 4.1, the time series of scenarios 1, 2, 7, 14, 19, and 26 are shown in Figure 4.8. Correspondingly, the time series of the 1D-mean orbit improvements of scenarios 2, 7, 14, 19, and 26 compared to scenario 1 is shown in Figure 4.9. Generally, reduced orbit RMS and STD are achieved when increasing the number of ground stations or increasing the number of integrated LEOs. The GPS satellite orbit accuracy improves most when all the seven

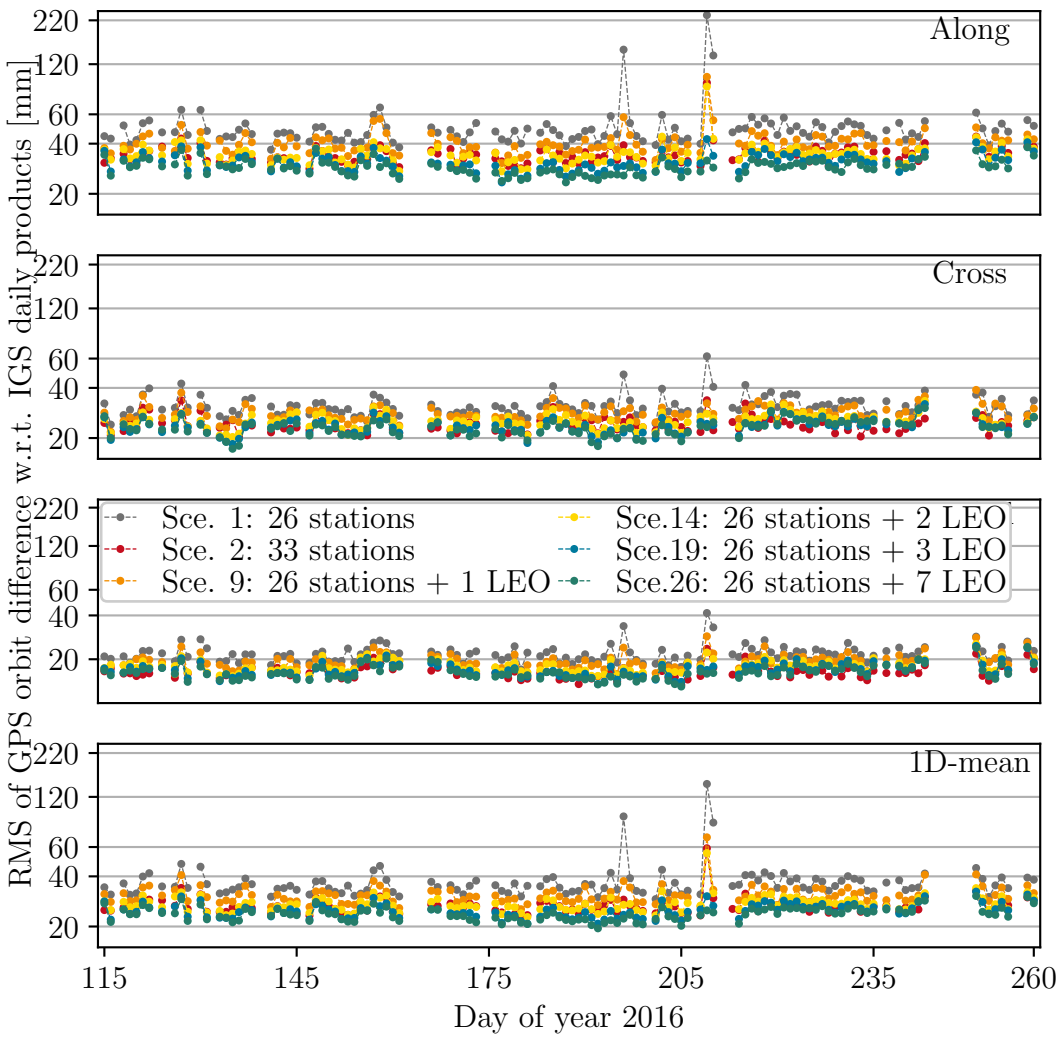

Figure 4.8: Statistical results of the GPS satellite orbit differences compared to the IGS final products of scenarios 1, 2, 7, 14, 19, and 26. The RMS of orbit differences in the along-track, the cross-track, and the radial directions are computed over epochs and satellites in each day. The 1D-mean RMS is computed over epochs, satellites, and the three orbital directions

LEOs are integrated into the POD (34%). In all scenarios, the orbit accuracy of the three directions is ranked as along-track < cross-track < radial, while the orbit improvements in the three directions are ranked in the reverse order (along-track > cross-track > radial). With only three LEOs integrated, the determined GPS satellite orbits of scenario 19 (28% improvement) are slightly better than those of scenario 2 (27% improvement) which includes seven additional and well-selected ground stations, with a stronger improvement mainly in the along-track direction. There are two peaks in all the plots. One is on DOY 196, and the other one is on DOY 209 and 210. These three days are presented as orange dots in Figure 4.4. After checking the residuals, we realized that the large RMS is caused by large errors in code measurements of a ground station (GODN). Since our data editing

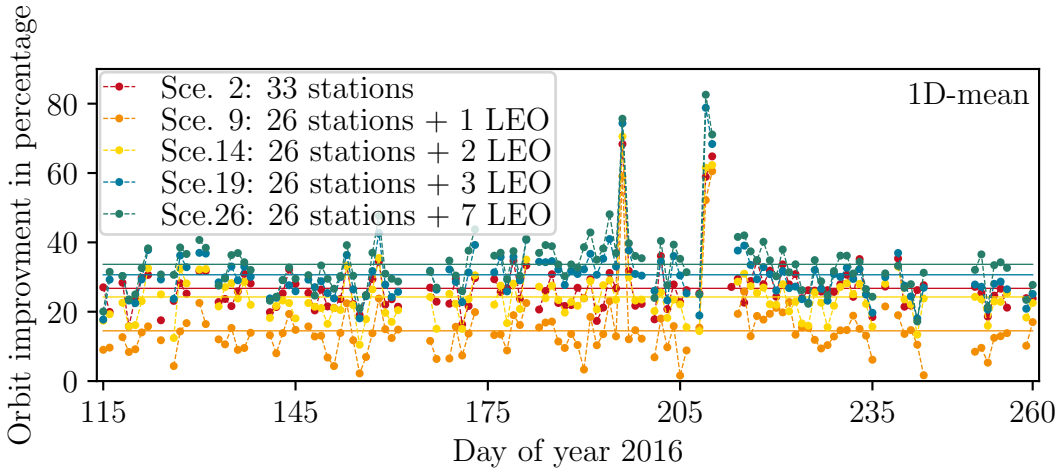

Figure 4.9: Improvements of the GPS satellite orbits derived by scenarios 2, 7, 14, 19, and 26 compared to scenario 1. The improvements are derived from 1D-mean RMS. Vertical lines indicate the averaged values

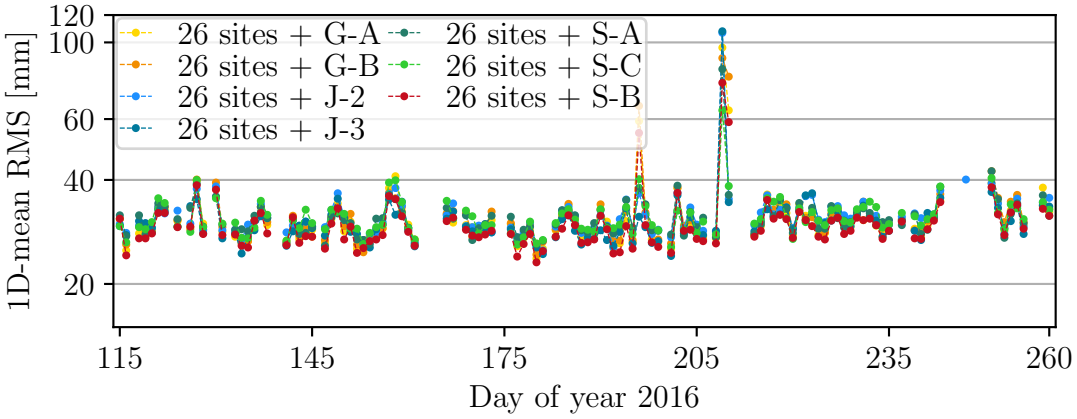

Figure 4.10: Statistical results of the GPS satellite orbit differences compared to the IGS final products of the one-LEO scenarios in time series. The RMS of orbit difference is computed over epochs, satellites, and three orbital directions (along-track, cross-track, and radial)

strategy is based on the residuals of the phase measurements, the station GODN with large residuals in its code measurements was not excluded. The GPS orbit improvements for these three days are more significant (about 50% to 82% in different scenarios) than for the other days (about 10% to 35%), and with only one LEO included, the improvement is close to the scenario including seven additional stations.

With only one LEO integrated (scenarios 3 to 9), the solutions are similar, for example, the 1D-mean RMS values vary slightly from 30.6 mm to 31.7 mm. Thus, compared to the 26-station only solution, the orbit improvements vary from 14% to 17%. However, the STD of the GPS orbit RMS of these one-LEO scenarios have larger differences (up to 4 mm in 1D-mean). As seen from Figure 4.10, there is no systematic difference between

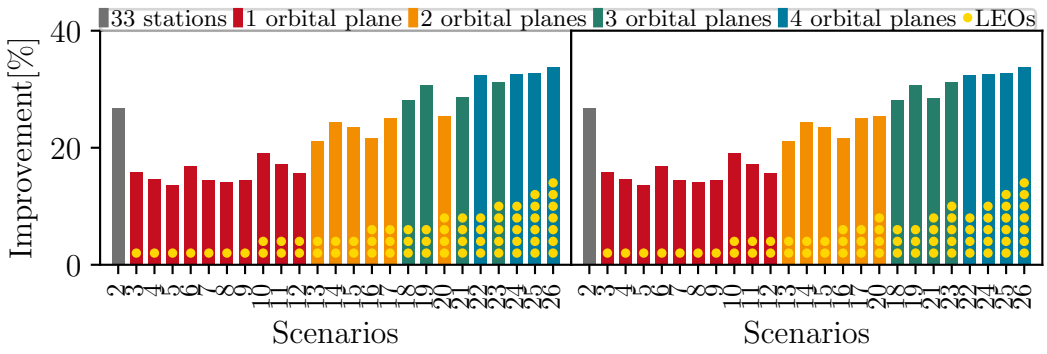

Figure 4.11: GPS satellite orbit improvements compared to scenario 1. The improvements are sorted with respect to the number of integrated LEOs (left) and the number of LEO orbital planes (right)

these one-LEO scenarios. The impact of different LEOs on the derived GPS satellite orbits is not visible.

Comparing the values given in Table 4.1 by considering the different LEO subsets, we find some phenomenons. In scenarios 10 to 15, two LEOs are included in the estimation. If the additional LEO is in the same orbital plane as the first one, the GPS orbit accuracy improves only by about 1 mm compared to the one-LEO scenarios (see scenarios 3 and 4 versus 10; 5 and 6 versus 11; 7 and 8 versus 12). Thus, the GPS orbit improvements compared to scenario 1 remain below 20% (16% to 19%). However, if the LEOs are flying in two different orbital planes, the orbit improvements compared to scenario 1 increase up to 24%, and the 1D-mean RMS values of the GPS orbits decrease to around 28 mm. By increasing the number of the integrated LEOs, the impact of the space-based observations and the LEO orbital planes on the derived GPS satellite orbits is getting more obvious. Figure 4.11 shows the orbit improvements sorted with respect to the numbers of LEOs (left) and the numbers of orbital planes (right). The number of integrated LEOs is marked with yellow dots, and the number of different orbital planes is represented by colored bars. As seen from the left plot, GPS satellite orbits improve generally by integrating more LEOs. However, the improvement does not correspond strictly to the increasing number of LEOs. For example, scenario 20 (with four LEOs in two orbital planes) includes one more LEO than scenario 19 (with three LEOs in three orbital planes), but the GPS orbit improvement of it is smaller (25% against 31%). This phenomenon happens also to the comparison between scenario 22 (with four LEOs in four orbital planes) and scenario 23 (with four LEOs in three orbital planes). When we sort the results by the number of LEO orbital planes, a clear trend is visible. One can see the increasing GPS orbit improvement related to the increasing number of LEO orbital planes from the right plot of Figure 4.11. In summary, the LEO orbital geometry is more important for the improvement of the GPS satellite orbits than the number of space-based observations. This summary also

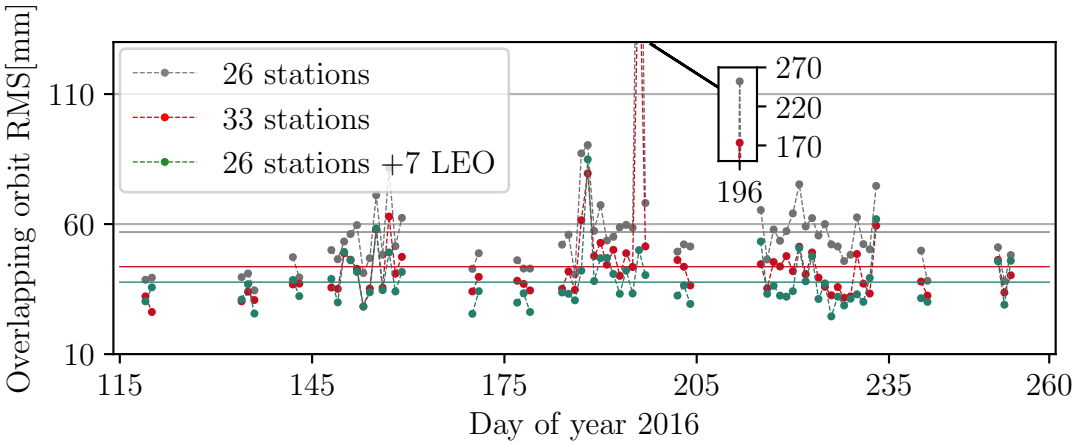

Figure 4.12: RMS of the differences between the 6-hour overlapping GPS satellite orbits computed over satellites and three orbital directions. The horizontal lines are the mean values of the time series

agrees with the discussion about Figure 4.2 based on observations only.

The positive effect of different LEO orbit geometries on the geocenter estimation is also given by some other studies, for example, the simulation study of the LEOs+GPS combined processing for geocenter estimation by Kuang et al. (2015) and the real data study on the geocenter variations derived from combined processing of the ground and space-based GPS observations by Männel and Rothacher (2017).

4.3.3 Internal comparison of GPS satellite orbits of three typical scenarios

Besides the external orbit comparison, internal comparisons are performed in two different ways. The typical three scenarios 1 (26 stations), 2 (33 stations), and 26 (26 stations and seven LEOs) are compared in this section. The first comparison is about the orbit overlaps. We expand the POD arc length of the three scenarios from 24 hours to 30 hours (three hours to both the previous and the next day). Consequently, a pair of 6-hour overlapping orbit arcs derived by real data processing is generated between two adjacent days. The 1D-mean RMS of the orbit differences of the 6-hour overlap is computed. Another comparison is about the satellite position differences at the day-boundary epoch of two adjacent 24-hour orbits at midnight. We extrapolate one more epoch from a 24-hour orbit by orbit integration, then the GPS satellite positions at the extrapolated epoch are compared with the estimated satellite positions in the first epoch of the next 24-hour orbit. The RMS of the satellite position differences is computed over the satellites and the three orbital directions at the day-boundary epochs. The main difference between the two approaches is whether common data is used for the two arcs.

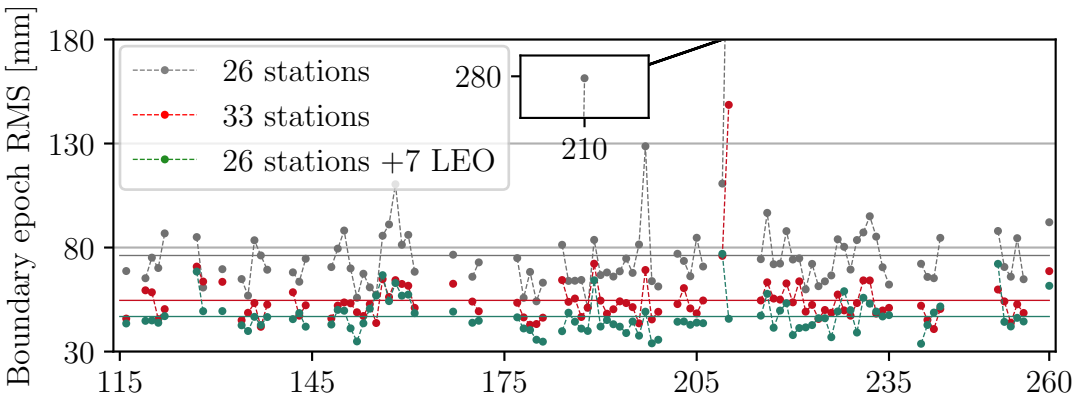

Figure 4.13: RMS of the GPS satellite position differences computed over satellites and three orbital directions at the day-boundary epoch between two 24-hour arcs. The horizontal lines are the mean values of the time series

Due to the excluded days mentioned above and the overlapping processing strategy, only 65 pairs of overlapping orbits with a 6-hour arc length are available for comparison. Figure 4.12 shows the 1D-mean RMS of the differences between the overlapping orbits. Seen from the time series of the three scenarios, the differences of the overlapping orbits are ranked as scenarios $1 > 2 > 26$, and the mean and STD of the overlapping orbit differences computed over 65 days are 57 ± 27 mm, 44 ± 19 mm and 38 ± 10 mm.

There are 92 day-boundary epochs between the processed 112 days. The GPS satellite position differences in these day-boundary epochs are plotted in Figure 4.13. The mean and STD of the results computed over the 92 epochs are 76 ± 25 mm, 55 ± 12 mm, and 50 ± 8 mm in scenarios 1, 2, and 26, respectively. This plot agrees with the comparison of the overlapping orbits in Figure 4.12 and the external orbit comparison in Figure 4.8. The outliers in Figures 4.12 and 4.13 are caused by the observation errors of station GODN which have been mentioned in the previous section.

4.3.4 Geolocated visualization of orbit comparison

Based on a geolocated comparison of epoch-wise satellite orbit differences (orange box in Figure **??**) between scenarios 1, 2, and 19, we will discuss the different effects of supplementing a sparse station network with additional stations and LEOs below. Thanks to the orbit dynamics, continuous observations for each satellite are not needed. In the introduction of the selected ground networks, we explained that the seven additional stations in scenario 2 were selected in the regions with few stations in scenario 1. For the analysis regarding station distributions, the GPS satellite orbit improvements of scenarios 2 and 19 compared to scenario 1 are projected to the surface of the Earth. Based on the epoch-wise orbit difference of each GPS satellite compared to the IGS final products, we

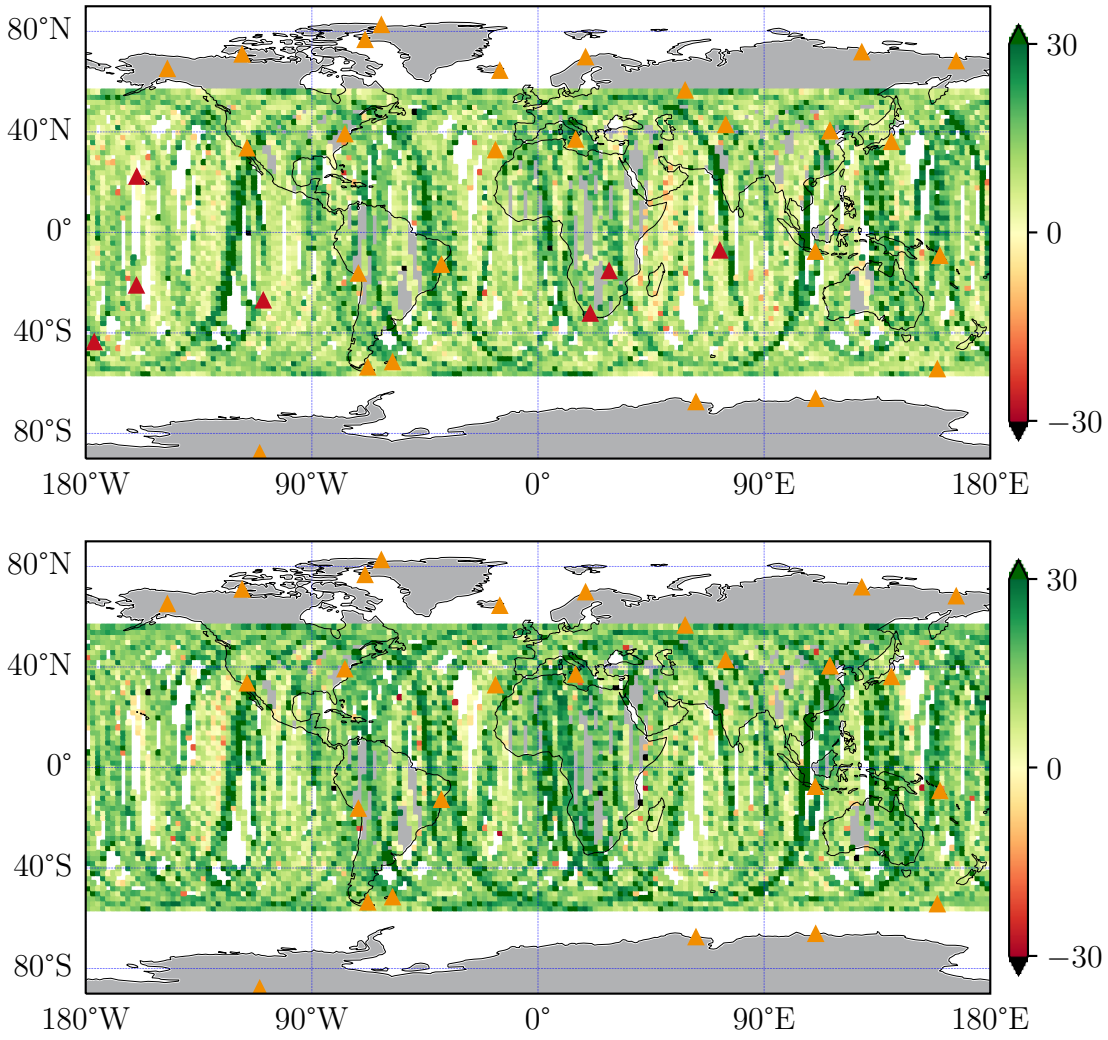

Figure 4.14: GPS satellite orbit improvements of scenarios 2(upper) and 19(lower) w.r.t. scenario 1. IGS final products are reference. The color of each bin presents the average value of the epoch-wise solutions located in the bin. The unit of the color bar is [mm]

computed the improvements of the GPS satellite orbits of scenarios 2 and 19 compared to scenario 1 with a 900-second sampling rate for all GPS satellites in 112 days (approximate 344,064 epoch-wise solutions). The results are presented in Figures 4.14. In these two figures, the potential GPS satellite position area is divided into geographical $2° \times 2°$ bins (10,260 in total). We computed the average of all the epoch-wise solutions located in the same bin. These geolocated statistical results are presented as the color of the corresponding bins. Green means the satellite orbits are closer to the IGS final products (improvement), and red means that differences get larger (degradation). Additionally, the ground tracks of GPS satellites are also visible in the plots.

In general, with seven well-selected additional stations (scenario 2) or three LEOs (scenario 19), the GPS satellite orbits improve globally (as indicated by the green bins). The improvements are more clearly presented in Figure 4.15. The density distributions of

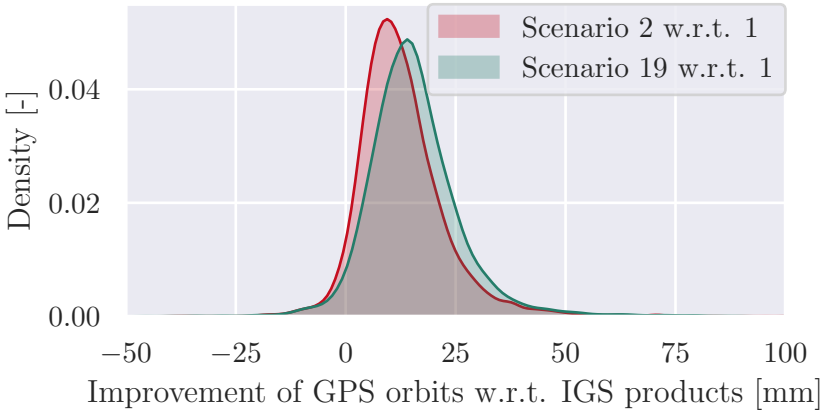

Figure 4.15: Density distributions of all the epoch-wise solutions of satellite orbit improvements from scenario 1 to scenario 2 (red) and 19 (green). Positive means getting closer to the IGS final products

all the epoch-wise solutions from both comparisons are mainly positive. However, there are still regions without significant improvement (as indicated by the yellow bins), and there are only a few bins in red with degradation caused by the additional observations. Comparing the two plots in Figure 4.14, there are more dark-green bins and fewer red bins in the plot of scenario 19. Correspondingly, the density distribution of the epoch-wise solutions of scenario 19 is located on the right of that of scenario 2 in Figure 4.15. Therefore, compared to scenario 1, the GPS satellite orbits derived in scenario 19 improve more than those of scenario 2. Especially in some regions of the Pacific Ocean, the Indian Ocean, and Africa, seen from the color of the bins, the improvement of scenario 19 is more significant than that of scenario 2. In summary, to a sparsely and non-homogeneously distributed network of ground stations, the derived GPS satellite orbits are improved more by supplementing the network with three LEOs in different orbital planes than with seven well-located additional stations, especially for the orbit arcs above the regions lacking stations.

4.3.5 Results about regional station network

An additional experiment is discussed below to show the GPS satellite orbit improvement by supplementing a small and mainly regionally distributed station network with seven LEOs. Figure 4.16 represents the network with five stations in China and another five stations in other regions. The figure shows that about two-thirds of potential GPS satellite positions ($2^\circ \times 2^\circ$ resolution, 20,200 km altitude) can be observed by only two or even fewer stations. The GPS-only and seven-LEO-integrated POD were performed with this network. The 1D-mean RMS of the GPS satellite orbit differences compared to the IGS final products are presented in Figure 4.17. Enhanced by seven LEOs, the 1D-mean RMS

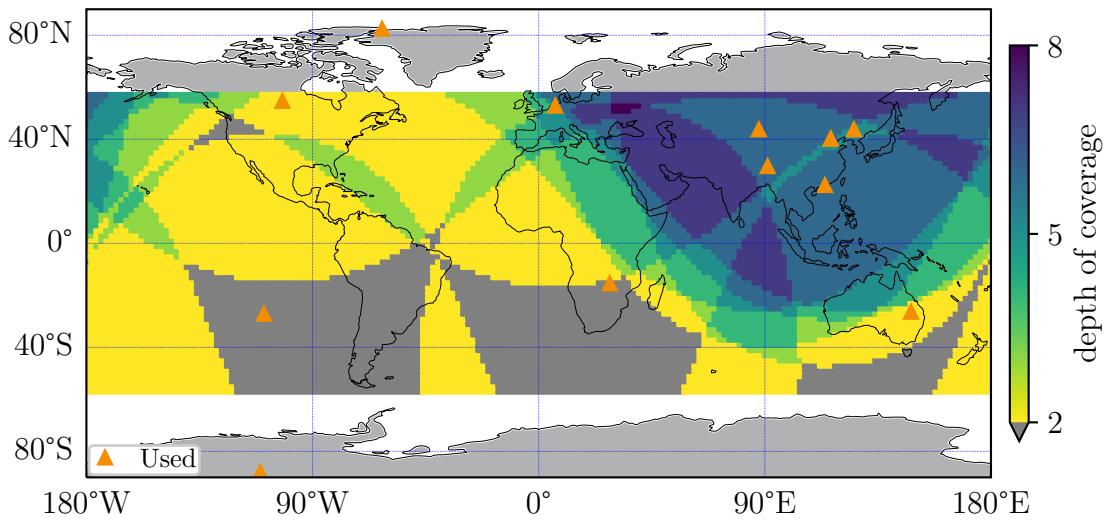

Figure 4.16: A subset of the available IGS stations including five stations in China and five stations in other regions. The station visibility from a potential GPS satellite position (Depth of Coverage) is presented as a colored bin ($2° \times 2°$ resolution, 20,200 km altitude)

decreases significantly from about 25 cm to 4 cm. Also, the variations of the time series are reduced significantly from about 4.3 cm to 0.7 cm. The GPS orbit improvement by integrating LEOs to a regional ground network was also demonstrated by Wang et al. (2016) with seven stations within China and three LEOs (GRACE-A/B and FengYun-3C). We also performed a test of just using five stations in China. To get an acceptable result, the number of observations should be increased by expanding the arc length to three days and increasing the sampling rate to 30 seconds. The derived GPS satellite orbits differ from the IGS final products by about 20 cm in 1D-mean RMS, but the LEO orbits degrade significantly. Further studies should be done to improve the solution in this situation.

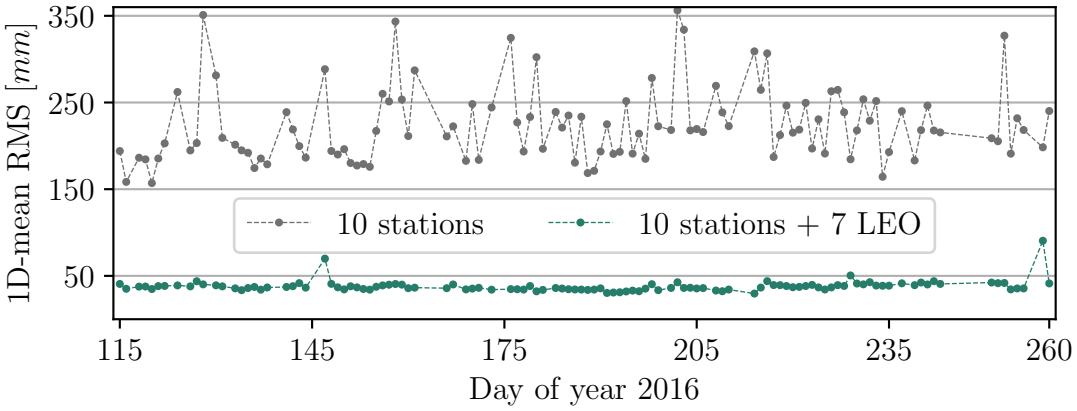

Figure 4.17: GPS satellite orbit RMS from POD with and without LEOs (comparison against IGS final products)

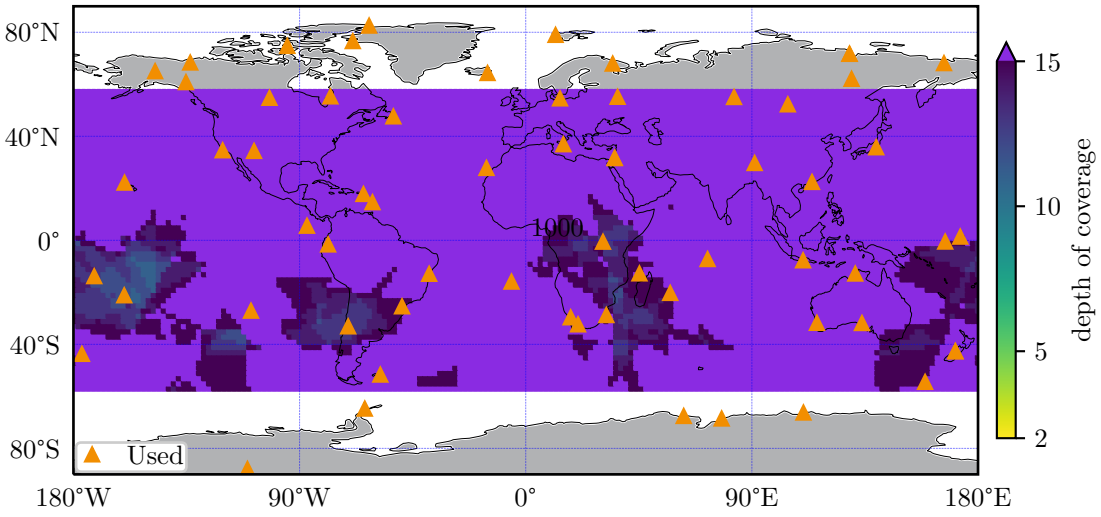

Figure 4.18: A dense subset of the IGS ground stations with 62 globally distributed stations

4.3.6 Comparison between LEOs integrated solution and 62-station based solution

Although the focus of this study is on improving the GPS satellite orbits derived from limited ground networks, we also presented the quality of the GPS satellite orbits derived from a 62-station globally distributed network as a reference for interested readers. The network distribution and the GPS satellite orbit comparison with scenario 26 are given in Figures 4.18 and 4.19. With 62 well-distributed ground stations, the DOC of the major region is larger than 15 (>10 in all coverage). The GPS orbit is improved in all directions than the solution of 26 stations and seven LEOs. However, the two solutions are still comparable.

4.4 Summary and feasibility of relevant topics

Based on the results and discussion of Section 4.3, the POD of GPS satellites can be improved by including LEOs due to the additional observations and geometries offered by the LEOs, especially when there is no additional station available. The benefit of integrating LEOs into the POD is convincing for a sparse or regional network. The GPS satellite orbits are improved more by supplementing a sparse ground network with LEOs than with comparable numbers of additional stations. By integrating three LEOs in three different orbital planes into the POD, the determined GPS satellite orbits (25.1 mm 1D-mean RMS compared to the IGS final products) are more accurate than those of the scenario with seven carefully selected additional ground stations (26.7 mm

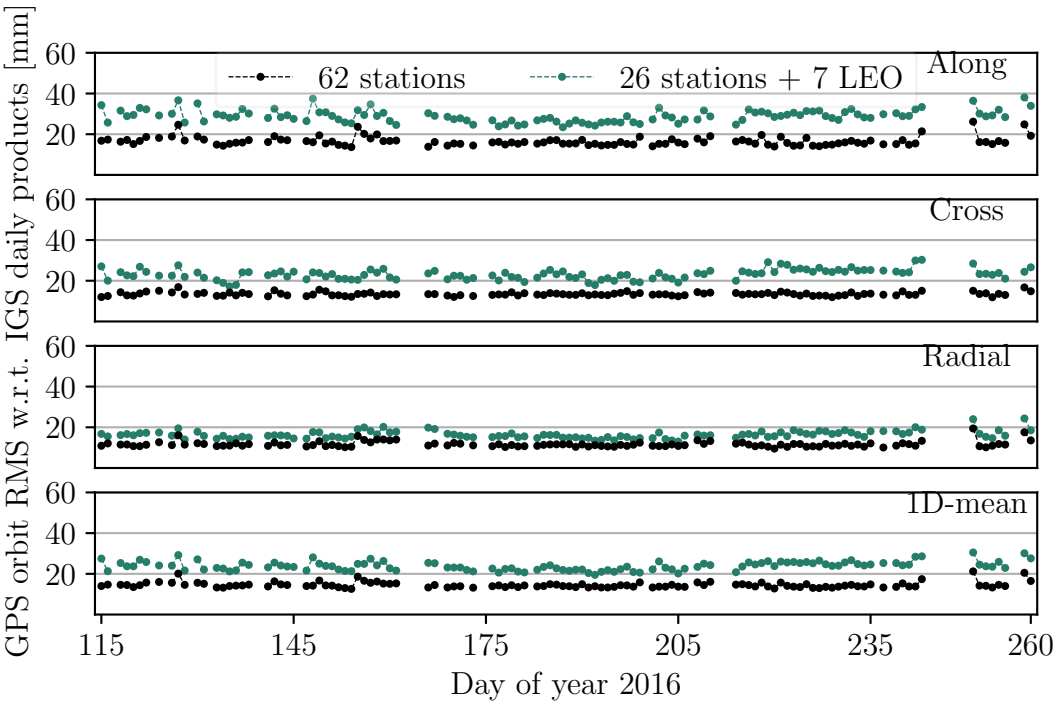

Figure 4.19: Statistical results of the GPS satellite orbit differences w.r.t. the IGS final products of 62-station scenario and 26-station+7-LEO scenario. The RMS of orbit differences in the along-track, the cross-track, and the radial directions are computed over epochs and satellites in each day. The 1D-mean RMS is computed over epochs, satellites, and the three orbital directions

1D-mean RMS). The benefits of adding LEOs do not correspond strictly to the number of the integrated LEOs but the diversity of their orbit planes. With the LEOs in different orbital planes, the GPS satellite orbits are improved. It is also expected by the analysis merely based on observations status in Section 4.2. Ground stations might bring some undetectable outliers in the observations, especially in sparse networks with less redundancy. In general, the effect of these bad observations can be reduced with more ground stations or LEOs. The mitigation with LEOs introduced is more significant than with more ground stations added. By integrating seven LEOs, the GPS satellite orbits derived from a 10-station and regional ground network are improved impressively with decreased 1D-mean RMS compared to IGS final products from about 25 cm to 4 cm. The impact of LEO orbit modeling quality on derived GPS satellite orbits is not discussed in this study.

Beyond this study based on real data in history, and outlook for the integrated POD can be given based on some recent studies by simulations and the current technical feasibility. Li et al. (2019b) simulated the integrated POD of large LEO constellations and multi-GNSS. Significant improvement of the GNSS orbits is shown, especially for the BeiDou GEO satellite orbits (cm-level accuracy achieved) due to tremendous variations in

tracking geometry bought by the large LEO constellations. LEOs fly in sun-synchronous orbits improve the GNSS orbits more than the LEOs in polar orbits. However, Li et al. (2019b) were confronted with long computation time even they used the super-computing system in the Supercomputing Center of Wuhan University. This is caused by a large number of integrated LEOs. Considering the improvement by including different numbers of LEOs and the current computation power, they suggested that including 40 LEOs in sun-synchronous orbits is a balanced solution. Improvements in the POD algorithm are expected. Seeing from Figure 2.7 and Table 2.2, only more than 20 LEOs equipped with GNSS receivers are in operation and most of them fly in polar orbits. Therefore, the state-of-art computation ability is capable of the current status of integrated POD. More LEOs equipped with GNSS receivers are expected for the future. Whether the LEOs can augment the positioning and navigation applications of GNSS is another trending topic. Again based on simulation, Li et al. (2018a); Ge et al. (2018); Li et al. (2018b) studied the contribution to the rapid convergence of precise point positioning (PPP) by including large constellations of LEOs. The LEOs are simulated to receive signals from upper GNSS satellites and transmit signals down to ground stations. The convergence time of PPP and the coverage of GNSS, especially in polar regions, improve significantly. However, the existing LEO constellations e.g., OneWeb, Iridium, and Starlink are not feasible to be adapted to the GNSS due to the different signals. Some deeper discussions about the feasibility of OneWeb for positioning are given by Ramsey and Ziebart (2020). As mentioned in Chapter 1, the 'Kepler' constellation (Giorgi et al., 2019) could be a good solution for the LEO-enhanced GNSS in the next generation.

Estimation of GPS PCOs and GNSS-based Earth parameters

Besides the improvements of GNSS satellite orbits, the additional LEOs observations can also contribute to the determination of other parameters related to GNSS, for example, geodetic parameters including the Earth gravity field (König et al., 2005) and geocenter (Kuang et al., 2015; Männel and Rothacher, 2017). In this study, the LEOs are integrated with GNSS satellites to determine GPS PCOs, GNSS-based terrestrial scale, and GNSS-based geocenter. Section 5.1 gives a detailed introduction of the current status and the previous studies. Especially, the different issues related to the horizontal (x- and y- directions) and vertical (z-direction) components of GPS PCOs are discussed in detail. For the GPS PCOs in z-direction which is correlated with the terrestrial scale, two approaches are capable for the estimation. One is based on the LEOs and the other one is based on Galileo (Villiger et al., 2020). The two approaches are introduced in Section 5.2. Due to the aim of this study, the new implemented datum definition in PANDA software is discussed in Section 5.3. In Section 5.4, a study based on real observations in 2016 is carried out to analyze the estimated GPS PCOs in x-,y-, and z-directions by integrating LEOs. To compare and cross-check the estimated GPS PCOs in the z-direction and the GNSS-based terrestrial scale by using the LEOs-based method or the Galileo-based method, a study based on real observations in 2019 is presented in Section 5.5 and it has been published in GPS Solutions(Huang et al., 2021). Some results of geocenter estimation by the two methods are shown in Section 5.6. Section 5.7 gives a summary for this chapter.

To improve readability, the following naming convention is used. PCOs describe the offset between the center of mass and mean transmitting point onboard the spacecraft and the offset between the antenna reference point and mean receiving center for receiving antennas. The PCOs in three directions of the satellite system are denoted by x-, y- and z-PCO. The nadir (and azimuth) dependent deviations from the mean transmitting or receiving point is described by PVs, which are nadir and azimuth or elevation and azimuth dependent, respectively. Transmitter phase centers are identified by the satellite system in a superscript (e.g., $\mathrm{PCO}^{\mathrm{GPS}}$). Receiving antennas are indicated by subscripts (e.g.,

$\mathrm{PCO}_{\mathrm{LEO}}$). The estimated PCO differences in the z-direction with respect to the a priori values are indicated by z-ΔPCO, e.g., z-$\Delta\mathrm{PCO}^{\mathrm{GPS}}$ and z-$\Delta\mathrm{PCO}_{\mathrm{LEO}}$.

5.1 Current status and previous studies

The importance of GNSS antenna phase center calibrations became evident in the early 2000s when GPS based TRF started to show significant scale biases and trends. In the early years of the GNSS, Malla and Wu (1989) predicted that daily GPS-only geocenter offset estimates based on small networks could reach centimeter accuracy. Driven by the growing space and ground segment and advances in processing GPS, Heflin et al. (2002) presented an independent GPS-based TRF agreeing with the ITRF 2000 at the level of 1 cm and 1 ppb (part per billion) in origin and scale, respectively. The long-term stability of this TRF was found to be 6 mm/yr for the origin and 0.6 mm/yr for the scale (on the Earth surface). However, further studies reported unreliable scale rates. For example, Ge et al. (2005) determined an increased rate of 6 mm/yr. The reason, as found out by Zhu et al. (2003) and Ge et al. (2005), was the insufficient knowledge about the antenna offsets of the GPS Block IIR satellites. These satellites were launched from 1997 onwards to replenish the aging GPS constellation. This step-wise replenishment caused the discovered trend in the derived scale time series (Ge et al., 2005). Vertical network distortions of 6-12 mm and errors in the vertical velocities of 1-2 mm/yr resulting from the evolution of the GPS constellation and inaccurate PCOs were quantified in simulations (Cardellach et al., 2007). Unfortunately, the position of the transmitting point is usually not disclosed by the GNSS providers. For some recently launched satellites, ground calibrated PCOs are now provided, e.g., for Galileo, BeiDou-3, QZSS, and GPS III. The uncertain PCOs/PVs of most currently and formerly operational GNSS satellites was estimated in global adjustments (e.g., Schmid and Rothacher, 2003; Schmid et al., 2005; Dilssner et al., 2011; Steigenberger et al., 2016). By using these corresponding PCOs and PVs, GPS-based TRFs with increased accuracy were published, for example, by Rülke et al. (2008).

The current standard of the IGS to determine GNSS satellite antenna offsets and variations is based on the processing of a global GNSS ground station network (Schmid et al., 2016). Due to the high correlation between station height, troposphere delay, and the offsets of transmitting and tracking antennas, accurate calibrations of the tracking antennas are a prerequisite for estimating the transmitting antenna offsets. The corresponding robot-calibrations are provided in the International GNSS Service (IGS) antenna exchange format (ANTEX). Moreover, thanks to a recent effort by Geo++, signal-specific including Galileo frequencies and multi-GNSS calibrations are available for many receiver antennas used within the IGS tracking network, for example, in the

ANTEX file for IGS repro3 *igsR3_2057.atx* provided by (Villiger, 2019). In addition, the terrestrial scale had to be fixed, for example, to the current ITRF solution, to avoid a poorly conditioned normal equation system with less precise estimates. However, this approach suffers from three considerable limitations:

- the derived transmitter offsets and any further derived geodetic products are not independent of this ITRF scale;
- the absolute antenna phase patterns of the ground tracking sites are contaminated by local environmental effects such as time-variable multi-path;
- tropospheric delays have to get estimated simultaneously for each ground station.

The most important issue is the first one mentioned in this list. Stations of a global tracking network observe GNSS satellites only within a very limited range of nadir angles of up to 14°. This unfavorable geometry causes a strong correlation between station height, tropospheric delays, satellite clock parameters, and z-PCO. As a consequence, the derived z-PCO are highly correlated with the terrestrial scale. Zhu et al. (2003) reported a relationship that 130 mm error in GPS z-PCO$^{\mathrm{GPS}}$ leads to one ppb terrestrial scale. For deriving the satellite PCOs and PVs in the IGS, this problem is solved by fixing the coordinates or by applying a no-net-scale condition to a selected set of core stations with respect to the ITRF. Consequently, the scale information from VLBI and SLR is introduced into the GNSS antenna patterns and, therefore, transferred into any further GNSS solution. As mentioned by Haines et al. (2015) the derived GNSS-based TRF realizations are, therefore, no longer fully independent of other space geodetic techniques. Theoretically, GNSS can provide a terrestrial scale thanks to (1) centimeter-level accurate satellite orbits (Männel, 2016) and to (2) the precision of the GNSS phase measurements (observation error less than 2 mm). However, to link both orbit and observation, information is required about the transmitting point (reference for the observation) with respect to the satellite center of mass (reference for the orbit). Obviously, an unconsidered offset in the radial direction (i.e., in the z-direction of the spacecraft body-fixed frame) will shift the determined station heights and bias the eventually estimated terrestrial scale parameter. Therefore, once the z-PCO of GNSS satellites can be determined accurately and independently of other techniques, the pure GNSS-based scale can be determined.

For the horizontal components of the phase center offset (i.e., x-PCO and y-PCO), the commonly known yaw-steering mode introduces some limitations to their estimation. Figure 5.1 shows this attitude law. The z-axis of the satellite body system coincides with the antenna direction pointing towards the Earth. The y-axis is parallel to the rotation axis of the solar panels, and the x-axis is perpendicular to the y-axis and z-axis, such that the +x panel is illuminated by the Sun. Schmid et al. (2007) present the low

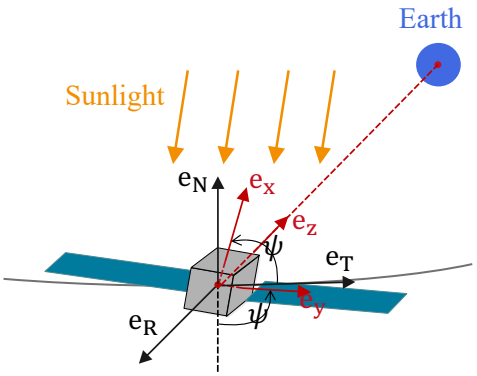

Figure 5.1: GPS satellite attitude (yaw steering model in large solar elevation angle moment). e_x, e_y, and e_z present the axes of the satellite body fix system. e_R, e_T, and e_N are the unit vectors in radial, transverse, and normal directions of the orbital reference system. The angle ψ is the nominal yaw angle

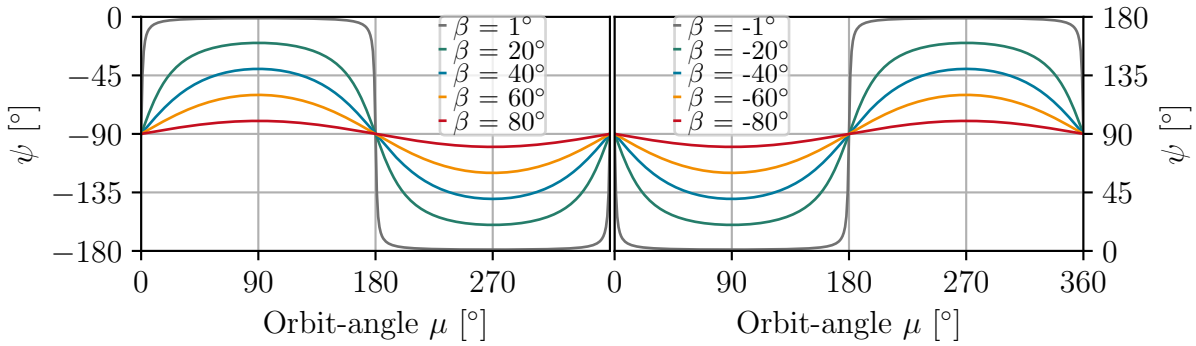

Figure 5.2: Yaw angle variation during one full orbit (expressed by the orbit angle μ measured from orbit midnight) w.r.t different orbital β angles

precision of x/y-PCO during the period of large β angle (the angle between the orbital plane of the satellite and the vector to the Sun). As pointed out by Schmid (2009), it is impossible to separate a satellite antenna offset component from an along-track orbit error if the corresponding axis orientated parallel or anti-parallel to the along-track direction, i.e., the nominal yaw angle (ψ; the angle between the transverse direction of the orbital reference system and the x-axis of the satellite body fix system) is around 0°, ±90° or 180°. This problem is dissolved if the ψ angle has a large variation during the estimation period. However, the ψ angle varies slightly around ±90° during one full orbit period when the β angle is large (cf. Figure 5.2). The low x/y-PCO precision mentioned above is due to the strong correlation with the orbit in the large β angle period. Besides the correlation between the x/y-PCO and the satellite orbit and attitude, the x-axis being close to sunlight direction brings additional effects, as discussed in terms of Galileo by Steigenberger et al. (2016). They reported a strong correlation between the empirically estimated coefficient D_0, constant part of the acceleration in Sun's direction, and the x-offset estimates. This correlation is visible also as an effect between the x-PCO and β angle.

Consequently, the aspects need to be discussed in the following. One is about determining the scale-independent z-PCO$^{\mathrm{GPS}}$ and the GNSS-based scale. The other one

is about the improvement of x/y-PCO^{GPS} estimates. Several previous studies about the estimation of the GPS antenna phase centers by integrating low Earth orbiters (LEOs) have been published. Haines et al. (2004) estimated GPS satellite antenna PVs from Jason-1 and GRACE observations to improve their Jason-1 orbit determination. Apart from improvements in the derived Jason-1 orbit solution, they found decreased RMS values for independent GPS observations when applying the derived GPS satellite PVs. Haines et al. (2015) provided GPS satellite PVs and an independent TRF solution based on GRACE-B and GPS observations of ground stations. Their solutions cover the years between 2002 and 2012, while they additionally provide a solution based on TOPEX/Poseidon GPS observations from 1993. Based on the a priori LEOs receiver patterns the derived GPS transmitter PVs agreed well to the IGS patterns and a robot-based calibration of the Block II/IIA antenna (Wübbena et al., 2007). Jäggi et al. (2011) presented GPS transmitter patterns for nadir angles of up to 17° derived from LEO-observation-only processing including GRACE-A/B, OSTM/Jason-2, MetOP-A, and GOCE. Comparing the derived transmitter PVs to the igs08.atx a good agreement at the level of 2 mm was shown. However, they constrained the PVs of two GPS satellites in Block IIA to their *igs08.atx* values due to the simultaneous estimation of LEOs PVs by using only LEOs observations. Dilssner et al. (2011) determined both GPS PVs and LEOs PVs from combined processing of GPS data obtained at ground stations, on Jason-1, and on OSTM/Jason-2. They found a good agreement between the derived satellite antenna PCO/PVs and the corresponding IGS solutions for nadir angles below 14°. When introducing the derived satellite PVs, which were estimated for nadir angles of up to 17°, the RMS of the phase residuals for the orbit determination dropped from 7.2 mm down to 6.5 mm. Similar studies were also performed to calibrate the GNSS transmitting antennas within the concept of co-location in space, for example, the work of Männel (2016), which incorporated GRACE, GOCE, and OSTM/Jason-2 satellites and the preparing study of the GRASP and E-GRASP/Eratosthenes missions (Bar-sever et al., 2007; Biancale et al., 2017).

Besides the method of adding LEOs, joint processing of GPS and a GNSS with calibrated antennas is another approach to determine the scale-independent z-PCO^{GPS}. In October 2017, the European GNSS Agency (GSA) released a comprehensive set of satellite metadata for the Galileo FOC satellites. The available data set includes spacecraft properties, optical surface characteristics, the attitude law, and the PCOs/PVs. Together with similar information released for the IOV satellites in December 2016, for the first time, this information became available for a whole GNSS. Since then, several studies have discussed resulting improvements in the geodetic analysis (Bury et al., 2019; Katsigianni et al., 2019; Zajdel et al., 2019; Li et al., 2019a). The Galileo-based approach to determine the scale-independent z-PCO^{GPS} is introduced and discussed later in detail. xx

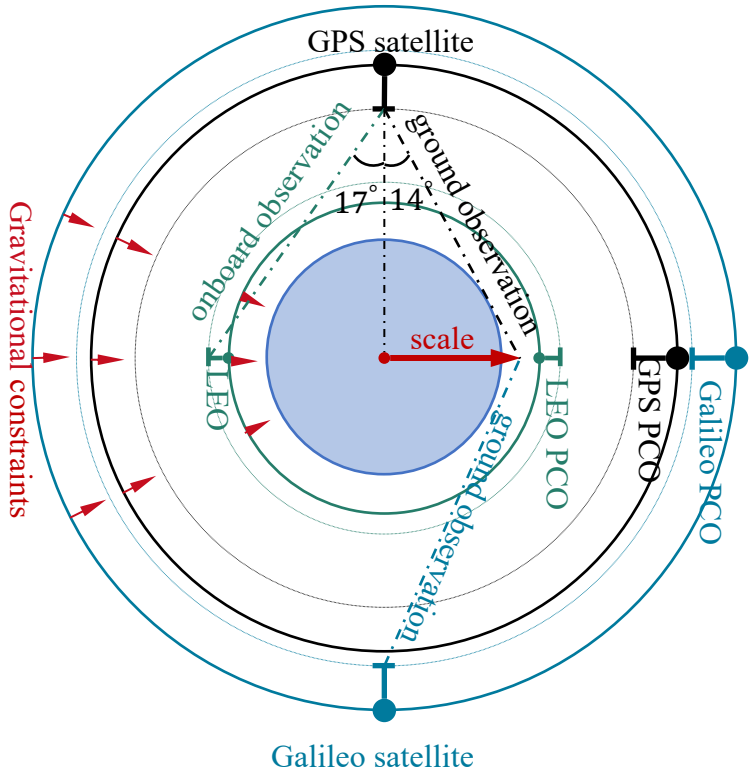

Figure 5.3: Schematic diagram of the two methods of determining scale-independent GPS z-PCO

5.2 Two methods of z-PCO^{GPS} estimation and scale determination

This section describes two different methods used to derive the z-PCO^{GPS} and GNSS-based scale. Both approaches rely on additional observations, either ground Galileo observations or GPS observations onboard LEOs. Figure 5.3 presents the basic setup consisting of ground stations, GPS and Galileo satellites, and LEOs. Ground-based and space-based observations connect the antenna phase center of different transmitters and receivers. The estimated coordinates of the ground station network have a scale factor with respect to the a priori coordinates. The scale is not subject to the gravitational constraint, while GNSS satellite and LEO orbital positions derived by a dynamic precise orbit determination have a negligible sensitivity to the scale (Haines et al., 2015).

5.2.1 Method I: Integrated processing with LEOs

The principle benefit of space-based GNSS observations for the estimation of transmitter antenna phase centers is given by dynamic constraints on the receiver, i.e., the LEOs

positions. This so-called gravitational constraint is based on the third Keplerian law that reads as $n^2a^3 = GM$, where a is the semi-major axis of the satellite orbit. The mean motion of the satellite is described by n, which is derived from the orbital period T by $n = 2\pi/T$. Considering a realistic relative accuracy of 0.5 ppb for the geocentric gravitational constant GM, the related error in the semi-major axis amounts to 1 mm for a satellite in 1000 km altitude as mentioned by Haines et al. (2015). GM is introduced according to the IERS2020 conventions (Petit and Luzum, 2010) as constant. Consequently, the satellite's semi-major axis is constrained, since n is defined by the orbit dynamics and measured with a relative accuracy of around 10^{-10}. The corresponding partial derivative reads as

$$\frac{\Delta n}{n} = -\frac{3}{2}\frac{\Delta a}{a}. \tag{5.1}$$

This equation relates an error Δn in the mean motion to an error Δa in the semi-major axis. However, also uncertainties in the Earth's orientation could affect the measured orbit period. Haines et al. (2015) estimated that a 10 μs error in the orbit period amounts to an error of not more than 4 mm in a. The relationship between an error in the semi-major axis and an error in the along-track direction Δs reads as

$$\Delta s = \Delta n T a \Leftrightarrow \frac{\Delta n}{n} = \frac{\Delta s}{2\pi a}. \tag{5.2}$$

From Equation (5.1) and (5.2), the relationship between the error in the semi-major axis and the error in along-track for one revolution reads as

$$\Delta s = -3\pi\Delta a. \tag{5.3}$$

Under the assumption that orbit dynamics are appropriately modeled, Δs will be small. Modeling deficiencies concerning non-gravitational forces will influence the semi-major axis by not more than 1-2 cm. Therefore, Δa is well calculated during the orbit determination process. Overall the geocentric receiver position is, assuming a dynamic orbit representation, determined on the centimeter-level without any sensitivity to the scale. However, the considerations made here for LEOs are, in the strict sense, valid for the dynamic orbit representation only, as the pseudo-stochastic pulses that are commonly estimated distort the direct relationship between Δa and Δs. Fortunately, as mentioned in Section 2.5.2, a more dynamic approach (without estimating accelerations in radial-direction) is applied for the LEOs in this study. Consequently, the solutions of this study are more reliable than that of Männel (2016) by using a reduced dynamic approach. Based on the theory mentioned above, the estimation of scale-independent z-PCO^{GPS} becomes possible by adding LEOs. Consequently, a GNSS-based scale is achievable.

Beyond the de-correlation of the transmitting antenna phase center and the scale,

estimating the corresponding patterns from LEO-based observations provides some more benefits as mentioned, for example by Dilssner et al. (2011). First of all, LEOs GNSS observations are not influenced by the troposphere, whereas for ground stations the high correlation between station height, the radial component of the GPS orbits, tropospheric delay, antenna parameters, and satellite and receiver clock errors have to be resolved. Additionally, due to the missing troposphere, there is in principle no need to set an elevation cut-off angle. However, due to spacecraft-specific near-field multi-path, a low cut-off angle, of e.g., 3°, might be useful as recommended by Jäggi et al. (2009). Secondly, the rapidly changing geometry between LEOs and GNSS constellation improves the GNSS orbit determination (Huang et al., 2020) and, thus, also the estimation of transmitting patterns. Thirdly, also related to changing geometry, GNSS receivers onboard LEOs allow to sample signals from all parts of the transmitting antennas within a comparably short time. Fourthly, the already mentioned increased nadir coverage is an additional benefit, for example, at the altitude of OSTM/Jason-2 ($\approx 1350\,km$), signals transmitted at nadir angles of 17° can be tracked. Thanks to the benefits mentioned above, including LEOs can improve the precision of the estimated x/y-$\mathrm{PCO}^{\mathrm{GPS}}$.

However, there are three major limitations to this method. Firstly, there are not enough space-based observations to solve for all parameters (z-$\mathrm{PCO}^{\mathrm{GPS}}$, LEO orbits, GPS orbits, etc.) together in one run. Moreover, a connection to the Earth is always needed. Therefore, ground- and space-based observations have to be combined. This approach is known as an integrated or one-step approach and has been studied for the past 15 years. It was already used to determine z-$\mathrm{PCO}^{\mathrm{GPS}}$ by Haines et al. (2015) and Männel (2016). To transfer the scale constraint offered by the space-based observations requires a fully consistent estimation of GNSS satellite orbits and clocks which link ground- and space-based observations. The second limitation is the availability and quality of the space-based observations. According to Figure 2.7, very limited LEOs obtained GPS observations simultaneously in history. However, as long as possible processing period is required to estimate the $\mathrm{PCO}^{\mathrm{GPS}}$ precisely. And thirdly, an error in the a priori calibrated z-$\mathrm{PCO}_{\mathrm{LEO}}$ can significantly bias the derived z-$\mathrm{PCO}^{\mathrm{GPS}}$. A simulation study by Glaser et al. (2020) regarding the future GNSS constellation 'Kepler' (Giorgi et al., 2019) gives a positive blueprint for this approach. Kepler has a constellation including 24 MEO satellites and six LEOs. Moreover, it has two-way optical inter-satellite links (ISL) and optical frequency references. The constellation and new techniques can both contribute to this approach. According to the results of this simulation study, 1 mm level accuracy of $\mathrm{zPCO}_{\mathrm{LEO}}$ is required to grantee the accuracy of the estimated z-PCO of MEO satellites and the corresponding scale in 1 mm accuracy at the equator. In reality, the available $\mathrm{PCO}_{\mathrm{LEO}}$ values are normally ground calibrated, for example in a chamber. However, it is very difficult to validate their accuracy, especially considering the different environments

in space and on the ground.

5.2.2 Method II: Joint processing with Galileo

Thanks to the release of the metadata of all Galileo satellites and the signal-specific calibration of phase center for many receiving antennas used within the IGS tracking network, a Galileo-based scale becomes achievable. However, with the first operational Galileo satellites launched in 2012, a corresponding Galileo-only solution could cover only the most recent years (i.e., from 2017 onwards). To process a long-time solution and determine the terrestrial scale back in time, the PCOs, which are independent of the terrestrial scale derived by other techniques such as VLBI and SLR, are still required for GPS and GLONASS. Therefore, another approach for the z-PCO^{GPS} estimation based on GPS+Galileo joint processing is important. With the PCO^{GAL} fixed to the calibrated values provided by the GSA, a reliable scale-independent solution is achieved. Consequently, as GPS and Galileo are observed by the same stations whose coordinates are now estimated scale-independent from the underlying reference frame, also the PCO^{GPS} can be estimated scale-independently. This method will fail if there is any systematic bias between independently estimated station coordinates for GPS and Galileo. Villiger (2019) reported translational biases of several mm when applying the L1 and L2 PVs of GPS to the Galileo E1 and E5 signals. The multi-signal ANTEX was released in 2019. With the signal-specific antenna corrections provided by Geo++ this systematic discrepancy should not occur anymore. This assumption was tested by processing GPS and Galileo solutions independently in the framework of the next IGS reprocessing campaign (repro3). However, due to the different satellite PCOs used (z-PCO^{GPS} from igs14.atx and z-PCO^{GAL} from GSA) a terrestrial scale bias of 1.16±0.27 ppb was observed in the GFZ submission that agrees well to the scale estimated between the solutions provided for example by CODE (1.10±0.21 ppb) or by ESA (1.09±0.18 ppb) (Männel et al., 2020). When taking this terrestrial scale into account, GPS and Galileo-based coordinates agree on the level of a few millimeters in the height component. The antenna coordinates are obviously the same, i.e., the terrestrial is the same, therefore the scale difference is simply introduced by the different PCOs. In a two-year (2017-2018) processing with this approach, (Villiger et al., 2020) derived −22.1 cm and −15.0 cm system-specific z-PCO^{GPS} with respect to the *igs14.atx* by fixing the Galileo PCOs to the chamber and robot calibrated values, respectively. The re-adjusted PCO^{GPS} by simply adding the mean difference from the 2017-2018 test have been updated in the IGS repro3 ANTEX file (igsR3_2077.atx) and will be used in the IGS repro3 processing.

5.3 Implementation of new datum definition in PANDA software

The geodetic datum in PANDA was defined by constraining the station coordinates with a priori uncertainties. To study the correlation between the z-PCO$^{\mathrm{GPS}}$ and the terrestrial scale, another datum definition is implemented by constraining the network translation, rotation, and scale between the a priori and the estimated station coordinates. Therefore no-net-translation (NNT), no-net-rotation (NNR), and no-net-scale (NNS) conditions can be applied to the ground network. In practice, replacing the datum definition is done at the normal equation (NEQ) level. During the regular processing, the coordinates of the ground stations are constrained by:

$$\boldsymbol{X} - \boldsymbol{X0} = \boldsymbol{U} \tag{5.4}$$

in which $\boldsymbol{X}$ is the estimated vectors of station coordinates, $\boldsymbol{X}0$ is the vector of a priori coordinates of the stations, and $\boldsymbol{U}$ is the a priori uncertainties. The normal equation of the last iteration of adjustment is saved for further applications. All the constraints in the normal equation can be modified in the re-solving or stacking processing. The a priori coordinate uncertainties are replaced by a free-network constraint as below (Thaller, 2008). Due to the assumption of small values for the Helmert transformation parameters between the a priori and estimated station coordinates, the transformation is linearized as:

$$\begin{bmatrix} x_i \\ y_i \\ zi \end{bmatrix} = \begin{bmatrix} x0_i \\ y0_i \\ z0_i \end{bmatrix} + \begin{bmatrix} 1 & 0 & 0 & 0 & -z0_i & y0_i & x0_i \\ 0 & 1 & 0 & z0_i & 0 & -x0_i & y0_i \\ 0 & 0 & 1 & -y0_i & x0_i & 0 & z0_i \end{bmatrix} \cdot \begin{bmatrix} T_x \\ T_y \\ T_z \\ \alpha \\ \beta \\ \gamma \\ \mu \end{bmatrix} \tag{5.5}$$

and written in matrix notation for station i as:

$$\boldsymbol{X_i} = \boldsymbol{X0_i} + \boldsymbol{B_i} \cdot \boldsymbol{\zeta} \tag{5.6}$$

where $\boldsymbol{\zeta}$ is the vector of Helmert parameters and $\boldsymbol{B_i}$ is the coefficient matrix for station i. The basic equation for solving for the Helmert parameters can then be written as

$$\begin{aligned} \boldsymbol{\Delta X} &= \boldsymbol{X} - \boldsymbol{X0}, \\ \boldsymbol{v} &= \boldsymbol{B} \cdot \boldsymbol{\zeta} - \boldsymbol{\Delta X} \end{aligned} \tag{5.7}$$

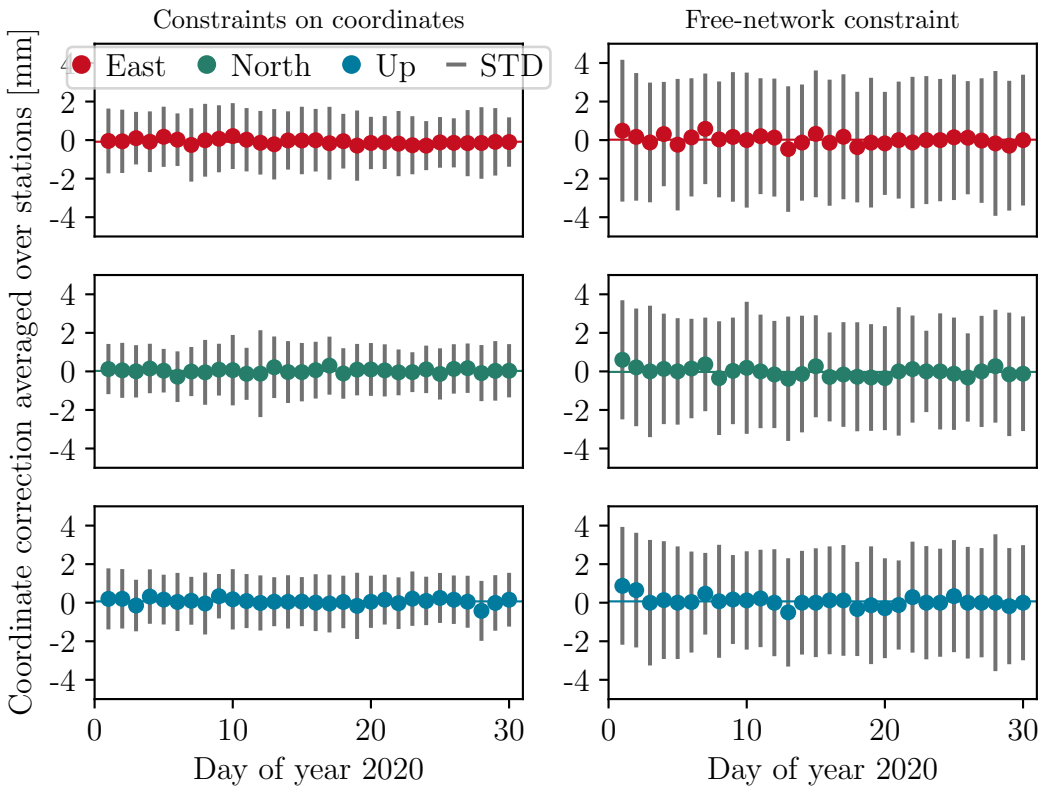

Figure 5.4: Corrections of station coordinates derived by applying direct constraints on the coordinates and no-net-conditions (no-net-rotation,-translation, and -scale) constraint. Different colors denote the East, North, and Up directions. The dots are the mean correction average over all stations. The gray bars denote the STD of the corrections over all the stations

with solution

$$\boldsymbol{\zeta} = (\boldsymbol{B}^{\boldsymbol{T}}\boldsymbol{B})^{-1}\boldsymbol{B}^{\boldsymbol{T}} \cdot \boldsymbol{\Delta X}. \tag{5.8}$$

The free-network constraint asks for zero values for the same or all transformation parameters (depending on requirement), i.e., $\boldsymbol{\zeta} = \mathbf{0}$. Therefore, the Jacobian matrix is $\boldsymbol{H} = (\boldsymbol{B}^{\boldsymbol{T}}\boldsymbol{B})^{-1}\boldsymbol{B}^{\boldsymbol{T}}$. Finally, the system of normal equations including free-network constrains read as:

$$\left(\boldsymbol{A}^{\boldsymbol{T}}\boldsymbol{P}\boldsymbol{A} + \boldsymbol{H}^{\boldsymbol{T}}\boldsymbol{P}_h\boldsymbol{H}\right) \cdot x = \boldsymbol{A}^{\boldsymbol{T}}\boldsymbol{P}\boldsymbol{l} \tag{5.9}$$

where $\boldsymbol{A}$ is the design matrix, $\boldsymbol{P_h}$ is the weight matrix for transformation parameters. In our re-solving of the normal equation, the initial constraints based on Equation 5.4 is abandoned and the free-network constraint is applied by setting different weight matrices $\boldsymbol{P}_h$.

To show the differences between the constraint on coordinates and the no-net-conditions constraint, i.e., no-net-rotation, -translation, and -scale, the NEQ of the GPS POD processing is discussed in Section 3.1 is resolved by replacing the constraint on

Table 5.1: Transformation parameters between the a priori and the estimated coordinates of ground stations by applying two types of constraints. The mean value is averaged the 30 days' solutions. The STD is relative to the mean

Transformations	coordinate constraints mean/STD	no-net-conditions constraint mean/STD
x-translation [m]	$-8.1\times10^{-5}\pm\ 1.3\times10^{-4}$	$-5.6\times10^{-12}\pm\ 3.6\times10^{-12}$
y-translation [m]	$4.8\times10^{-5}\pm\ 1.5\times10^{-4}$	$6.1\times10^{-13}\pm\ 3.0\times10^{-12}$
z-translation [m]	$5.3\times10^{-5}\pm\ 1.5\times10^{-4}$	$-1.7\times10^{-12}\pm\ 2.3\times10^{-12}$
scale [ppb]	$6.6\times10^{-3}\pm\ 3.5\times10^{-2}$	$-3.4\times10^{-11}\pm\ 8.3\times10^{-11}$
x-rotation [arcsec]	$-2.7\times10^{-12}\pm\ 1.9\times10^{-11}$	$-4.2\times10^{-18}\pm\ 7.3\times10^{-18}$
y-rotation [arcsec]	$5.7\times10^{-12}\pm\ 2.3\times10^{-11}$	$-3.5\times10^{-19}\pm\ 1.3\times10^{-17}$
z-rotation [arcsec]	$1.0\times10^{-11}\pm\ 2.0\times10^{-11}$	$-4.2\times10^{-19}\pm\ 3.9\times10^{-19}$

the coordinates with the no-net-conditions constraint. In the initial processing, all the coordinates are constrained by uncertainties in millimeter level because they are taken from the final IGS SINEX products with precise positions and velocities. Consequently, very strong constraints to the translations, rotations, and scale are applied to the whole network in the resolving of NEQ. It should be mentioned that NNS constraint is not applied for GNSS in normal cases except for the estimation of PCOs. The comparison focus on the corrections of the station coordinates and the transformation between the a priori and the estimated coordinates. Figure 5.4 show the correction of the coordinates by applying the two different constraints in 30 days. Because of the strong constraints, the mean corrections averaged over the stations in both solutions are close to zero. There is no obvious difference among the three components. The RMS of the coordinate corrections over all stations is the obvious difference between the two solutions. The solution derived by applying the direct constraints on the coordinates has smaller (1 to 2 mm) RMS than the no-net-conditions constraint solution (3 to 4 mm). The direct constraint on the coordinates has a stronger effect on the individual coordinates than the no-net-conditions constrain. However, the no-net-conditions constraint with this performance is sufficient for the studies in the next sections. The network transformations present the advantage of the no-net-conditions constraint. The Helmert-transformation parameters between the a priori and the estimated coordinates of the two solutions are listed in Table 5.1. The mean values are averaged over 30 days and the STD is relative to the mean. Due to the strong constraints again, the ground network in both solutions has very slight transformations. However, the no-net-conditions constraint solution is much stronger. The no-net-conditions constraint avoids the deformation of the network efficiently. The strong advantage of the no-net-conditions is that stations can show variations, for example with respect to loading deformations, without being absorbed by the residuals or clock corrections.

5.4 Study of determining PCO^{GPS} by including LEOs

Regarding the problems in the estimation of PCO^{GPS} mentioned in Section 5.1 and the benefits of adding LEOs to the processing discussed in Section 5.2.1, various experiments are performed in different scenarios to investigate the impact of adding LEOs on the PCO^{GPS} estimation in this section. The seven LEOs which have been introduced in section 2.3 and used already in the POD study (section 4.3) are integrated into this study. In section 5.4.1, the ground- and space-based data description and the selected ground network are introduced. Then, the processing and analysis strategies are introduced in section 5.4.2. Section 5.4.3 mainly discusses the estimated x/y-PCO^{GPS}. Section 5.4.4 focuses on the z-PCO^{GPS} estimated and the determined scale. In section 5.4.5, the impact of individual LEOs on the estimation of z-PCO^{GPS} is investigated based on cases with different subsets of the LEOs.

5.4.1 Data status of LEOs and ground stations

The data availability of the seven LEOs is shown in Figure 5.5. In total, data from 251 days in 2016 are processed. In the gaps, the corresponding LEOs are excluded for different reasons, including missing data, bad data quality, and orbit maneuvering. There are 192 days in which all seven LEOs are available, and at least four LEOs are available in the remaining 59 days. The processing period starts on the 115th day of the year (DOY 115) 2016 because the quaternions data of Jason-3 are available from that day onward. GPS satellites had no SVN-PRN change during our processing period except for PRN G04 which was excluded completely due to its unstable data quality (see discussion in Section 4.3.1). Therefore, all results are referred to PRN numbers in this paper (see SVN-PRN matching in the Appendix). To avoid residual systematic errors, the processing period for a reliable and consistent estimation of PCO^{GPS} , especially in x- and y- directions, should be as long as possible (Schmid et al., 2007). This short period study is on purpose to test and develop the method. Moreover, the processing period is also limited by the seven LEOs. However, as a proof of concept, the derived PCO^{GPS} in this study shows the benefits of including LEOs. More focus is placed on comparison and cross-check to the Galileo-based method later on. A proper PCO^{GPS} product will be provided after extending the period significantly. A long-term solution will be given within the upcoming InGE project mentioned before.

A global GPS ground tracking network with a total of 54 well-distributed IGS stations is selected as the main processing network (cf. Figure 5.6, blue dots). The PCO^{GPS} in three directions are estimated by integrating the seven LEOs with this network.

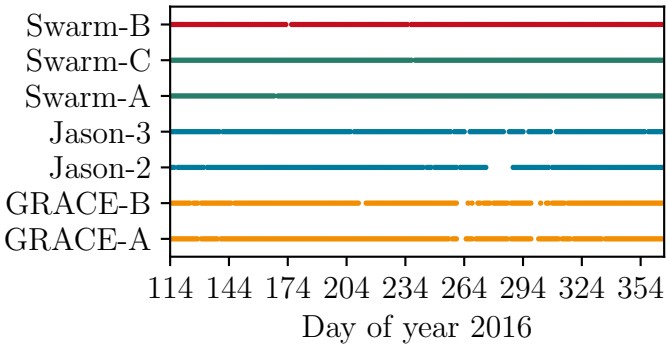

Figure 5.5: Status of LEOs data availability in the processing period (251 days in total)

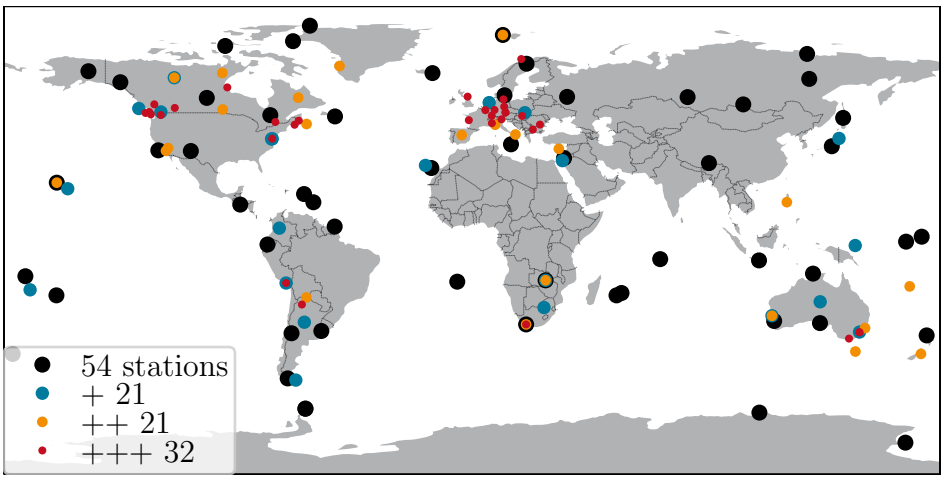

Figure 5.6: Selected ground tracking networks with different density. 54-stations (blue) in global distribution are selected as main processing network. 21 (green), 21 (orange) and 32 (red) stations are added to the network step-by-step to generate three more dense networks

Additionally, three more and more dense networks are selected by adding iteratively 21 (green), 21 (yellow), and 32 (red) stations step-by-step. All the stations mentioned above are available during the 251 days, and their accurate coordinates are always available in IGS SINEX under IGb08 reference frame (Rebischung et al., 2012) that is aligned to ITRF2008 (Altamimi et al., 2011) that was used by the IGS operation in 2016. Due to this station selecting criterion, the additional stations are less uniformly distributed, especially for the red stations added in the last step. The four different networks offer different numbers of observations and geometry to the processing, and the network geometry diversity is typically important to the discussion about the correlation between the GPS z-PCO and the scale in Section 5.1. The impact on PCO estimation of adding ground stations and integrating LEOs are discussed in Section 5.4.1 and 5.4.2.

5.4.2 Processing and analysis strategy

The processing strategy applied here is similar to the integrated POD study in Section 4.3. It is a 'one-step' processing of estimating GPS and LEOs orbits and other parameters simultaneously. Besides, instead of using the PCO^{GPS} from *IGS08.atx* (Schmid et al., 2016) as a priori known values, the daily satellite-specific PCOs for GPS are freely estimated without constraints, i.e., no a priori information on the PCOs are introduced. Although the general configuration for the processing in this study is given in Table 2.5, more detailed information for this study about PCO is listed in Table 5.2. The orbit modeling has been introduced already in Section 2.5.2.

It has to be mentioned that the used PCO$_{LEO}$ are taken from different sources. For GRACE-A/B satellites, their PCOs are given by Montenbruck et al. (2009) which are according to Wübbena et al. (2000) pre-launch calibrated by a robot. The PCOs of OSTM/Jason-2 and Jason-3 are taken from Bertiger et al. (2010) and Couderc (2015), respectively. The GPS antennas of these two satellites are identical and their PCOs were measured on the ground (Couderc, 2015). The PCOs of Swarm-A/B/C satellites which are characterized in a test chamber are offered by Siemes (2019). Their sources are listed in Table 5.2. The PVs of LEOs are also important to this study. They are normally estimated by previous studies. For example, Montenbruck et al. (2018) reported in-flight calibrated PVs for the Swarm satellites of up to 25 mm. However, the in-flight calibration are not independent of the scale provided by VLBI and SLR. Therefore, the PVs of LEOs are not applied or estimated in this study. Consequently, there are potential errors in

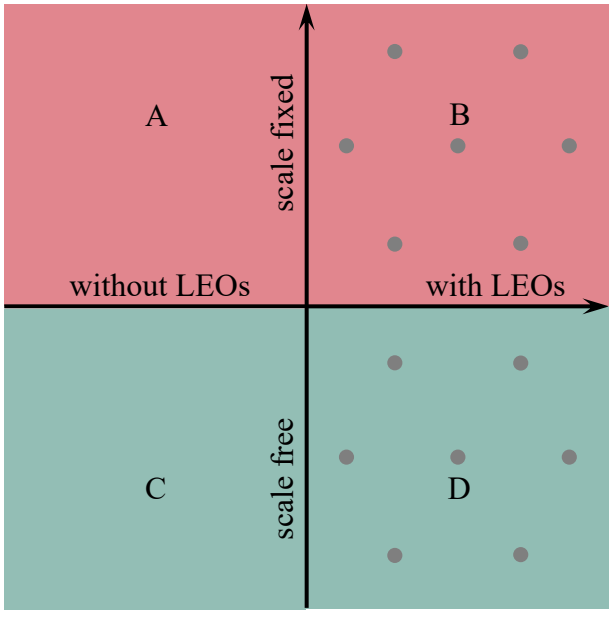

Figure 5.7: Four types of processing for PCO^{GPS} estimation. The gray dots denote the seven integrated LEOs

Table 5.2: Processing configurations and estimated parameters for z-PCO^{GPS} estimation

Configurations	
Arc length	24 hours
Cut-off elevation	7° for ground stations and 3° for LEOs
Observations	zero-difference ionosphere-free phase and code measurements; 5 minutes sample rate for both ground and on-board observations
Weighting	ground and space-based observations are equally weighted
LEOs attitude	antenna position and star camera based spacecraft attitude (quaternions data provided by operators)
LEOs receiver PCO	GRACE-A/B taken from Montenbruck et al. (2009); OSTM/Jason-2 taken from Bertiger et al. (2010)) Jason-3 offered by Couderc (2015); Swarm-A/B/C offered by Siemes (2019)
LEOs receiver PV	not applied
Station receiver PCO/PV	*IGS08_1930.atx* (Schmid et al., 2016)
Ambiguity fixing	only within ground stations
GPS PV	*IGS08_1930.atx*
Parameters	
PCO^{GPS}	satellite-specific daily solution of L1/L2 ionosphere-free combined PCO in three directions; freely estimated without constraints
Station coordinate	no-net-translation and no-net-rotation with respect to IGb08 reference frame that aligns to ITRF2008 (Altamimi et al., 2011), scale is constrained depending on the scenarios
GPS orbit	initial epoch state vector and five solar radiation pressure parameters; initial orbital elements are generated from broadcast ephemeris
LEOs orbit	initial epoch state vector; piece-wise empirical force (90 minutes interval) and atmosphere drag (four hours interval) parameters; initial orbital elements are generated from official orbit products
Earth rotation	rotation pole coordinates and UT1 for 24h intervals, piece-wise linear modeling
Tropospheric delay	for each ground station; piece-wise constant zenith delays for 1h intervals; piece-wise constant horizontal gradients for 4h intervals
Clock offsets	satellites and receivers; epoch-wise; pre-eliminated

the LEOs' receiver phase center positions. The impact of the errors in z-PCO$_{LEO}$ on the estimation of z-PCO^{GPS} is discussed in Section 5.4.5.

To study the impact of adding LEOs and the effect on the correlation between the z-PCO^{GPS} and the scale, depending on LEOs and the constraint on the scale, four types of processing are performed. The four groups are shown in Figure 5.7 as A, B, C, and D. Scale fixed means that the NNS constraint is applied to the ground station network as the description in Section 5.3. Type A doesn't include LEOs and constrains the terrestrial scale by applying the NNS condition. Additionally, type A is also the IGS standard processing since 2016. In type B, the gravitational constraint due to the dynamics of LEO orbits and the NNS constraint work together on the terrestrial scale. Therefore, the inconsistency between the two constraints may be shown in this over-constrained solution. Type C has neither constraint on the scale nor additional observations from LEOs. In type D, different from type B, only the gravitational constraint from LEOs is applied. The PCO^{GPS} in three components are always estimated jointly in all cases. However, due to the different characteristics of the horizontal and vertical PCOs, they are analyzed separately in Sections 5.4.3 and 5.4.4. According to the results, the estimated horizontal PCOs are nearly identical between the solutions with and without applying NNS. That means the NNS condition does not visibly affect the estimation of horizontal PCOs. This is also expected from theory. Therefore, the solutions with NNS constraint are simply used to analyze the horizontal PCOs, i.e., the solutions in type A and B. The estimated offsets in x- and y-directions are analyzed based on the formal error and the STD to the mean of the time series. Especially, their correlation with the solar elevation angle (β angle) is discussed in detail. The comparison is mainly between the GPS-only solution derived by the 54-station network and the solution derived by adding seven LEOs. For the estimation of z-PCO^{GPS} , 16 scenarios in the four processing types solutions are presented in Section 5.4.4. The ground network is an additional difference between the 16 scenarios. The discussion is mainly about the correlation between the z-PCO^{GPS} and the scale. In the processing without applying NNS constraint, the correlation matrix ($Q_{x,zpco}$) between the estimated coordinates of all stations (vector x) and the z-PCO^{GPS} of all GPS satellites can be derived from the variance-covariance matrix. Based on the linearized Helmert-Transformation equations between the estimated and the a priori coordinates of all ground stations, the vector (h) of the seven transformation parameters can be expressed by

$$\underset{7\times1}{h} = \underset{7\times3n}{B} \cdot \underset{3n\times1}{x} \tag{5.10}$$

in which n is the number of ground stations and B is the matrix expressing least-squares fit. Therefore, the correlation matrix ($Q_{h,zpco]}$) between h and z-PCO^{GPS} can be derived

by

$$\underset{(7+m)\times(7+m)}{Q_{h,pcoz}} = \begin{bmatrix} \underset{7\times 3n}{B} & \underset{7\times m}{0} \\ \underset{m\times 3n}{0} & \underset{m\times m}{I} \end{bmatrix} \underset{(3n+m)\times(3n+m)}{Q_{x,zpco}} \begin{bmatrix} B & 0 \\ 0 & I \end{bmatrix}^T \tag{5.11}$$

in which m is the number of GPS satellites and I is the identity matrix.

In Section 5.4.5, in addition to the z-PCO$^{\mathrm{GPS}}$ analysis, 17 different scenarios are performed in type D, i.e., with different subsets of LEOs and scale-free condition, to study the impact of the errors in z-PCO and other aspects of the LEOs on the estimation of scale-independent z-PCO$^{\mathrm{GPS}}$.

5.4.3 Improvement of the estimation of x- and y-PCO$^{\mathrm{GPS}}$

As mentioned in Section 5.1 the precision of the horizontal PCO components depends on the β angle. The GPS satellites are flying in six different orbital planes (cf. Table 5.3). The six orbital planes are sorted by their maximum β angles. For the satellites in the same orbital plane, the change of the β angle is identical. In Table 5.3, the orbital planes are arranged in descending order of the maximum β angle during our processing period. The blue lines in Figure 5.8 show the β angles of selected satellites in different orbital planes. Simultaneously, the formal errors of the daily estimated offsets in x- and y-directions are presented in this figure. The red dots denote the results from the scenario which includes only 54 ground stations, and the green dots are presenting the scenario which in addition includes seven LEOs. Seen from the upper three plots, the formal errors increase obviously when the β angle is getting larger because the satellite rotation rate gets slower for large β angle, subsequently, the correlation between orbit and PCO is hardly resolvable during this periods. In the lower three plots, the maximum β angles are smaller than 50°, the formal errors are correspondingly very stable with small values. Comparing between x- and y-direction offsets, the formal error in the large β angle period increases more significantly in y-direction than in x-direction. For instance, in the ground-only solution of satellite G03 (orbital plane F), the maximum formal error is around 16 cm in the x-direction, while that of the y-direction is about 40 cm. Schmid et al. (2007) give an explanation from the geometrical point of view. The y-PCO is stronger correlated with the orbital parameters since the y-axis keeps close to the along-track direction, while the x-axis is nearly perpendicular to the along-track direction. After adding LEOs to the processing, the large formal errors in the large β angle period decrease obviously. For example, the formal error peaks of G03 x- and y-PCO are reduced from about 17 cm and 45 cm to 9 cm, and 25 cm, respectively. When the β angle is small, the impact of adding LEOs is not very obvious.

Figure 5.9 shows the β angle based distribution of the formal errors of all the satellites from daily solutions. The relationship between a large β angle and the improvement by

Table 5.3: Classification of PRN-specific satellites based on the orbital planes. The third column is the maximum absolute orbital β angle of the corresponding orbital plane in the 251 processing days.

Orbital plane	**PRN**	$\lvert\beta\rvert_{max}$ [°]
F	G03, G05, G10, G18, G20, G22	78.3
E	G09, G13, G14, G15, G23, G32	70.5
A	G01, G02, G06, G21	65.8
D	G07, G11, G24, G30, G31	49.7
B	G08, G17, G19, G27, G29	43.4
C	G12, G16, G25, G26, G28	33.3

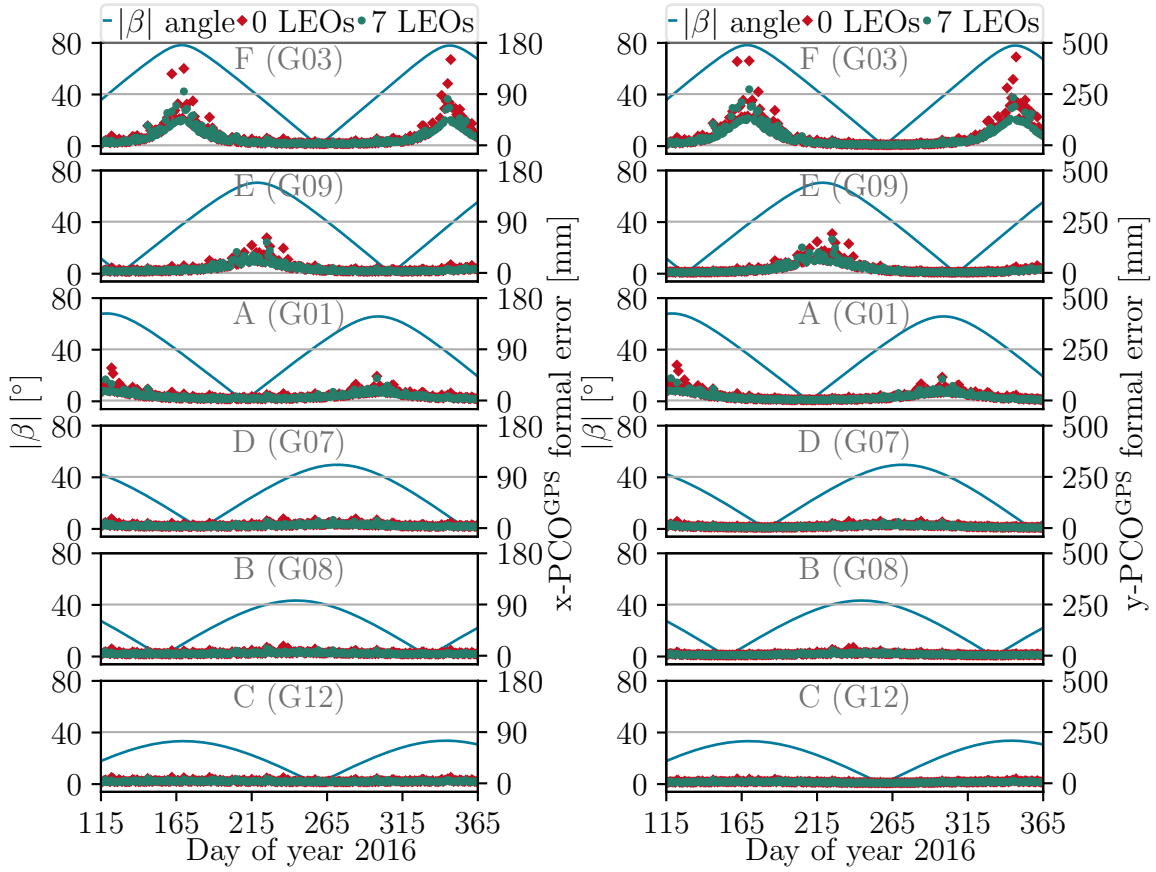

Figure 5.8: Time series of x-PCO^{GPS} (left) and y-PCO^{GPS} (right) formal errors. Six example satellites from different orbital planes. β angles are shown in absolute values

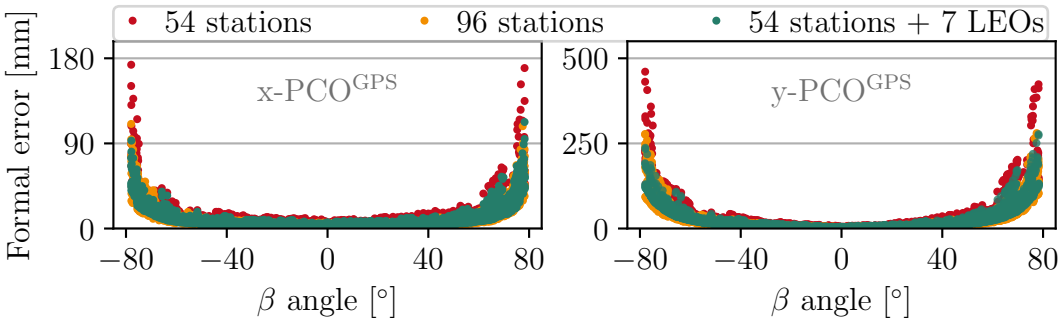

Figure 5.9: Distribution of x-PCO$^{\mathrm{GPS}}$ (left) and y-PCO$^{\mathrm{GPS}}$ (right) formal errors with respect to β angle

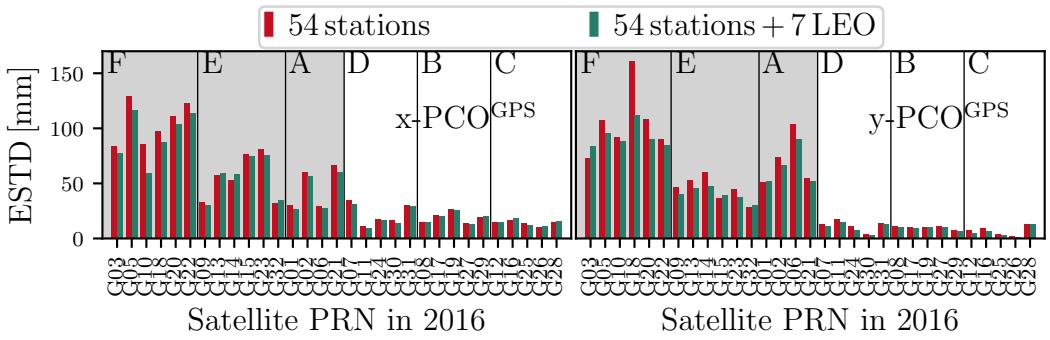

Figure 5.10: Empirical standard deviations (ESTD) of x-PCO$^{\mathrm{GPS}}$ (left) and y-PCO$^{\mathrm{GPS}}$ (right) with respect to the mean of the time series in 251-day solutions. The results are sorted by the orbital planes (from large to small β angles)

integrating LEOs is clearly shown in the left plot. The average reductions of formal errors for β angles larger than 70° are 14% and 17.7% for x-PCO and y-PCO, respectively. On the right of Figure 5.9, the orange dots denote the formal error derived in the scenario which includes 96 ground stations only. The improvement due to the additional seven LEOs and due to the additional 42 ground stations is very similar. Additionally, the formal-error-based weight means of the x- and y-PCO$^{\mathrm{GPS}}$ values derived by the seven LEOs integrated processing is given in the table in the appendix.

The STD of x-PCO$^{\mathrm{GPS}}$ and y-PCO$^{\mathrm{GPS}}$ of each satellite from the 251-day processing is shown in Figure 5.10. In each plot, the results are sorted by the orbital planes. The satellites in orbital planes F, E, and A (with large maximum β) have significantly larger STD than the other satellites in orbital planes D, B, and C (with small maximum β). For 12 of the 16 satellites in orbital planes F, E, and A, the STD of x-PCO$^{\mathrm{GPS}}$ and y-PCO$^{\mathrm{GPS}}$ become smaller after adding LEOs to the processing. Several of them are significant, for example, the x-PCO of G10 (2.6 cm reduction) and the y-PCO of G18 (4.5 cm reduction). The STD of the four satellites gets slightly bigger (less than 3 mm) after adding LEOs. This phenomenon might be caused by different aspects, for example, the processing period

Table 5.4: Results of 16 scenarios for z-PCO^{GPS} estimation in 251 days. NNT and NNR conditions are always applied. The introduction about groups A, B, C, and D are given in Section 5.4.2 via Figure 5.7. ΔScale is the scale between the estimated and the a priori coordinates (in IGb08) averaged over 251 days. z-ΔPCO^{GPS} is the difference between the estimated z-PCO^{GPS} and *igs08_1930.atx* averaged over satellites and days. The correlation coefficient is between z-ΔPCO^{GPS} and the scale averaged over satellites and days

Group	Scenarios	Stations	LEOs	Constraint	Correlation coefficient	ΔScale [ppb] mean/STD	z-ΔPCO [mm] mean/STD
A	a1	54	0	NNS NNR NNT	0	0	−4.7±42.1
	a2	75			0	0	+2.2±30.7
	a3	96			0	0	−4.2±29.6
	a4	128			0	0	−3.8±28.4
B	b1	54	7	NNS NNR NNT	0	0	−99.6±26.12
	b2	75			0	0	−76.3±26.0
	b3	96			0	0	−72.3±55.6
	b4	128			0	0	−62.3±47.3
C	c1	54	0	scale-free NNR NNT	0.85	−1.77±0.88	+234.9±105.0
	c2	75			0.85	−0.24±1.16	+37.6±146.5
	c3	96			0.86	+0.81±1.02	−99.7±126.7
	c4	128			0.84	+0.42±0.87	−55.1±101.0
D	d1	54	7	scale-free NNR NNT	0.30	+1.80±0.43	−254.8±56.7
	d2	75			0.36	+1.91±0.43	−258.1±55.1
	d3	96			0.40	+1.90±0.61	−262.7±53.7
	d4	128			0.43	+1.86±0.53	−255.2±52.3

or the LEOs' geometry.

5.4.4 GPS z-PCO and GPS-based scale determined by including LEOs

Regarding the correlation between the z-PCO^{GPS} and the scale (Zhu et al., 2003), the satellite-specific z-PCO^{GPS} are estimated in 16 scenarios (cf. Table 5.4). NNT and NNR conditions compared to the IGb08 reference frame are applied to all scenarios. The 16 scenarios are classified into four groups (A, B, C, and D) based on the four types of processing discussed in Section 5.4.2 and shown in Figure 5.7. In each group, there are four scenarios that have different numbers of ground stations. Groups A and C include ground-based only scenarios, while the scenarios in groups B and D are integrated with seven LEOs. In groups A and B, the ground network scale is constrained to the IGb08 scale, while the NNS condition is not applied in group C and D. According to the statistics of the results, the correlation coefficient between the scale and the z-PCO^{GPS} varies slightly between different satellites and during the processing days (two magnitudes smaller than

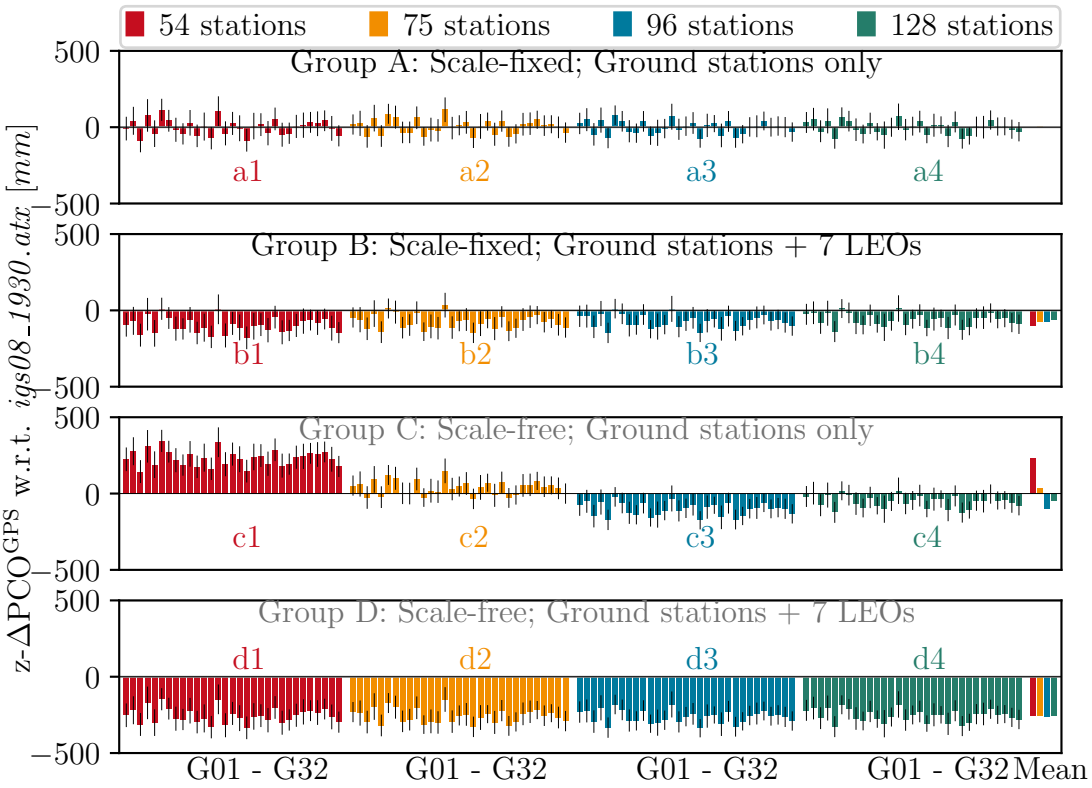

Figure 5.11: Satellite-specific z-PCO$^{\mathrm{GPS}}$ differences compared to the z-PCO$^{\mathrm{GPS}}$ in *IGS08_1930.atx* derived by the 16 scenarios in Table 5.4. The colored bars present the PCO-z corrections. The error bars presents the standard deviations (STD) of the PCO-z corrections with respect to the mean values of the time series in 251-day solutions.

the values themselves), therefore the values presented in Table 5.4 are averaged over all satellites and processing days. The STD values of the time series relative to the means are listed to show the stability. ΔScale is the change of the ground network scale compared to the a priori coordinates in ppb. z-ΔPCO$^{\mathrm{GPS}}$ is the differences between the estimated values and the values from *IGS08_1930.atx* averaged over all satellites.

Besides the statistical and system-specific results shown in Table 5.4, the satellite-specific z-ΔPCO$^{\mathrm{GPS}}$ of the 16 scenarios are presented by colored bars in Figure 5.11. Red, orange, blue, and green denote the results derived from the scenarios with 54, 75, 96, and 128 ground stations. At the right end of each plot, the z-ΔPCO$^{\mathrm{GPS}}$ averaged over all satellites are shown (also see statistical results in Table 5.4). It has to be mentioned that the z-PCO$^{\mathrm{GPS}}$ values in this discussion are formal-error-based weighted mean over 251 days. In groups A and B, due to the scale constraint, the correlation and ΔScale are all zeros. The estimated z-PCO$^{\mathrm{GPS}}$ values of the four ground-based only scenarios in group A agree with *IGS08_1930.atx* very well with only 2 mm to 4 mm differences in average. The z-PCO$^{\mathrm{GPS}}$ values derived by the four scenarios including seven LEOs (group B) have −6 cm to −10 cm collective shifting with respect to *IGS08_1930.atx*. It

shows the inconsistency between the constraints from the terrestrial network and from the LEOs. With more ground stations used, the z-ΔPCO^{GPS} value is reduced due to the stronger network constraint. In groups C and D, the constraint on the network scale is removed. Consequently, the four ground-based only scenarios (group C) derived very high correlation coefficients between the z-PCO^{GPS} and the scale (about 0.85), and adding more ground stations cannot dissolve this problem. Correspondingly, the estimated z-PCO^{GPS} values are very different from scenario c1 to c4 due to different ground network densities and geometry. The ΔScale values vary from -1.77 ppb to $+0.81$ ppb (-11 mm to $+5$ mm at the equator), and the z-ΔPCO^{GPS} values vary collectively from -99.7 mm to $+234.9$ mm. After adding seven LEOs (group D), the correlation coefficients are reduced significantly to 0.3$\sim$0.42. The correlation and STD increases from scenario d1 to d4 as more ground stations are used, because the increased proportion of ground-based observations weakens the de-correlation effect by adding seven LEOs. Due to the effective de-correlation, ΔScale and z-ΔPCO^{GPS} are quite stable in group D with about 0.1 ppb (0.6 mm at the equator) and 1 cm variations, respectively. The z-ΔPCO^{GPS} derived in group D is -25.5 cm on average. Based on the ground calibrated Galileo transmitter and receiver offsets, Rebischung (2019) estimated the z-PCO^{GPS} by Galileo scale and reported a -16 ± 2.5 cm correction of the z-PCO^{GPS} compared to *igs14.atx*. Villiger et al. (2020) derived -22.1 cm and -15.0 cm system-specific z-PCO^{GPS} with respect to the *igs14.atx* for by fixing the Galileo PCOs to the chamber and robot calibrated values, respectively. Taking the -6cm difference between *igs08.atx* and *igs14.atx* (Rebischung and Schmid, 2016) into account, both solutions differ by only 3.1 cm. The satellite-specific z-PCO^{GPS} differences between scenario d1 and Rebischung (2019) solution, as well as the official *igs08.atx*, are listed in the table in the Appendix. The detailed comparison and cross-check between the two methods based on LEOs and Galileo are presented in Section 5.5.

The STD of the estimated z-PCO^{GPS} with respect to the mean of the time series are shown as error bars in Figure 5.11. The STD values in group A are reduced by adding more ground stations. However, due to the inconsistency between the two constraints, the STD values in group B have no obvious trend relative to the number of stations. After removing the constraint on the network scale, the STD derived by the ground-based only scenarios (group C) increase significantly by five to ten centimeters larger than that of group A. However, there is no visible trend of STD due to the additional stations. Especially for scenario c2 and c3, the STD of them is even larger than that of scenario c1 which includes fewer stations. This shows the instability of the estimations in group C. In group D, the STD values vary from 52 mm to 58 mm with a trend of very slight decreasing due to additional stations (one to two millimeters with 20 more stations). Therefore, adding LEOs makes the estimation stable with different scale constraints and

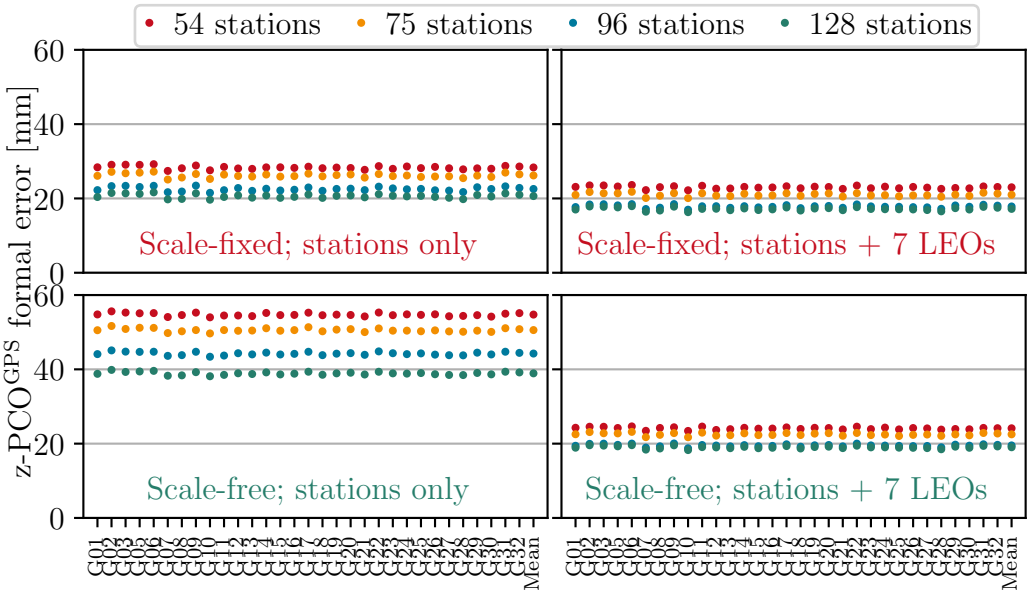

Figure 5.12: Formal errors of satellite-specific z-PCO$^{\mathrm{GPS}}$ averaged over 251 days of the 16 scenarios in Table 5.4

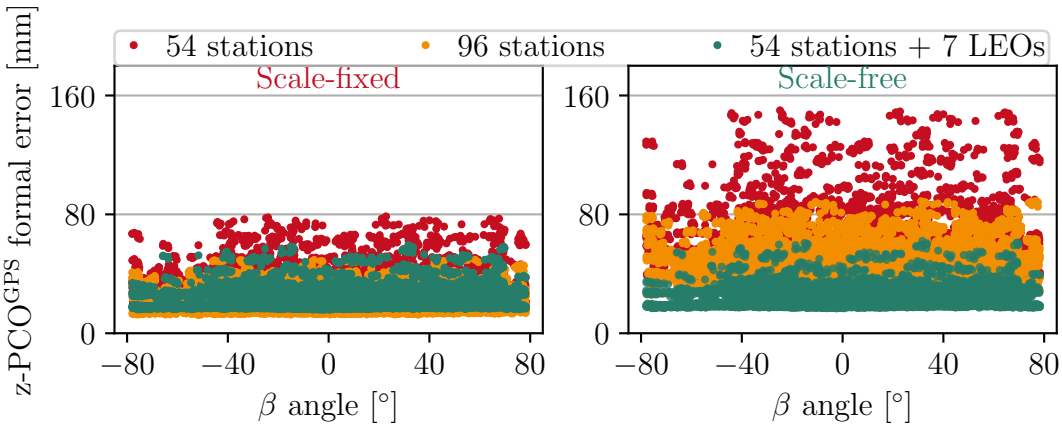

Figure 5.13: Distribution of z-PCO$^{\mathrm{GPS}}$ formal errors with respect to β angle

network geometry.

Figure 5.12 presents the satellite-specific formal errors of z-PCO^{GPS} averaged over 251 processing days of the 16 scenarios. In each plot, the formal errors of z-PCO^{GPS} are reduced for all satellites when more ground stations are used. That means the precision of estimated z-PCO^{GPS} can be improved by using more ground stations. In the two upper plots (groups A and B), the formal errors are smaller than 30 mm in all scenarios due to the scale constraints. However, the LEOs integrated scenarios in group B (*upper right*) have 3 to 6 mm smaller formal errors than the ground-based only scenarios in group A (*upper left*) due to the additional observations and geometry from LEOs. After removing the constraints on the network scale, the z-PCO^{GPS} formal errors of the ground-based only scenarios in group C (*lower left*) increased significantly compared to that of group A. The averaged formal error differences between a1∼a4 and c1∼c4 are 26 mm, 24 mm, 22 mm and 22 mm, respectively. This is caused by the correlation between the GPS z-PCO^{GPS} and the terrestrial scale. Due to the de-correlation effect by integrating LEOs, the formal errors derived by LEOs integrated scenarios in group D (*lower right*) nearly remain the same (1 to 2 mm larger) as group B. In a short summary, the GPS z-PCO^{GPS} can be estimated precisely when either a NNS condition is applied or LEOs with dynamic POD are integrated into the processing. The NNS condition offers the network constraint while the orbit dynamics of orbits introduce the gravitational constraint. Additionally, similar to Figure 5.9, the distribution of the formal errors of z-PCO^{GPS} with respect to the β angles is presented in Figure 5.13 for scenarios a1, a3, b1, c1, c3, and d1. However, no correlation between the β and z-PCO^{GPS} is visible in the plots. The Pearson correlation coefficients between the formal errors of the z-PCO^{GPS} and the β angles for the six scenarios are all below 0.1.

5.4.5 Impact of individual LEOs on the GPS z-PCO estimation

We performed 17 scenarios for the z-PCO^{GPS} estimation under NNT, NNR, and scale-free conditions, in order to investigate the impact of individual LEOs on the z-PCO^{GPS} estimation. Different numbers and combinations of LEOs are integrated into different scenarios. DOY 176 to DOY 200 (25 days) are selected as a processing period because all seven LEOs are fully available during this period. The results are shown in Table 5.5. The scenarios marked by asterisks ($*$) are additional experiments where a +3 cm artificial bias is added to Swarm-A/B/C z-PCO. Based on these scenarios, the impact of the z-PCO$_{LEO}$ accuracy is shown in this section.

Seen from the scenarios without the asterisk, the correlation between the scale and the z-PCO^{GPS} decreases by adding more LEOs (from 0.85 to 0.3). Comparing the scenarios

Table 5.5: Different scenarios of LEOs integrated processing in 25 days. NNT, NNR and scale-free conditions are always applied. 54 ground stations are used in all scenarios. Cross mark (×) means the corresponding LEO satellite is integrated. Asterisk (∗) means the satellite is added +3 cm artificial bias in z-PCO_{LEO}. Correlation is the correlation coefficient between z-PCO^{GPS} and the scale average over satellite and days. ΔScale is the scale between the estimated and the a priori coordinates (in IGb08) averaged over 251 days. z-ΔPCO^{GPS} is the difference between the estimated z-PCO^{GPS} and *igs08_1930.atx* (averaged over satellites and days).

Scenarios	G-A	G-B	J-2	J-3	S-A	S-B	S-C	LEOs Obs.	Correlation coefficients	ΔScale [ppb]	z-ΔPCO^{GPS} [mm]
0	54 ground stations without LEOs							0	0.85	−1.57	+233
1	×							2300	0.60	+1.22	−161
2		×						2000	0.65	+0.57	−73
3			×					1859	0.63	+0.67	−86
4				×				2436	0.55	+1.45	−193
5					×			2059	0.63	+1.11	−145
5*					×*				0.63	+5.46	−736
6						×		2092	0.62	+1.33	−179
6*						×*			0.62	+5.67	−769
7							×	2069	0.63	+0.96	−123
7*							×*		0.63	+5.33	−718
8	×	×						4300	0.52	+1.30	−173
9			×	×				4296	0.48	+1.43	−190
10	×		×					4159	0.51	+1.33	−176
11					×	×	×	6220	0.44	+1.67	−221
11*					×*	×*	×*		0.44	+6.76	−918
12	×	×	×					4359	0.46	+1.36	−181
13	×		×		×			6218	0.44	+1.53	−205
13*	×		×		×*				0.43	+3.24	−436
14	×	×	×	×				8595	0.38	+1.69	−214
15		×	×		×	×		8010	0.40	+1.58	−211
15*		×	×		×*	×*			0.40	+4.39	−594
16	×			×	×	×		8887	0.36	+1.87	−251
16*	×			×	×*	×*			0.36	+4.16	−564
17	×	×	×	×	×	×	×	14815	0.30	+1.77	−237
17*	×	×	×	×	×*	×*	×*		0.30	+4.00	−540

with only one LEO satellite, the impact of the number of space-based observations on the de-correlation is obvious. For example, GRACE-A has on average 300 more observations per day than GRACE-B, correspondingly the correlation coefficient is 0.05 smaller for the GRACE-A solution (scenario 1 against 2). A similar phenomenon can be observed for the comparison between scenarios 3 and 4. There is a 0.08 difference of correlation coefficient where Jason-3 has 577 more observations than OSTM/Jason-2. The different numbers of observations of these two pairs can be explained by satellites getting older and more unstable (GRACE-A/B and OSTM/Jason-2). Both examples have spacecraft flying in close formation on the same orbit. That means the satellites have the same orbital characteristic and the same observation geometry. Therefore, the de-correlation differences could be related only to the number of observations. In addition, scenarios 15 and 16 both have four LEOs in four orbital planes, but the 878 more observations of scenario 16 lead to a smaller correlation coefficient. This also supports the conclusion mentioned above. The three satellites of the Swarm mission have a similar amount of observations and correlation coefficients (scenarios 5, 6, and 7). The impact of the LEOs orbital plane diversity can not be seen from the results, and this is different from the conclusion of the LEOs integrated POD study by Huang et al. (2020). The reason is that the number of space-based observations is more important than the geometry of the observations for propagating gravitational constraint of the LEOs to the GPS satellites. Moreover, the de-correlation due to the extended nadir angles of observations can be realized by comparing scenarios 8 with 9. The total numbers of LEOs observations in these two scenarios are similar, while 0.04 smaller correlation is derived in scenario 9. This can be explained by the larger nadir angles of observations obtained by OSTM/Jason-2 and Jason-3 due to their higher altitude compared to GRACE-A and GRACE-B satellites.

The derived scale with respect to IGb08 (ΔScale in Table 5.5) and the z-PCO^{GPS} corrections with respect to *igs08_1930.atx* (z-ΔPCO^{GPS} in Table 5.5) vary between the scenarios. The accuracy of these estimated parameters is affected, for example, by the LEOs dynamic modeling, the observations quality, and the accuracy of the a priori z-PCO$_{LEO}$ values which are fixed in the estimation. The orbit modeling for all the LEOs in this study is identical and introduced in Section 2.5.2. The observations quality and the PCO$_{LEO}$ corrections depend on the LEOs aging. For instance, GRACE-A/B and OSTM/Jason-2 satellites are at the end of their service life during our processing period, therefore, the reduction of their observation quality and the shifting of their center of mass potentially impact the accuracy of the derived z-PCO^{GPS}. Here, the impact of the errors in z-PCO$_{LEO}$is mainly discussed. After adding an arbitrary +3 cm artificial bias to Swarm-A/B/C z-PCO, the correlation coefficients of the scenarios including the three satellites remain the same value, but the derived scale and z-PCO^{GPS} change significantly. Seen from scenarios 5*, 6*, and 7*, when one Swarm satellite is processed with a +3 cm-

biased z-PCO_{LEO} , ΔScale is about +4.3 ppb (+2.7 cm at the equator) larger than the result derived with official Swarm PCOs, and z-PCO^{GPS} shifted about −59 cm in average correspondingly. When the three z-PCO-biased LEOs are integrated together (scenario 11*), ΔScale is about +5.1 ppb (+3.3 cm at the equator) larger, and z-PCO^{GPS} shifted about −69 cm. If there are LEOs with official z-PCO in the processing, the impact of biased z-PCO_{LEO} is reduced (scenarios 13*, 15*, 16*, and 17*). The sensitivity of the scale to z-PCO_{LEO} is observed from the results mentioned above, for example, 3 cm bias in z-PCO_{LEO} leads to 4.2 ppb scale (2.7 cm at the equator). Therefore, it is concluded that the LEO receiver antenna offset in z-direction has to be accurate at the one-millimeter level in order to realize a one-millimeter accuracy scale at the equator. The requested one-millimeter accuracy for z-PCO_{LEO} is also reported by Glaser et al. (2020) based on a simulation study. The PCO_{LEO} used in this study are taken from the available sources with limited information in terms of their accuracy. However, an accurate PCO_{LEO} is the pre-requisite for a future mission dedicated to co-location in space (Biancale et al., 2017).

5.5 Cross-check and comparison between the two methods

Two different approaches to calibrate the z-PCO^{GPS} are introduced in Section 5.2. Base on a study with data of 2016, the LEO-based approach is discussed in the previous section. The second approach based on Galileo with calibrated antenna offsets is compared and cross-checked with the LEO-based approach in this section. The resulting z-PCO^{GPS} and scale values derived by an exemplary period processing(first half of 2019) are discussed. This period is selected to include as many Galileo satellites as possible.

5.5.1 Ground station selection and Swarm orbit quality

The first half-year of 2019 is selected as the processing period. During this period, the Galileo constellation already had 24 satellites in operation. All selected ground stations are tracking both GPS and Galileo, and the network is globally and evenly distributed. As a prerequisite for the scale realization, the stations should have accurate coordinates that are offered within the IGS weekly coordinate products (i.e., in IGS14 reference frame). There are 68 to 94 stations (only a few days less than 75) that are selected for different days. The majority of these stations are equipped with Galileo-calibrated receiving antennas (Figure 5.14), and for the others, the GPS L2 calibrations are applied for the E5a signal. Following the recommendation of the IGS, only stations providing observations in RINEX3 format to the IGS data centers are used. The station number increases around DOY (day of the year) 87 because more stations started to offer RINEX3

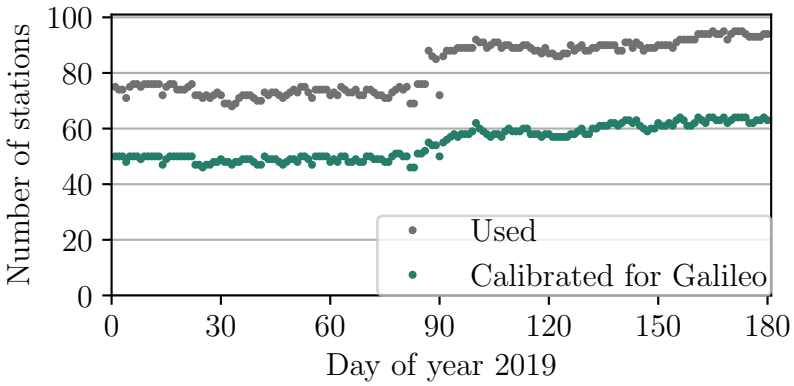

Figure 5.14: Number of stations selected for each day

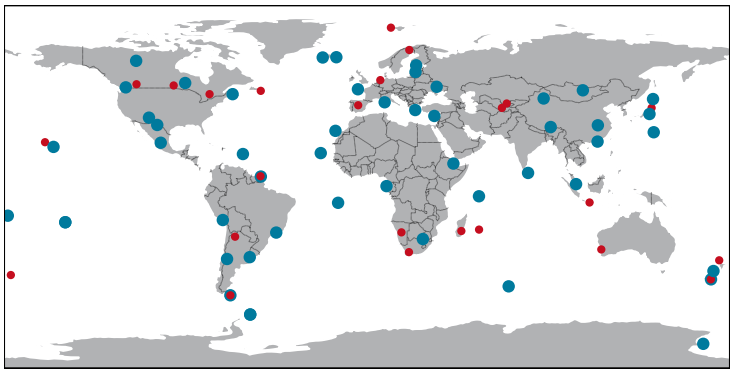

Figure 5.15: Distribution of the 75 stations selected for January 1st, 2019. Stations with Galileo antenna calibrations are marked in blue. Red denotes the stations using phase center corrections of GPS for the Galileo signals

observations from that day. Figure 5.15 presents the 75 selected stations for the processing of DOY 1 as an example.

For the LEO-based strategy, the three spacecraft of the Swarm mission are used. The data status of the three LEOs is presented in Figure 5.16. The gaps are caused by missing or bad quality data. To check the quality of the LEO observation data and to verify our orbit determination, a Swarm-only dynamic POD is done by using IGS final orbit and 30-second clock products. The data sampling rate is 30-second and the arc length is 24-hour. The dynamic POD of LEOs are carefully discussed in Section 3.3 based on

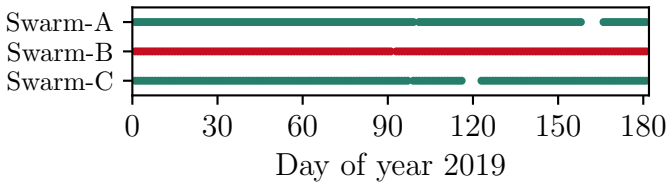

Figure 5.16: Data status of three Swarm satellites

Table 5.6: The validation of the orbits of Swarm satellites. The direction-specific RMS values of orbit differences compared to the office products are averaged over 180 days. The SRL validation is based on the observations of Yarragadee station. The residuals are averaged over epochs

	Orbit RMS compared to official products [mm]			SLR residuals [mm]	
	Along-track	Cross-track	Radial	Epochs	mean/STD
Swarm-A	30.9	15.1	25.3	1781	3.7±25.1
Swarm-B	29.7	12.2	21.0	4083	4.2±19.5
Swarm-C	30.3	14.8	25.1	1650	2.4±25.0

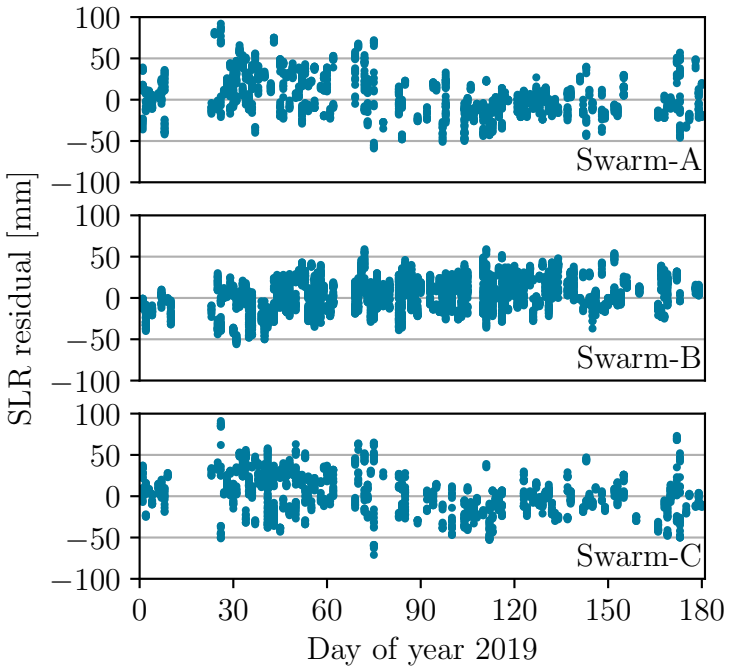

Figure 5.17: SLR observation residuals for the Swarm-A, B, and C POD solution for all passes of the Yarragadee station in Australia for 180 days. The gaps are caused by missing SLR observations

the data in 2016. However, it is necessary to check the quality of the Swarm orbits in this study. The determined orbits are compared with official products without Helmert transformation. The RMS of orbit differences is computed in the along-track, cross-track, and radial directions and averaged over 180 days (see Table 5.6). In general, the orbits of the three Swarm satellites are determined in similar accuracy with about 30 mm RMS in the along-track direction, 14 mm RMS in the cross-track direction, and 24 mm RMS in the radial direction. The orbits are also validated by the residuals of SLR observations. All SLR observations of the high-quality Yarragadee station in Australia during the 180 days are used to validate the Swarm orbits. The statistical results are also listed in Table 5.6, and all the epoch-wise solutions are shown in Figure 5.17. With the most observations, the SLR residuals of Swarm-B have the largest mean (4.2 mm) and the smallest variation (±19.5 mm). With similar numbers of observations, the SLR residuals (with variation) of Swarm-A and Swarm-C are 3.7±25.1 mm and 2.4±25.0 mm. Comparing with previous studies, the orbit quality of our solution is at a comparable level. The comparison to other studies is shown in Table 3.4.

5.5.2 Validation and analysis strategy

In general, the validation of z-PCO^{GPS} is challenging as the phase center offsets cannot be observed by space geodetic techniques. However, the different z-PCO^{GPS} estimated by both methods can be evaluated by comparison and cross-check. First of all, scale independence can be empirically analyzed by comparing the correlation between scale and phase center parameters of different cases. Using only ground-based GPS observations results in a large correlation coefficient of the two parameters (Schmid et al., 2007). Using both methods with different observations and constraints (on PCO^{GAL} or PCO_{LEO}) allows, secondly, to assess the agreement between the z-PCO^{GPS} estimates. For this purpose, six cases are designed and listed in Table 5.7. Different combinations of included satellites, PCO constraints, and estimated satellite z-PCO increments with respect to the a priori values (ΔPCO) are selected for the different cases. Since our focus is on the satellite z-PCO and the terrestrial scale, the satellite PCOs in x and y directions are always kept fixed. Case 1, as a reference case and discussed as type C situation in Section 5.4, shows the problem of a high correlation between the terrestrial scale and the z-ΔPCO^{GPS}. In cases 2 and 3, z-ΔPCO^{GPS} are estimated by fixing either PCO_{LEO} or PCO^{GAL}. Moreover, ground-based observations of GPS and Galileo and space-based GPS observations are combined in cases 4, 5, and 6. In case 4, both PCO^{GAL} and PCO_{LEO} are fixed to estimate the z-ΔPCO^{GPS}. In cases 5 and 6, z-ΔPCO_{LEO} or z-ΔPCO^{GAL} are estimated jointly with z-ΔPCO^{GPS} while only fixing PCO^{GAL} or PCO_{LEO} , respectively. These two cases allow the ultimate cross-check with the known Galileo and LEO offsets. However, it is debatable whether the gravitational constraint can be transferred from

Table 5.7: The six scenarios for deriving the GPS PCOs and GNSS-based terrestrial scale. The column named 'Satellites' shows the satellites included in the processing. 'Fixed' means the corresponding satellite PCOs are fixed to a priori values. The last column shows the satellite PCO-z correction estimated in the processing

	Cases	Satellites	Fixed	Estimated
1	G-G	GPS	-	z-ΔPCO$^{\mathrm{GPS}}$
2	GL-G	GPS LEOs	PCO$_{\mathrm{LEO}}$	z-ΔPCO$^{\mathrm{GPS}}$
3	GE-G	GPS GAL	PCO$^{\mathrm{GAL}}$	z-ΔPCO$^{\mathrm{GPS}}$
4	GEL-G	GPS GAL LEOs	PCO$^{\mathrm{GAL}}$ PCO$_{\mathrm{LEO}}$	z-ΔPCO$^{\mathrm{GPS}}$
5	GEL-GL	GPS GAL LEOs	PCO$^{\mathrm{GAL}}$	z-ΔPCO$^{\mathrm{GPS}}$ z-ΔPCO$_{\mathrm{LEO}}$
6	GEL-GE	GPS GAL LEOs	PCO$_{\mathrm{LEO}}$	z-ΔPCO$^{\mathrm{GPS}}$ z-ΔPCO$^{\mathrm{GAL}}$

the GPS space-based observations to the Galileo satellites or reversely (unfortunately, space-based observations are available only for GPS during 2019). This question will be discussed in Sections 5.5.3, 5.5.4 and 5.5.5. To improve the readability, the six cases are named based on the included satellites and the estimated z-ΔPCO. For example, GEL-GE means that GPS (G), Galileo (E), and Swarm (L) satellites are all included in the processing, and z-ΔPCO$^{\mathrm{GPS}}$ (-G) and z-ΔPCO$^{\mathrm{GAL}}$ (-E) are estimated while only the PCOs of Swarm satellites are fixed.

The results are analyzed from three aspects. Firstly, considering the relationship that 130 mm error in GPS z-PCO$^{\mathrm{GPS}}$ leads to one ppb terrestrial scale (Zhu et al., 2003), both the estimated z-ΔPCO$^{\mathrm{GPS}}$ and the derived terrestrial scale with respect to IGS14 are discussed. The further comparisons and the estimation quality analysis are based on the daily estimates, the formal error of the estimates, and the correlation coefficient of z-ΔPCO$^{\mathrm{GPS}}$ and scale. The variation of the estimated daily z-ΔPCO values, the formal error of z-ΔPCO, and the derived scale between the processed days are shown by the STD of their time series with respect to the mean. Both satellite-specific results and the results averaged over satellites (system-wise) are discussed in detail. Secondly, the z-ΔPCO estimated by fixing only the PCO$^{\mathrm{GAL}}$ in GEL-GL will be analyzed. The impact of fixed PCO$^{\mathrm{GAL}}$ on the estimation of z-ΔPCO$_{\mathrm{LEO}}$ is shown. At last, mainly based on GEL-GE, the z-ΔPCO$^{\mathrm{GAL}}$ estimated by fixing only the PCO$_{\mathrm{LEO}}$ is analyzed. The effect of transferring the gravitational constraint directly to GPS and indirectly to Galileo via

GPS satellites and ground stations is discussed.

5.5.3 Estimation of GPS phase offsets and the GNSS-based scale

In Figure5.18, the satellite-specific z-ΔPCO$^{\mathrm{GPS}}$ with respect to the IGS values and averaged over the 180 processed days are shown as blue bars. The vertical lines denote the STD for each time series. The last bar in each plot provides the mean value over all satellites, correspondingly the STD of the constellation-wise value is smaller than the satellite-specific values. The formal errors of z-ΔPCO$^{\mathrm{GPS}}$ and their STD are presented as green bars. Due to the evenly distributed ground network and satellite constellation, the formal errors are quite similar within one case. There is no obvious block-specific phenomenon visible. Although the z-PCO$^{\mathrm{GPS}}$ in the same block are similar, the z-ΔPCO$^{\mathrm{GPS}}$ are similar for all satellites in every case.

In the case G-G, the estimated z-ΔPCO$^{\mathrm{GPS}}$ values are smaller than 100 mm, but with large STD (100 to 130 mm), formal error (about 46 mm), and STD of formal error (about 22 mm) among all cases. The reason for this is the high correlation between the estimated z-ΔPCO$^{\mathrm{GPS}}$ and the terrestrial scale. Slight changes in any inputs of the estimation (e.g., the ground station network) lead to very different solutions, therefore, the precision of the estimated z-ΔPCO$^{\mathrm{GPS}}$ and the scale is low. Similar processing is performed in group C in Section 5.4.4. Although the two studies are using data from different stations and in different period (2016 and 2018), both solutions agree with each other in the large correlation coefficients (0.85 and 0.87) and the large variations of z-ΔPCO$^{\mathrm{GPS}}$ (about 100 mm) and scale(about 0.85 ppb).

In the other five cases, either z-PCO$^{\mathrm{GAL}}$ or z-PCO$_{\mathrm{LEO}}$ or both are fixed. Consequently, the precision of the z-PCO estimates is improved. In general, the results of the five cases show collective shifts of z-PCO$^{\mathrm{GPS}}$ with respect to the IGS values, and the satellite-specific values have a good agreement among the five cases. Comparing the results based on the gravitational constraint (GL-G) and on Galileo (GE-G), the z-ΔPCO$^{\mathrm{GPS}}$ values have differences of about 30 mm for all satellites. The STD of z-ΔPCO$^{\mathrm{GPS}}$, the formal error of z-ΔPCO$^{\mathrm{GPS}}$, and the STD of the formal error of GL-G are 12 mm, 5 mm, and 3 mm larger than those of GE-G, respectively. That means the precision of the LEO-PCO-fixed case is slightly lower than that of the Galileo-PCO-fixed cases. It is explained by the stronger constraint transferred by many more observations from 24 Galileo satellites compared to the three Swarm satellites, which is verified later in this section.

In the GEL-G case, both PCO$^{\mathrm{GAL}}$ and PCO$_{\mathrm{LEO}}$ are fixed, but the results are quite similar to GE-G. Similar results are obtained in GEL-GL in which only PCO$^{\mathrm{GAL}}$ are fixed. This demonstrates that the Galileo satellites are dominating the results due to

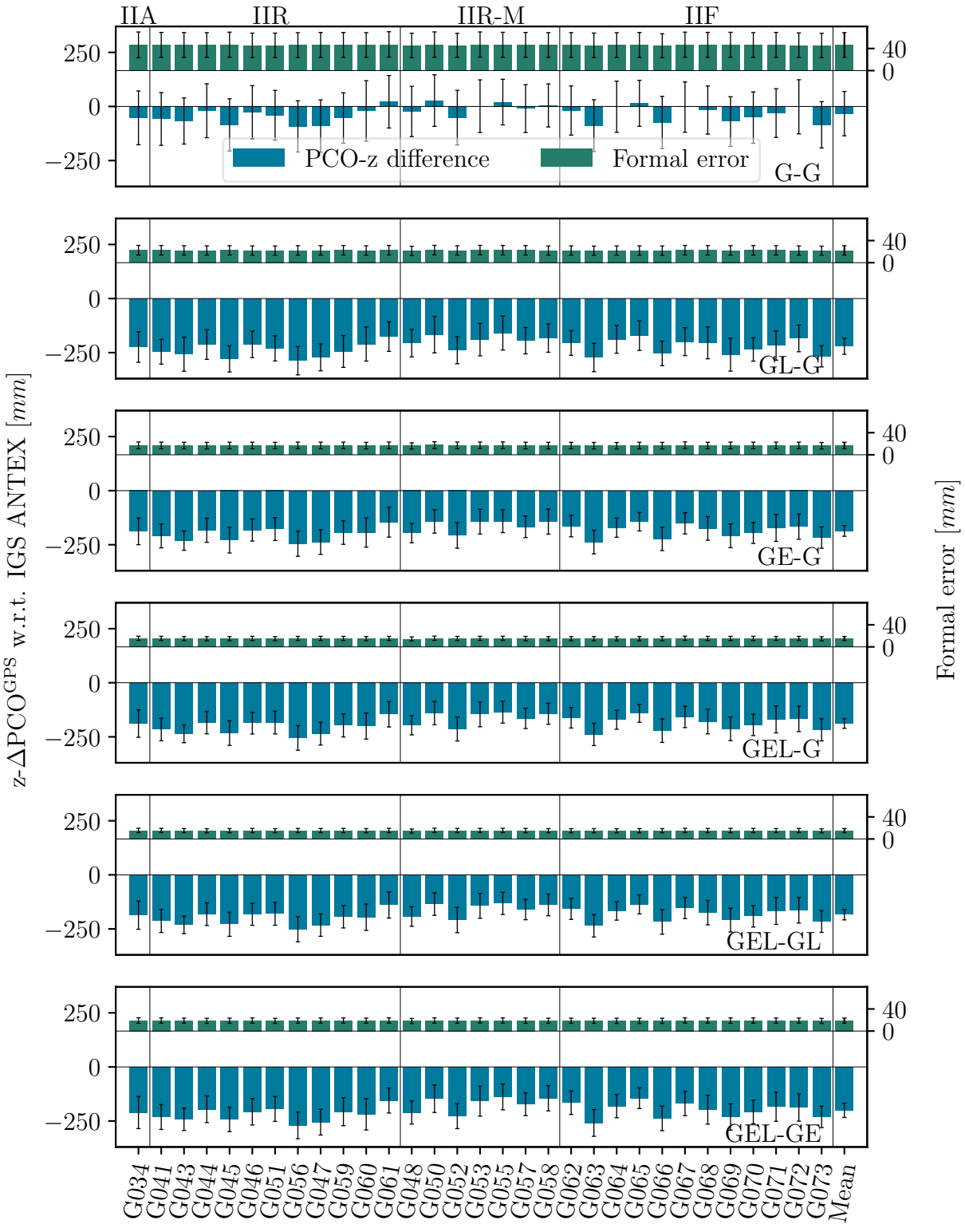

Figure 5.18: Estimated z-ΔPCO$^{\text{GPS}}$ compared to IGS values (blue) and their formal errors (green). Each bar denotes the solution averaged over 180 processing days. The error bars denote the standard deviation of the time series to the mean. The x-label presents the space vehicle number of the satellites and the satellites are sorted by block-wise.

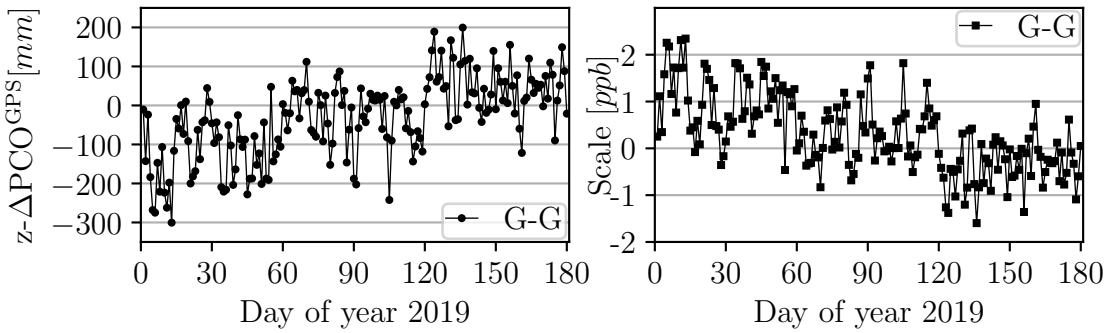

Figure 5.19: Time series of the estimated z-ΔPCO$^{\mathrm{GPS}}$ compared to IGS values averaged over satellites (left) and the corresponding scale with respect to IGS14 (right) in the case including GPS only without fixing the scale

the larger number of observations. In GL-G and GEL-GE, only the $\mathrm{PCO_{LEO}}$ is fixed. However, the result differences between GL-G and GEL-GE are larger than the resulting differences between GE-G, GEL-G, and GEL-GL. The z-ΔPCO$^{\mathrm{GPS}}$ values in GEL-GE are collectively larger by about 10 mm than that of GL-G. The STD of z-ΔPCO$^{\mathrm{GPS}}$, the formal error of z-ΔPCO$^{\mathrm{GPS}}$, and the STD of formal error are all smaller in GEL-GE than in GL-G. The differences between GL-G and GEL-GE are caused by including Galileo.

The time series of daily system-wise (averaged over satellites) z-ΔPCO$^{\mathrm{GPS}}$ and the corresponding terrestrial scale are shown in Figure 5.19 for G-G and in Figure 5.20 for the other five cases. The corresponding mean values and STD of all the time series are presented in Table 5.8 (left). Comparing the left (z-ΔPCO$^{\mathrm{GPS}}$) and the right (scale factor) plots, the relationship between the two parameters is shown. The variation of the time series in G-G is quite large (103 mm STD for z-ΔPCO$^{\mathrm{GPS}}$ and 0.823 ppb STD for terrestrial scale). The solutions of the Galileo-PCO-fixed solutions (GE-G, GEL-G, and GEL-GL) are very similar. The time series of GL-G and GEL-GE have larger variation and -20 to -40 mm differences in mean values of z-ΔPCO$^{\mathrm{GPS}}$ than those of the Galileo-PCO-fixed solutions. By including Galileo satellites, GEL-GE is more stable and closer to the Galileo-PCO-fixed solutions than GL-G.

The quality of the estimation in the different cases is also reflected in the correlation coefficients of the estimated z-ΔPCO$^{\mathrm{GPS}}$ and the terrestrial scale. The corresponding correlation coefficients averaged over satellites and days are presented in Table 5.8 (right). Overall, the coefficients are very stable with variations smaller than 0.01. G-G shows the largest correlation coefficient of z-ΔPCO$^{\mathrm{GPS}}$ and terrestrial scale (0.87) which agrees with the analysis mentioned above. The correlation coefficient can be reduced effectively by introducing LEOs or by processing GPS together with Galileo and fixing $\mathrm{PCO^{GAL}}$. Derived by different numbers of observations, the Galileo-PCO-fixed case GE-G is more effective than the LEOs-PCO-fixed case GL-G in de-correlation (reduction of 0.74 versus

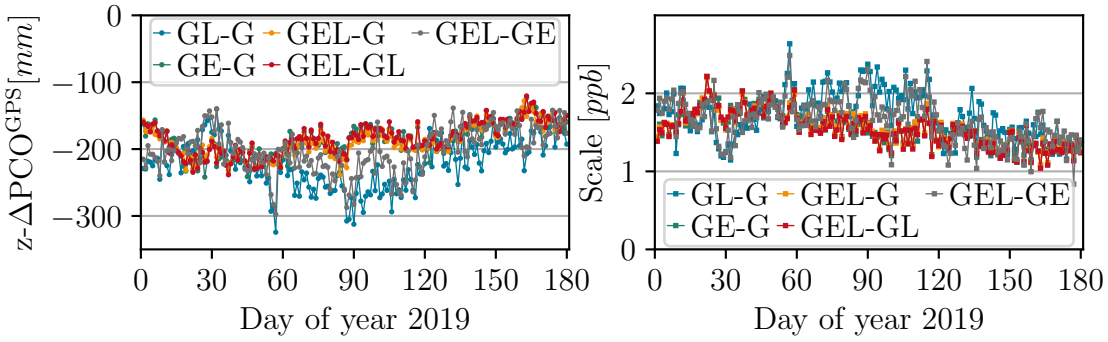

Figure 5.20: Time series of the estimated z-ΔPCO$^{\mathrm{GPS}}$ compared to IGS values averaged over satellites (left) and the corresponding scale with respect to IGS14 (right) for the five cases including Galileo or LEOs or both

0.35). Due to the stronger impact of Galileo on transferring the constraint compared to Swarm, the correlation coefficient nearly does not change after fixing PCO$_{\mathrm{LEO}}$ additionally (GEL-G and GEL-GL). The correlation coefficients in GEL-GL show that the fixed PCO$^{\mathrm{GAL}}$ can separate the derived terrestrial scale and the estimated z-ΔPCO$^{\mathrm{GPS}}$ for both GPS and LEOs. In GEL-GE, with only three PCO-fixed LEOs, the correlation between z-ΔPCO$^{\mathrm{GPS}}$ and terrestrial scale is identical for GPS and Galileo satellites (0.56) and is close to that of GL-G (0.52).

To investigate the impact of the numbers of Galileo and Swarm satellites on the estimation, GE-G is processed again by only including three Galileo satellites (E101, E210, and E212) in three different orbital planes (GE-G*). The statistic of the solution for GE-G* is presented in Table 5.8. With fewer Galileo satellites, the results of GE-G* are different from that of GE-G with a system-wise difference of 25 mm for the estimated z-ΔPCO$^{\mathrm{GPS}}$. This is caused by the weaker geometry and fewer observations of the three Galileo satellites compared to the full system. Without the advantage of more satellites, the precision of GE-G* becomes lower than that of the GL-G with 13 mm larger STD of the z-ΔPCO$^{\mathrm{GPS}}$ and 0.1ppb larger STD of the scale. Moreover, the correlation coefficient between z-ΔPCO$^{\mathrm{GPS}}$ and the terrestrial scale increases from 0.13 (GE-G) to 0.54 (GE-G*), which exceeds that of GL-G by 0.02. In a summary, due to the much faster geometry change, including three Swarm satellites gives more precise z-ΔPCO$^{\mathrm{GPS}}$ than including three Galileo satellites. Therefore, the Galileo method might be not sufficient for the early days of Galileo when there were very limited satellites in operation.

Besides the internal comparison and cross-check between the different cases, the results of this study are also compared with other studies. The system-wise z-ΔPCO$^{\mathrm{GPS}}$ derived by GE-G is between the robot-calibration-based solution and the chamber-calibration-based solution in Villiger et al. (2020). The estimated GNSS-based scale is compared with the scale determined by the VLBI and SLR. As reported by Altamimi et al. (2016),

Table 5.8: The estimated z-ΔPCO$^{\mathrm{GPS}}$ averaged over satellites and processed days and the scale factor with respect to IGS14 averaged over the processed days. The empirical standard deviations of the time series are also given. The correlation coefficients of the estimated satellite PCOs in the z-direction and the terrestrial scale. The values are averaged over satellites and processed days. Zero values are due to the fixing to the a priori values. The dash means not included

Case	z-ΔPCO$^{\mathrm{GPS}}$ [mm] mean/STD	Scale [ppb] mean/STD	z-ΔPCO$^{\mathrm{GPS}}$ vs. Scale	z-ΔPCO$^{\mathrm{GAL}}$ vs. Scale	z-ΔPCO$_{\mathrm{LEO}}$ vs. Scale
G-G	-33/103	0.31/0.82	0.87	-	-
GL-G	-221/37	1.72/0.31	0.52	-	0
GE-G	-186/25	1.55/0.22	0.13	0	-
GEL-G	-188/23	1.56/0.22	0.12	0	0
GEL-GL	-184/24	1.54/0.23	0.13	0	0.09
GEL-GE	-201/33	1.66/0.29	0.56	0.56	0
GE-G*	-161/50	1.44/0.41	0.54	0	-

the scale factors determined by VLBI and SLR with respect to the ITRF 2014 are about +0.77 ppb and -0.77 ppb, respectively. The GNSS-based scales derived by GL-G and GE-G cases are +1.72ppb and +1.55 ppb, respectively. Therefore, the GNSS-based scale derived by both methods agrees with each other well and agrees with the VLBI-based scale better than the SLR-based scale does. After removing the systematic errors in SLR data by Luceri et al. (2019), the scale derived by SLR is about +1 ppb toward ITRF 2014 scale. Therefore, the scales determined by GNSS in this study, by VLBI, and by SLR have an agreement of better than 1 ppb.

There is a question left regarding the increase of stations after DOY 89 shown in Figure 5.14. However, the impact of the additional stations on the estimates is not obvious. Only a slight decrease of the formal errors is observed in the analysis. This means that the amount of the stations (about 80) before the increase and their distribution is sufficient for the estimation already.

5.5.4 Estimation of LEO phase offsets

In the case of GEL-GL, z-ΔPCO$^{\mathrm{GPS}}$ and z-ΔPCO$_{\mathrm{LEO}}$ are estimated simultaneously by fixing all PCO$^{\mathrm{GAL}}$ to the GSA values. Figure 5.22 shows the time series of the estimated satellite-specific z-ΔPCO$_{\mathrm{LEO}}$. The mean and STD are -2.2 ± 2.5 mm, -2.6 ± 2.1 mm, and -1.1 ± 2.4 mm for Swarm-A, B, and C satellites, respectively. The plots of Swarm-A and Swarm-C are very similar, but that of Swarm-B is slightly different from them. This can be explained by their orbital configuration as introduced in Section 2.3. During DOY 55 to 57, the orbits of Swarm-B have a 10 mm larger RMS with respect to the official products than the other days, which might be caused by some unconsidered behavior of the spacecraft. This is assumed to cause the large deviation of the estimated z-ΔPCO$_{\mathrm{LEO}}$

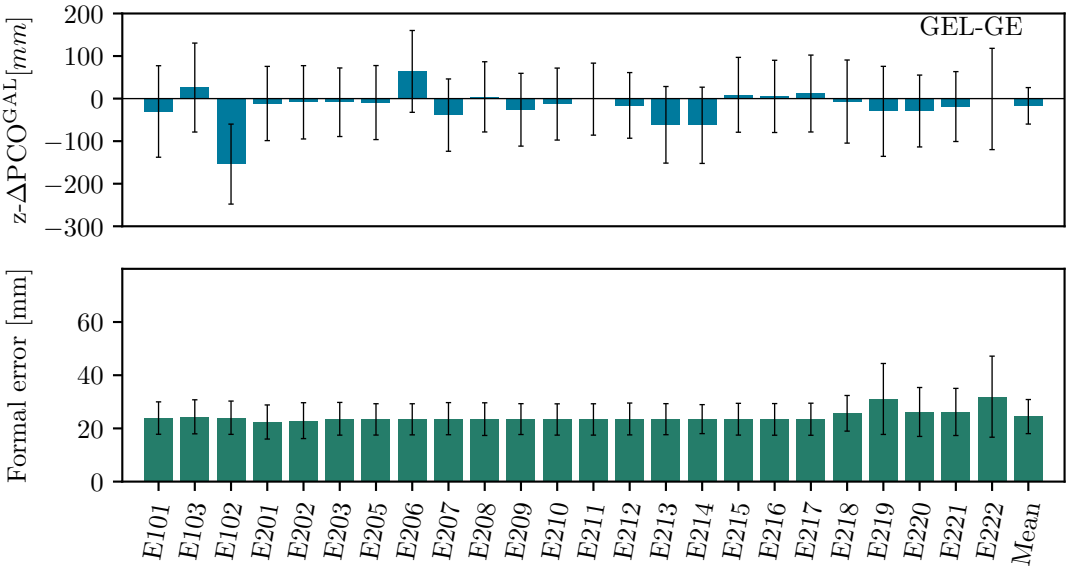

Figure 5.21: The estimated z-ΔPCO$^{\mathrm{GAL}}$ compared to *igsR3_2057.atx* (upper) and their formal errors (lower). Each bar denotes the solution averaged over 180 processing days. The thin errors bars denote the standard deviations of the time series

on those days. It also affects all the time series of z-ΔPCO$^{\mathrm{GPS}}$, z-ΔPCO$^{\mathrm{GAL}}$, and the scale derived by the LEOs-PCO-fixed cases. Therefore, it is concluded that orbit modeling quality has a large impact on the estimation.

All of the three time series show a periodic behavior. The periodicity might be related to the draconitic period, i.e., the period of two consecutive passes of the Sun through the orbital plane in the same direction, of Swarm, Galileo, and GPS. However, the processing period is too short for a reliable investigation. The impact of the periodicity can also be observed from the time series variation of z-ΔPCO$^{\mathrm{GPS}}$ and z-ΔPCO$^{\mathrm{GAL}}$ estimated in GL-G and GEL-GE in which only the z-PCO$_{\mathrm{LEO}}$ are fixed (Figure 5.20 and 5.25).

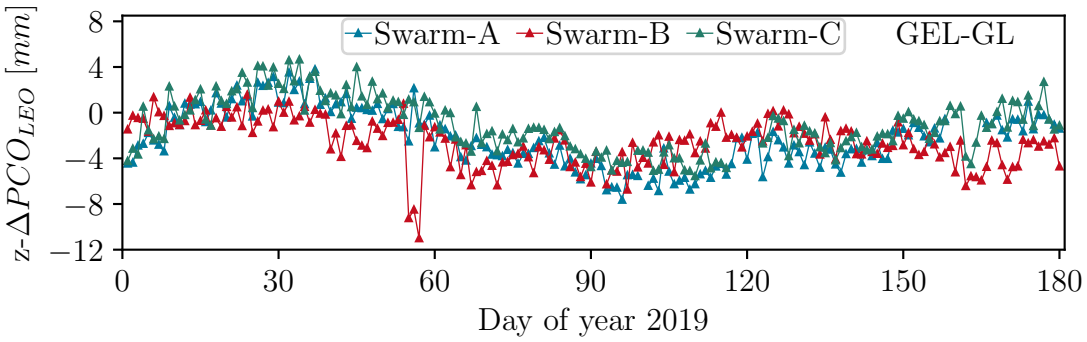

Figure 5.22: Time series of the estimated z-PCO$_{\mathrm{LEO}}$ of Swarm-A, B, and C compared to the a priori values (ESA offered) in the case including GPS, Galileo, and Swarm satellites and fixing only the PCO$^{\mathrm{GAL}}$.

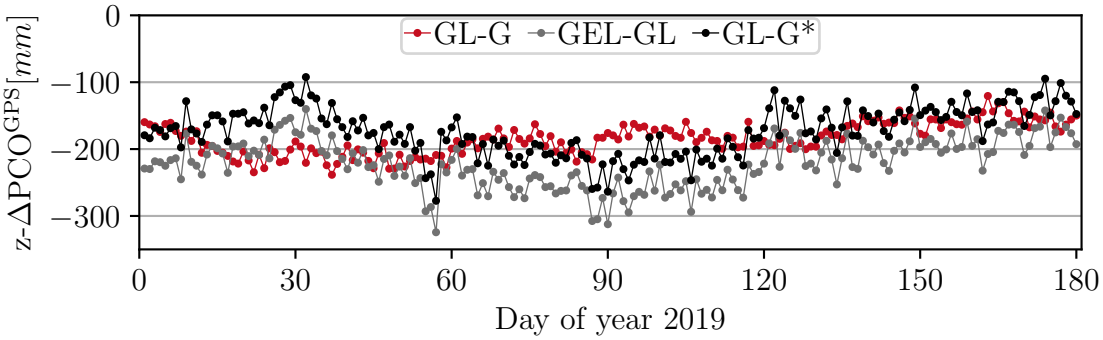

Figure 5.23: Time series of the estimated z-ΔPCO$^{\mathrm{GPS}}$ compared to IGS values averaged over satellites in three cases. GL-G includes GPS and Swarm satellites and the PCOs of Swarm satellites are fixed. GEL-GL includes GPS, Galileo, and Swarm satellites and only the PCOs of Galileo satellites are fixed. GL-G* is an update processing of GL-G by modifying the z-ΔPCO$_{\mathrm{LEO}}$ artificially.

From the magnitude of the estimated z-ΔPCO$_{\mathrm{LEO}}$, the importance of the accuracy of PCO$_{\mathrm{LEO}}$ can be realized. The scale factor between GL-G and GEL-GL has a 0.2 ppb (1.3 mm at the equator) difference, while the estimated z-ΔPCO$_{\mathrm{LEO}}$ in GEL-GL is 1-2 mm with respect to the a priori values which are fixed in GL-G. Additionally, an update for GL-G (GL-G*) is processed by using artificially modified Swarm PCOs by adding the estimated z-ΔPCO$_{\mathrm{LEO}}$ to the values offered by ESA. The time series of z-ΔPCO$^{\mathrm{GPS}}$ estimated in GL-G* is presented in Figure 5.23 (black). The curve of the updated case is systematically shifted from the curve of GL-G by 48 mm. However, the z-ΔPCO$^{\mathrm{GPS}}$ averaged over satellite and processed days is -173 mm which is much closer to the Galileo-PCO-fixed solution in GEL-GL (gray) than that of GL-G (red). This comparison shows the importance of the accuracy of PCO$_{\mathrm{LEO}}$ again.

5.5.5 Estimation of Galileo phase offsets

In the case GEL-GE, z-ΔPCO$^{\mathrm{GAL}}$ and z-ΔPCO$^{\mathrm{GPS}}$ are estimated simultaneously by fixing the PCOs of the three LEOs to a priori values and without constraining the terrestrial scale. This allows us to assess the estimated z-ΔPCO$^{\mathrm{GAL}}$ with respect to the values offered by GSA. Since the z-ΔPCO$^{\mathrm{GPS}}$ and the terrestrial scale derived in GEL-GE have small differences with respect to the solutions derived by the Galileo-PCO-fixed cases (GE-G, GEL-G, and GEL-GL), the estimated z-ΔPCO$^{\mathrm{GAL}}$ in GEL-GE are small. The satellite-specific z-ΔPCO$^{\mathrm{GAL}}$ values are presented as blue bars in Figure 5.21. The z-ΔPCO$^{\mathrm{GAL}}$ averaged over satellites is only -21 mm. The STD of the z-ΔPCO$^{\mathrm{GAL}}$ time series are about 80 mm to 100 mm for different Galileo satellites, and they are about 30 mm to 50 mm larger than that of the GPS satellites shown in Figure 5.18. The reason is that the gravitational constraint on LEOs is transferred only via the GPS satellites and the

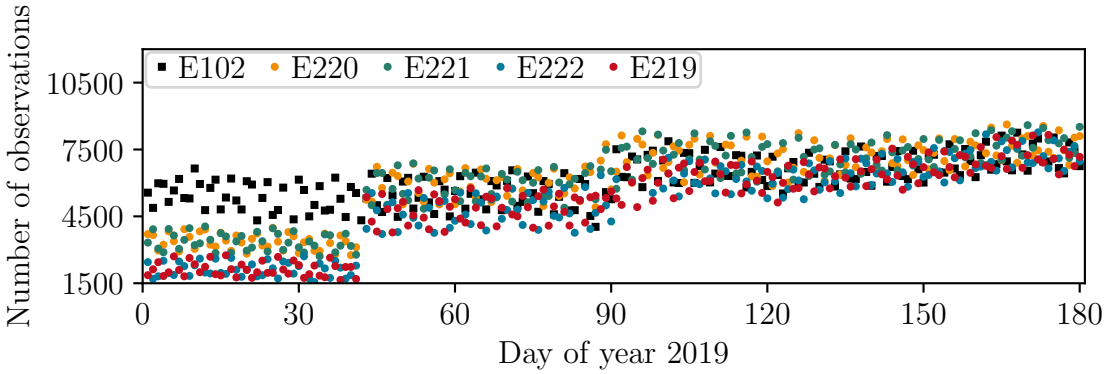

Figure 5.24: Number of ground-based observations that are used for the processing of Galileo satellites E102 (as a reference), E219, E220, E221, and E222 during the 180 processed days

ground stations to Galileo (Figure 5.3). Since the selected ground network changes day by day during the processed period, the impact on individual Galileo satellites will change. However, the constraints on the LEO orbits affect z-ΔPCO$^{\mathrm{GPS}}$ directly by onboard GPS observations, therefore, the variations of z-ΔPCO$^{\mathrm{GPS}}$ are smaller. Evaluating the impact on the whole Galileo constellation, the STD of z-ΔPCO$^{\mathrm{GAL}}$ averaged over all satellites is only 10 mm larger than that of GPS. The formal errors of z-ΔPCO$^{\mathrm{GAL}}$ and the STD of the formal errors are only about 6 mm and 2 mm larger than those of the estimated z-ΔPCO$^{\mathrm{GPS}}$. In general, the gravitational constraint on the LEOs acts on the estimation of z-ΔPCO$^{\mathrm{GAL}}$. Some unexpected phenomena also happen to satellite E102. A systematic change of the estimated z-ΔPCO$^{\mathrm{GAL}}$ is expected due to the scale change, but the absolute value of the estimated z-ΔPCO$^{\mathrm{GAL}}$ of E102 is much larger than all the other satellites. For example, the z-ΔPCO$^{\mathrm{GAL}}$ of E101 and E102 have a -123 mm difference. However, the a priori (GSA) z-PCOs of the two satellites have a $+87$ mm difference. That means our estimated z-PCO values of the two satellites are much closer (-36 mm difference) than their a priori values. This result agrees with the study by Steigenberger et al. (2016) that estimated similar z-PCOs of E101 and E102.

For the four Galileo satellites E219, E220, E221, and E222 launched in July 2018, they have larger formal errors than the other Galileo satellites. This is likely caused by fewer ground-based observations that were available during the first 43 processed days, as part of the ground stations were not offering data for them. The numbers of observations are shown in Figure 5.24. Moreover, the observations of satellites E222 and E219 reach a similar number as the other satellites in mid-2019. This is due to the limited capability of some ground receivers which only observe satellites with PRN smaller than 32 (Mozo, 2018).

The time series of system-wise z-ΔPCO$^{\mathrm{GAL}}$ and z-ΔPCO$^{\mathrm{GPS}}$ are plotted in Figure 5.25. As explained above, the variation of the z-ΔPCO$^{\mathrm{GAL}}$ time series is slightly larger (10 mm)

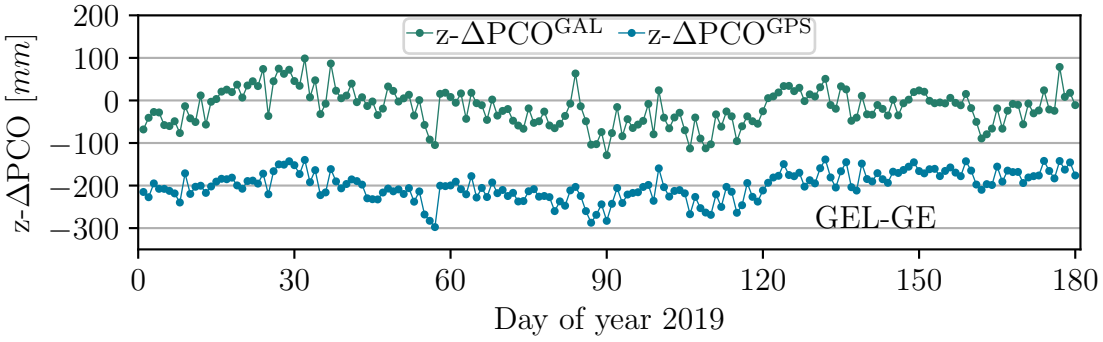

Figure 5.25: Time series of the estimated GPS and Galileo z-PCO differences with respect to *igsR3_2057.atx* averaged over satellites in the case including GPS, Galileo, and Swarm satellites and only fixing the PCOs of Swarm satellites

than that of z-ΔPCO$^{\mathrm{GPS}}$. However, due to the fixed $\mathrm{PCO}_{\mathrm{LEO}}$ and the same ground stations, they agree with each other.

5.6 Indirect estimation of the Geocenter

By re-solving the NEQ of four cases discussed in Section 5.5 with fixed PCOs of all satellites, some results and discussion about the geocenter are given in this section. The different centers of the Earth and the geocenter are briefly introduced below. For the Earth, there are four centers with respect to different physical or mathematical concepts (Dong et al., 2003):

- the center of mass of the whole Earth, including the mass of the solid Earth, the cryosphere, the ocean, the continental hydrosphere, and the Earth's atmosphere (CM);
- the center of mass of the solid Earth without mass load (CE);
- the center of figure of the outer surface of the solid Earth (CF);
- the center of a network consisting of a subset of ground stations attached to the solid Earth (CN).

The CM and the CE are defined by both the shape and the mass distribution of the Earth. The differences between the CM and the CE are caused by the temporal variable mass, i.e., the mass loading mainly caused by oceans, the atmosphere, and continental water. The CF and the CN are concepts defined by only the shape of the Earth or the network. The true CF is very difficult to be realized because it requires the summation over the entire solid Earth's surface. In practice, it is assumed that the CN of a subset of ground stations in a homogeneous distribution coincides with the CF. As introduced

Table 5.9: Three configurations for geocenter realization

Case	Estimate geocenter	NNR	NNT
1	No	Yes	No
2	Yes	Yes	Yes
3	No	Yes	Yes

in Section 2.4, the origin of the ITRS is conventionally defined to be at the long-term mean CM. The ITRF, as a realization of the ITRS, is derived from a set of geodetic stations located at the surface of the solid Earth in global distribution. Therefore, the origin of the ITRF is a CN in fact (CN≡CF). The origin of the ITRF is defined to have zero translations and translation rates at a certain epoch relative to the CM averaged over the time series of SLR solution provided by ILRS (Altamimi et al., 2011). However, the offset between the CF and the CM appears and varies periodically due to the mass re-distribution of the Earth(Dong et al., 2003). The offset is called the geocenter and its variation is called the geocenter motion. There are three approaches to determine the geocenter motion. The first one is based on the inversion of geophysical models, for example, the studies given by Dong et al. (1997) and Chen et al. (1999). A second method is also an inversion approach which is introduced by Blewitt (2003). Based on the measured deformations on the Earth's surface, the geocenter motion is derived indirectly. The last method is called the translational approach. As the satellites are orbiting the CM and the ITRF stations are attached to the surface of the solid earth, the geocenter can be estimated simultaneously with the dynamic orbits of the satellites and the coordinates of the geodetic stations. The detailed introduction of this approach is given by Wu et al. (2012). The general equation for this method reads (Meindl et al., 2013):

$$D = |\mathbf{r}(t_s) - (\mathbf{R}(t_r) - \mathbf{G}(t_r))| + \epsilon \tag{5.12}$$

where D is the distance measurement between the emission point and the receiving point, $\mathbf{r}$ is the position vector of the satellite relative to the CM, $\mathbf{R}$ is the position vector of the observing geodetic station relative to the CF of the reference frame, R for the position vector of the observer w.r.t. the origin of the reference system, G consequently is the position vector of the geocenter. The time epochs t_s and t_r are the emission and the receiving time of the signals. This equation is applicable for the estimation based on GNSS, SLR, DORIS, or jointly.

As the discussion is about the enhancement to the GNSS by including LEOs, the translational method is our focus in this study. Concerning the geocenter estimation, Zajdel et al. (2019) have summarized the three common types of processing (see Table 5.9). Case 1 is a practical processing model applied by the IGS analysis centers. When coordinates of stations are not constrained, the NNR condition is required to remove the singularity

of the NEQ as the stations coordinates, ERPs, and orbits are estimated simultaneously. Since geocenter is not estimated, the satellite orbits refer to the CF of the reference frame, i.e., the network. However, the origin of the dynamic orbits should be the CM. Therefore, the geocenter is absorbed by other terms, in particular by the stations coordinates. Since the NNT is not applied to the network, the translation of the resulting reference frame with respect to the a priori reference frame consists of the daily geocenter as the main part. However, this approach is influenced by the SPR modeling errors (Männel and Rothacher, 2017; Zajdel et al., 2019). Case 2 presents the proper model for the translational approach. The geocenter is estimated as an additional parameter by adding observations based on equation 5.12. This model is commonly applied in the geodetic community to estimate the geocenter (Blewitt et al., 2001; Lavallée et al., 2006; Wu et al., 2012). By integrating four LEOs with the GPS in this model, Männel and Rothacher (2017) reported significant improvements of geocenter estimation by including LEOs. However, the orbital modeling issues and other unmodeled noise still distort the solution in this case. Case 3 is an over-constrained case as the NNT and NNR conditions are applied together without estimating the geocenter. Therefore, the orbital origin (CM) and the network origin (CF) are forced to coincide with each other. This setup can be applied to figure out the potentially absorbed or hidden information of geocenter by the other aspects instead of the translation of the network.

Seeing from the configuration of the study in Section 5.5, the processing in this study is the same as case 1. Although the geocenter is not directly estimated as a parameter, based on the discussion above, the translation of the ground network with respect to the a priori coordinates (aligned to ITRF2014) represents the indirect geocenter. By fixing the PCOs of all satellites, the NEQ of four cases discussed in Section 5.5 is resolved, including GPS-only, Galileo-only, GPS+Galileo, and GPS+Swarm. The translations of the ground network between the estimated and the a priori coordinates can be simply computed. All the results are presented in Figure 5.26. The times series and the corresponding statistical results (mean±STD) are shown in the left plot. For each case, the variations in the x- and y-component are similar and smaller than that of the z-component. The reason is that the z-component of the geocenter is contaminated by the orbit modeling deficiencies, especially in the solar radiation pressure modeling, and the x- and y-axis are stabilized by Earth rotation (Meindl et al., 2013). In x- and y- components, the mean values of the four cases are similar. The two Galileo-included cases have about 6 mm larger mean values in the z-component than the other cases. The variation of the Galileo-only case is larger than other cases in three components. Zajdel et al. (2021) also reported a larger variation of geocenter derived by Galileo than that of GPS. It can be explained by the different numbers of satellites and orbital planes of the two systems (32 versus 24) (Meindl et al., 2013). In the GPS+Galileo case, the variations in x- and y-component

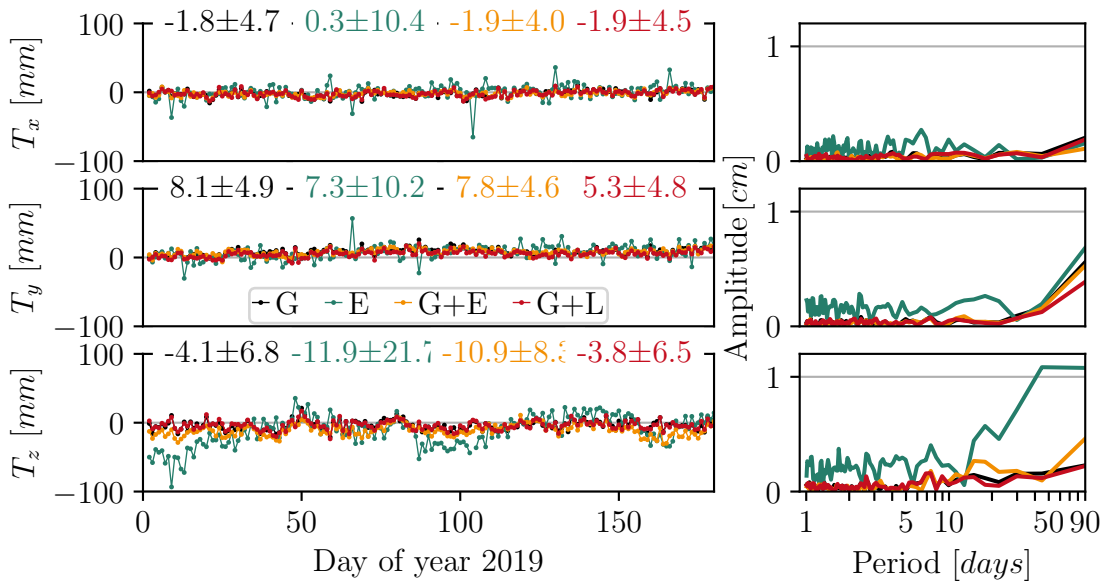

Figure 5.26: Translations in three directions of the ground network

are slightly smaller than that of the cases using only one of the two systems. However, the variation in the z-component is 1.5 mm larger than that of the GPS-only case and 13.4 mm smaller than that of the Galileo-only case. The mean of the z-component is dominated by the Galileo solution. By integrating the three LEOs of the Swarm mission with the GPS, the variations in the three components are slightly reduced by about 0.2 mm. The improvement agrees with the study by Männel and Rothacher (2017) but is not as significant as their study. Firstly, as discussed in the previous paragraph, they used the direct model whereas here only translation parameters are derived between the solution and the ITRF. Secondly, fewer LEOs (three versus four) and more ground stations (68 to 94 versus 53) are used. Moreover, the orbital geometry of the four LEOs they used is much more diverse than that of the three Swarm satellites. Thirdly, only half-year data is used and this is far away from a proper estimation of geocenter. The amplitude spectra are shown on the right of the figure. The larger variation of Galileo and the slight improvement due to the inclusion of LEOs are visible. The signal with a period close to 50 days for Galileo is visible. The interval of 52 days is the period between the epochs when the two out of three Galileo orbital planes have the same β angles(Zajdel et al., 2021). However, the processing period is too short to discuss the periodicity of the geocenter motion.

5.7 Summary

In Section 5.4, based on integrated processing of zero-difference ground and space-based GPS observations, the PCO^{GPS} in horizontal (x and y) and vertical (z) directions are

estimated and analyzed over day 115 to 365 in 2016 (251 days in total). For the first time, PCO^{GPS} are estimated based on observations recorded at ground stations and seven LEOs. The receiver antenna phase center positions of the seven LEOs are fixed by using the ground calibrated PCOs and without applying in-flight estimated PVs. The estimated PCO^{GPS} of this study is listed in the Appendix. Since this is a study based on a limited processing period to show the benefits of including LEOs, the resulting values should be used carefully. A reliable PCO^{GPS} product can be provided only based on an extended processing period. From the formal error analysis of GPS offsets in x- and y-directions, the benefits resulting from the additional observations and the fast-changing observation geometry can be seen. The correlations between the horizontal offsets and the orbit as well as the attitude of the GPS spacecraft are reduced. The formal errors of x-PCO^{GPS} and y-PCO^{GPS} in the large orbital β angle period are significantly reduced after adding seven LEOs to the processing. The STD of the estimated x-PCO^{GPS} and y-PCO^{GPS} are also reduced in general. The improvement of adding seven LEOs is comparable with adding 42 carefully selected ground stations. The z-PCO^{GPS} is estimated in different scenarios, e.g., with or without LEOs, scale-fixed or scale-free, and different ground networks. The correlation between the β angle and the z-PCO^{GPS} is not visible in any scenarios. By adding seven LEOs to 54-station, 75-station, 96-station, and 128-station based processing without applying the NNS condition, the correlation coefficient between the z-PCO^{GPS} and the scale is reduced significantly from about 0.85 to 0.3, 0.35, 0.4, and 0.42. As expected by the gravitational constraint, the inclusion of LEOs to the processing separates the z-PCO^{GPS} and the scale and improves the precision of the estimation. When the scale is constrained to the IGb08 scale, due to the additional observations from LEOs, there is a slight difference between the scenarios with and without LEOs. After removing the scale constraint, the z-PCO^{GPS} and the scale derived by ground-only scenarios vary significantly due to the ground geometry differences, while that of LEOs-integrated scenarios are very stable. The estimated z-PCO^{GPS} from the LEOs-integrated scenarios are about -25.5 cm (averaged over four scenarios) different from *igs08_1930.atx*. Moreover, taking the -6 cm difference between *igs08.atx* and *igs14.atx* into account, our solution agrees to the z-PCO^{GPS} estimated by Rebischung (2019) (based on calibrated offsets of Galileo) with 3.1 cm difference averaged over all GPS satellites. Based on the results of 17 additional scenarios in the 25-day processing, it can be concluded that the number of LEOs and the total number of observations from LEOs impact the de-correlation of the z-PCO^{GPS} and the scale. The de-correlation due to extended observation nadir angles is realized. The impact of LEOs orbital plane diversity is not obvious. By adding an artificial bias to the z-PCO_{LEO}, the impact of z-PCO_{LEO} on the z-PCO^{GPS} and the scale determination is shown. A $+3$ cm z-PCO_{LEO} bias leads to a $+4.2$ ppb ($+2.7$ cm at the equator) change of the scale and a -59 cm shifting of z-PCO^{GPS} in average. Therefore, an 1 mm accuracy on

z-$\mathrm{PCO_{LEO}}$ is required to estimate the scale in 1 mm accuracy at the equator.

In Section 5.5, using two different methods based on (1) the Galileo system with ground-calibrated antenna offsets and on (2) the gravitational constraint on LEO orbits, the scale-independent z-$\mathrm{PCO^{GPS}}$, and the corresponding GNSS-based terrestrial scale are determined. Applying the first method, a -186 ± 25 mm z-PCO correction with respect to the IGS values is found, and a $+1.55\pm0.22$ ppb terrestrial scale with respect to the IGS14. The results of the gravitational constraint method are -221 ± 37 mm for the z-PCO and $+1.72\pm0.31$ ppb for the terrestrial scale. The solutions derived by the two independent methods with different observations and metadata agree well with each other. The Galileo-based solution agrees very well with the latest study by Villiger et al. (2020). Moreover, these two solutions also agree with the VLBI-based scale (+0.77 ppb) better than the SLR-based scale (-0.77) does. Additionally, these solutions in 2020 also agree with the solutions in 2016 (group D solutions in Section 5.4.4). Comparing with the updated SLR-based scale without systematic errors (Luceri et al., 2019), the scales determined by GNSS in this study, by VLBI, and by SLR agree with each other with differences smaller than 1 ppb. Since Galileo offers many more observations which transfer the constraints than the Swarm constellation, Galileo dominated the results of the case in which the PCOs of both Galileo and LEOs are fixed. According to the correlation coefficient of z-$\Delta\mathrm{PCO^{GPS}}$ and scale, the formal error of z-$\Delta\mathrm{PCO^{GPS}}$, and the STD of the time series, the precision and stability of the solution derived by the Galileo-PCO-fixed method is higher than that derived by the LEO-PCO-fixed method. This is mainly caused by the different number of satellites and observations from Galileo and Swarm. If Galileo is reduced from the full constellation to only three satellites, the Swarm-based method leads to better results due to the shorter orbit period of Swarm satellites leading to faster changes in observation geometry. The joint estimation of z-$\Delta\mathrm{PCO^{GPS}}$ and z-$\Delta\mathrm{PCO_{LEO}}$ by only fixing $\mathrm{PCO^{GAL}}$ showed that the z-$\Delta\mathrm{PCO^{GPS}}$ and the derived scale factor are very close to the solutions derived by the case including GPS and Galileo and fixing the $\mathrm{PCO^{GAL}}$. Consequently, the constraint from Galileo is very strong and is nearly unaffected by including LEOs. The z-$\Delta\mathrm{PCO_{LEO}}$ is precisely estimated at 1 to 2 mm with respect to the values offered by ESA. This shows the small difference between the two methods again. Moreover, the accuracy of the z-$\mathrm{PCO_{LEO}}$ is very important for the gravitational constraint method. Some periodic variations are realized in the z-$\Delta\mathrm{PCO_{LEO}}$ time series. This is also visible in the time series of z-$\Delta\mathrm{PCO^{GPS}}$, z-$\Delta\mathrm{PCO^{GAL}}$, and scale derived by applying only the gravitational constraint and might be related to the draconitic period of GPS and Swarm constellations. Based on the unusual results of the Swarm-B satellite in three days, the importance of orbit modeling quality is shown. The z-$\Delta\mathrm{PCO^{GAL}}$ estimated by only fixing $\mathrm{PCO_{LEO}}$ in the GPS, Galileo, and Swarm joint processing differs on average by -21 mm from the values offered by GSA. This difference corresponds to 0.13 ppb difference in the terrestrial scale.

The estimated z-ΔPCO$^{\mathrm{GPS}}$ and scale have slight differences from the results derived by the case, which includes only GPS and LEOs. The precision and stability of z-ΔPCO$^{\mathrm{GAL}}$ are both worse than that of the simultaneously estimated z-ΔPCO$^{\mathrm{GPS}}$. The gravitational constraint on the Swarm orbits is partially transferred to the Galileo satellites. This situation can be improved by including more LEOs and moreover, by including Galileo space-based observations, which will be available soon for the Sentinel-6 mission.

In Section 5.6, the methods and models for the estimation of geocenter are briefly introduced. By resolving the NEQ of the processing in Section 5.6, the indirect geocenter realization is performed. From the results of the 180-day processing, the indirect geocenter is visible in the ground network translations by four cases including GPS-only, Galileo-only, GPS+Galileo, and GPS+Swarm. The solutions agree with the theory and the previous studies. The variation in the z-component of the geocenter is larger than that of the x- and y- components due to the contamination by the orbit modeling deficiencies. Due to the few satellites of Galileo than the GPS, the variations of Galileo-solution is larger than that of GPS-only solution. The slight improvement by integrating the LEOs of Swarm with the GPS is visible.

-

Conclusion and outlook

This study is based on the well-developed theory, methods, and software for POD of GNSS satellites and LEOs which was contributed by a lot of researchers in previous studies. Instead of investigating fundamental concepts, e.g., developing a better model for perturbations acting on satellites, this thesis focuses more on experiment design, data processing, and result analysis regarding the integration of LEOs into ground-based GNSS processing. My main goal is to answer the questions in which aspects and how much the integrated processing with LEOs can enhance the GNSS. The answer starts from the benefits brought by LEOs due to their characteristics. Firstly, LEOs offer additional observations. Although additional stations also give more observations, they might be unavailable due to various reasons, e.g., the limited ground segment of a GNSS. Secondly, LEOs move rapidly as kinematic stations relative to GNSS satellites with much more diverse observing geometry than ground stations. Thirdly, due to the altitudes of LEOs, they expend the maximum bore-sight angels of the GNSS satellite as additional geometry diversity. Last but not the least, the additional orbit dynamics of LEOs are very important for some geodetic parameters. Considering the above-mentioned benefits of LEOs, the improved GNSS satellite orbits, improved x-PCO$^{\mathrm{GPS}}$ and y-PCO$^{\mathrm{GPS}}$, scale-independent z-PCO$^{\mathrm{GPS}}$, and purely GNSS-based scale are achievable in an integrated processing of ground- and space-based observations. Based on the results of well-designed studies, all the expectations are validated. Although the available LEOs with GNSS observations were limited in history, especially the LEOs operating in a common period, this issue has been relieved in recent years by new launched LEOs. Therefore, all investigations in this study are based on real data in 2016 and 2020. There some LEO launched in recent years are equipped with multi-GNSS receivers to obtain observations of both GPS and another system, e.g., FenYun-3C obtaining BeiDou observations and Sentinel-6 obtaining Galileo observations. However, GPS satellites are observed by the most amount of LEOs. Therefore, GPS is studied as the representative of all GNSS. Some detailed summaries about the investigations are given at the end of the corresponding chapters. The conclusions in the top view of this study are given below.

At the beginning of this study, it is important and necessary to understand the background knowledge including the study objects, theory, and methods. As the basis

for the investigations, the knowledge from previous studies is presented in Chapter 2. Together with the general introduction of the other three space geodetic techniques (VLBI, SLR, and DORIS), the GNSS are carefully introduced by focusing on their space and ground segments. Accordingly, the concern on the potential limitation of GNSS stations is raised. Afterward, as another main space object in this study, the missions with LEOs in history and in operation are introduced by focusing on the long-term data status and orbital characteristics, especially for the seven LEOs used in this study, including GRAEC-A/B, OTSM/Jason-2, Jason-3, Swarm-A/B/C. A comparison between LEOs and the MEO satellite of GNSS is given to address the advantage, disadvantages, and co-location of the two types of satellites. A brief introduction about reference systems and their transformation is given as they are key issues for the POD. Then the methods of kinematic and dynamic POD are presented. Since only dynamic POD is used in this study, more detailed information about it is given, including the perturbations, the modeling, and the differences between the POD of GNSS satellites and LEOs. At the end of Chapter 2, as the connection between the geodetic measurements and the dynamic orbits, the GNSS observations and motion equations are introduced, and the processing configurations for this study are summarized.

The separated POD for GNSS satellites and LEOs are performed in Chapter 3 to validate the orbit quality because it is the pre-requirement for the integrated processing. By using the data of about 100 stations which are global and evenly distributed, the orbits of GPS, GLONASS, and Galileo are determined in the first 30 days of 2020. The orbits of GNSS satellites are determined in the accuracy of a few centimeter-level with respect to official products. The orbit difference RMS of Galileo is similar to but slightly larger than that of GPS whereas they are compared to different products. Due to the ambiguity fixing issued caused by the FDMA signal and the modeling uncertainties of GLONASS, the RMS of GLONASS is significantly larger than that of the other two systems. Due to the orbit dynamics, the orbit in the along-track component is worse than in cross-track and radial components for all systems. By estimating Helmert transformation parameters in the orbit comparison, the systematic differences caused by the datum definition and the ERP are removed. The GNSS orbits are also validated internally by position difference in the day-boundary epoch. The results agree with the external comparison. Adding new LEOs into PANDA software requires a lot of experience, implementation work, and testing. The key points for this mainly technical issue are summarized. The orbits of the seven LEOs are determined by using 100-day data in 2016. The LEOs orbits are also determined in the accuracy of a few centimeter levels with respect to the produces offered by mission operators. However, the LEO orbits are slightly worse than the other studies due to some modeling issues, e.g., Earth radiation, unimplemented stochastic pulses, and uncertain PCOs. The SLR validation for the LEOs orbits is comparable with

the previous studies. Overall, the orbit quality of GNSS satellites and LEOs are sufficient for the integrated processing. As an additional contribution to the data cleaning issue, a more efficient outlier detection method for pseudo-range observations is developed. The detection rate is improved to 97.4% (37% improvement) comparing with the regular data cleaning method. Consequently, it also improves the initial orbits of LEOs. However, the method still has some shortcomings compared with other methods, for example only effective to the epochs with a unique and extreme outlier. The combination of this method with others needs further study.

As one of the main topics in this study, the orbit improvement of GNSS satellites by integrating LEOs is discussed in Chapter 4. A review of the previous studies presents the benefits of including LEOs to the POD of GNSS satellites and the various algorithms and methods of the integrated processing. However, only one or two LEO missions were included in the previous studies. Therefore, seven LEOs operating at the same time in 2016 are included to investigate how much LEOs can contribute to the GNSS satellite orbits and which parameter impact on the improvement. Only based on the space-based observations of the seven LEOs in one day, the expectation of the improvement is given. The real data processing is performed in 2016 according to the data status of the LEOs. A 26-station ground network in a global and sparse distribution is supplemented by different subsets of seven LEOs to determine the orbits of GPS satellites during 2016. A 34% improvement of the GPS orbit in 1D-mean RMS (from 37.5 mm to 23.9 mm) is archived by including seven LEOs. Both the number of space-based observations and the LEO orbital geometry affect the GPS orbits. The latter one is proved to be more important. This conclusion also meets the analysis only based on space-based observations. However, the impact of LEO orbit modeling quality is not discussed. The impact on the clock corrections of GPS satellites is not considered.

Chapter 5 includes the discussion about several issues which are related to each other. The first issue is about the GPS phase center offsets in horizontal, i.e., x-PCO$^{\mathrm{GPS}}$ and y-PCO$^{\mathrm{GPS}}$. During the period with large β angles, the x-PCO$^{\mathrm{GPS}}$ and y-PCO$^{\mathrm{GPS}}$ are correlated with the orbits of GPS satellites. By including LEOs, this issue can be partially dissolved. The data of the seven LEOs in 2016 are used again to supplement a more dense ground network with 54 stations. The formal errors of x-PCO$^{\mathrm{GPS}}$ and y-PCO$^{\mathrm{GPS}}$ are significantly reduced after adding seven LEOs, especially in the period of large β angle (14% and 17.7% reduction when β angle larger than 70°). The additional observations and geometry brought by the LEOs reduce the correlations between the x/y-PCO$^{\mathrm{GPS}}$ and the orbit as well as the attitude of the GPS spacecraft. The improvement of adding seven LEOs is comparable with adding 42 carefully selected ground stations. However, to get a more reliable solution, as long as possible processing period is required due to the slow change of solar elevation angle relative to the GPS orbital plane. The second issue is about

the GPS phase offset in vertical, i.e., z-PCO$^{\mathrm{GPS}}$. In the same processing for the x-PCO$^{\mathrm{GPS}}$ and y-PCO$^{\mathrm{GPS}}$, z-PCO$^{\mathrm{GPS}}$ is also estimated. However, the processing is extended to 16 scenarios in four groups which are classified by the number of ground stations, the applied constraints, and whether LEOs are included. Due to the additional orbit dynamics of the seven LEOs, in the case without applying a no-net-scale constraint to the ground network, the correlation coefficients between the GPS z-PCOs and the scale are reduced from 0.85 to 0.3. A -25.5 cm system-specific z-PCO$^{\mathrm{GPS}}$ corrections with respect to *igs.08.atx* is estimated by the LEOs integrated processing. The estimated z-PCO$^{\mathrm{GPS}}$ is stable during the days (about 55 mm STD) and in cases including different numbers of ground stations (less than 1 cm differences). Since the z-PCO$^{\mathrm{GPS}}$ is estimated independently from the terrestrial scale, the GNSS-based scale is realized at the same time. The GNSS-based scale is the third issue with is highly correlated with the z-PCO$^{\mathrm{GPS}}$. Besides the de-correlation by introducing gravitational constraints on the LEOs, another approach for the z-PCO$^{\mathrm{GPS}}$ estimation and GNSS-based scale realization is based on the Galileo with ground calibrated PCOs. By using the data of the first 180 days of 2019 when Galileo is in a full constellation, the LEO-integrated approach (three Swarm satellites included) is compared and cross-checked with a Galileo-based approach. They provide mean z-PCO$^{\mathrm{GPS}}$ corrections of -186 ± 25 mm and -221 ± 37,mm with respect to the IGS values, and $+1.55\pm0.22$ ppb and $+1.72\pm0.31$ ppb in the terrestrial scale with respect to the IGS14 reference frame. The results of both methods agree with each other with only small differences. The results also agree with the 2016 results mentioned above and the other studies. Due to the larger number of Galileo observations, the Galileo-PCO-fixed method leads to more precise and stable results. In the joint processing of GPS+Galileo+Swarm in which both methods are applied, the constraint on Galileo dominates the results. We discuss and analyze how fixing either the Galileo transmitter antenna z-PCO or the Swarm receiver antenna z-PCO in the combined GPS+Galileo+Swarm processing propagates to the respective freely estimated z-PCO of Swarm and Galileo. In addition, similar to the strategy used for the integrated POD study, different subsets of the LEOs in 2016 are integrated with the 54-stations network to study the impact of individual LEOs on the estimation. However, the importance of orbital diversity is not visible in this investigation. The number of space-based observations is the main factor impacting the solutions. The more observations from more LEOs are used, the smaller the correlation coefficient of z-PCO$^{\mathrm{GPS}}$ and terrestrial scale is derived. By adding a $+3$ cm artificial z-PCO offset to the three Swarm satellites, the importance of the accuracy of z-PCO$_{\mathrm{LEO}}$ is shown. A 1 mm accuracy on z-PCO$_{\mathrm{LEO}}$ is required to estimate the scale in 1 mm accuracy at the equator. This conclusion agrees with other studies. The last issue is about the geocenter estimation. Previous studies have discussed the benefits of including LEOs in the geocenter estimation and the geocenter determined by multi-GNSS. As an extension study of the z-PCO$^{\mathrm{GPS}}$

, the geocenter is estimated in GPS-only, Galileo-only, GPS+Galileo, and GPS+Swarm scenarios for the 180 days in 2019. Although the period is too short to discuss the periodicity of the geocenter motion, the results agree with the previous studies.

This study will be continued in the upcoming InGE project mentioned in Chapters 3 and 5. Several jobs should be done:

- The processing period should be expended as long as possible to get more reliable solutions and invisible phenomenon in short term results. This is important for the z-PCO^{GPS} , the GNSS-based scale, and the geocenter.
- Related to the previous point, as many LEOs as possible should be implemented into the software to avoid gaps in time series, for example, GRACE-FO satellites, Sentinel series satellites, etc. From another point of view, when more LEOs are processed in the same periods, the studies in this thesis might have some new discovery.
- The solar radiation model for different GNSS should be updated to the state-of-art standard.
- The modeling for perturbations should be completed and updated, for example, the implementation of Earth radiation to the LEOs and the updating of Earth gravity field.

There are also some open questions left in this study and some related topics which are worth to be investigated:

- The impact of different characteristics and modeling of the LEO orbits on the integrated POD should be investigated.
- The clock corrections of GNSS satellites are worth to be analyzed in the integrated POD.
- The ambiguity fixing algorithm is not applied to LEOs observations, i.e., formatting flying situation, which could improve the derived LEO orbits.
- The PVs of GNSS transmitting antennas and LEOs receiving antennas should be considered in the PCO study.
- The PCO of other GNSS can be calibrated as well. For example, the PCOs of GLONASS satellites can be estimated by applying the two methods in this study.
- The Galileo+GPS on-board observations from Sentinel-6 or other future missions give an opportunity to validate the two methods more directly.
- The more consistent orbits of GNSS satellite and LEOs is always a goal of study.

- Further investigations of potential improvements in the station coordinates and the TRF parameters are necessary.
- Other objects can be determined based on the long-term multi-LEO constellation, for example, atmosphere density and electron content above LEO orbits.

Bibliography

Abbondanza C, Chin TM, Gross RS, Heflin MB, Parker JW, Soja BS, van Dam T, Wu X (2017) JTRF2014, the JPL Kalman filter and smoother realization of the International Terrestrial Reference System. J Geophys Res Solid Earth 122(10):8474–8510, DOI 10.1002/2017JB014360

Altamimi Z, Collilieux X, Métivier L (2011) ITRF2008: an improved solution of the international terrestrial reference frame. Journal of Geodesy 85(8):457–473, DOI 10.1007/s00190-011-0444-4

Altamimi Z, Rebischung P, Métivier L, Collilieux X (2016) ITRF2014: A new release of the International Terrestrial Reference Frame modeling nonlinear station motions. Journal of Geophysical Research: Solid Earth 121(8):6109–6131, DOI 10.1002/2016JB013098

Arnold D, Meindl M, Beutler G, Dach R, Schaer S, Lutz S, Prange L, Sośnica K, Mervart L, Jäggi A (2015) CODE's new solar radiation pressure model for GNSS orbit determination. Journal of Geodesy 89(8):775–791, DOI 10.1007/s00190-015-0814-4

Bancroft S (1985) An algebraic solution of the GPS equations. IEEE transactions on Aerospace and Electronic Systems AES-21(1):56–59

Bar-sever Y, Haines B, Bertiger W, Desai S, Wu S (2007) Geodetic Reference Antenna in Space (Grasp) – a Mission To Enhance Space-Based Geodesy. In: COSPAR colloquium: scientific and fundamental aspects of the Galileo program, Padua., 1, pp 1–12

Bar-Sever YE, Russ KM (1997) New and improved solar radiation models for gps satellites based on flight data. Tech. rep., CALIFORNIA INST OF TECHNOLOGY PASADENA JET PROPULSION LAB

Berger C, Biancale R, Barlier F, Ill M (1998) Improvement of the empirical thermospheric model DTM: DTM94 - a comparative review of various temporal variations and prospects in space geodesy applications. Journal of Geodesy 72(3):161–178, DOI 10.1007/s001900050158

Bertiger W, Desai SD, Dorsey A, Haines BJ, Harvey N, Kuang D, Sibthorpe A, Weiss JP (2010) Sub-Centimeter Precision Orbit Determination with GPS for Ocean Altimetry. Marine Geodesy 33(sup1):363–378, DOI 10.1080/01490419.2010.487800

Bettadpur S (2012) Gravity recovery and climate experiment: Product specification document (rev 4.5–february 20, 2007). Tech. rep., Center for Space Research, the University of Texas at Austin

Beutler G, Brockmann E, Gurtner W, Hugentobler U, Mervart L, Rothacher M, Verdun A (1994) Extended orbit modeling techniques at the CODE processing center of the international GPS service for geodynamics (IGS): theory and initial results. Manuscr Geod, Vol 19, No 6, p 367 - 386 19(6):367–386

Biancale R, Pollet A, Coulot D, Mandea M (2017) E-GRASP/Eratosthenes: a mission proposal for millimetric TRF realization. In: EGU General Assembly Conference Abstracts, vol 19, p 8752

Blewitt G (1990) An Automatic Editing Algorithm for GPS data. Geophysical Research Letters 17(3):199–202, DOI 10.1029/GL017I003P00199

Blewitt G (2003) Self-consistency in reference frames, geocenter definition, and surface loading of the solid Earth. Journal of geophysical research: solid earth 108(B2)

Blewitt G, Lavallée D, Clarke P, Nurutdinov K (2001) A New Global Mode of Earth Deformation: Seasonal Cycle Detected. Science 294(5550):2342–2345, DOI 10.1126/science.1065328

Bock H (2003) Efficient methods for determining precise orbits of low Earth orbiters using the Global Positioning System. PhD thesis, Astronomical In-stitute, University of Berne, Berne

Bury G, Zajdel R, Sośnica K (2019) Accounting for perturbing forces acting on Galileo using a box-wing model. GPS Solut 23(3):74, DOI 10.1007/s10291-019-0860-0

Bury G, Sośnica K, Zajdel R, Strugarek D, Hugentobler U (2020) Determination of precise Galileo orbits using combined GNSS and SLR observations. GPS Solutions 25(1):1–13, DOI 10.1007/s10291-020-01045-3

Cardellach E, Elósegui P, Davis JL (2007) Global distortion of GPS networks associated with satellite antenna model errors. Journal of Geophysical Research: Solid Earth 112(7):1–13, DOI 10.1029/2006JB004675

Case K, Kruizinga G, Wu S (2002) Grace level 1b data product user handbook. Tech. rep., JPL

Cerri L, Ferrage P (2015) DORIS satellites models implemented in POE processing. Tech. rep., CNES document Ref: SALP-NT-BORD-OP-16137-CN

Charlot P, Jacobs C, Gordon D, Lambert S, de Witt A, Böhm J, Fey A, Heinkelmann R, Skurikhina E, Titov O, et al. (2020) The third realization of the International Celestial Reference Frame by very long baseline interferometry. Astronomy & Astrophysics 644:A159

Chen J (2007) On precise orbit determination of low earth orbiters. Tongji University, ShangHai 17:234

Chen J, Wilson C, Eanes R, Nerem R (1999) Geophysical interpretation of observed geocenter variations. Journal of geophysical research: solid earth 104(B2):2683–2690

Choi K (2014) Status of Core Products of the International GNSS Service. In: American Geophysical Union, Fall Meeting 2014, abstract id. G21A-0426

Couderc V (2015) Jason-3 characteristics for POD processing. Tech. rep., CNES

Coulot D, Berio P, Biancale R, Loyer S, Soudarin L, Gontier AM (2007) Toward a direct combination of space-geodetic techniques at the measurement level: Methodology and main issues. Journal of Geophysical Research: Solid Earth 112(B5), DOI https://doi.org/10.1029/2006JB004336

Dach R, Sušnik A, Grahsl A, Villiger A, Schaer S, Arnold D, Prange L, Jäggi A (2019) Improving GLONASS orbit quality by re-estimating satellite antenna offsets. Advances in Space Research 63(12):3835–3847, DOI 10.1016/j.asr.2019.02.031

Deng Z, Fritsche M, Nischan T, Bradke M (2016) Multi-GNSS ultra rapid orbit-, clock-& EOP-product series. GFZ Data Services DOI 10.5880/GFZ.1.1.2016.003

Dilssner F, Michiel O, Tim S, Claudia F, Drazen S, Zandbergen R (2011) GPS satellite antenna parameters from combined ground-based and space-borne data processing. In: EGU General Assembly Conference Abstracts, vol 13, p 12263

Dong D, Dickey J, Chao Y, Cheng M (1997) Geocenter variations caused by atmosphere, ocean and surface ground water. Geophysical research letters 24(15):1867–1870

Dong D, Yunck T, Heflin M (2003) Origin of the international terrestrial reference frame. Journal of geophysical research: solid earth 108(B4)

Dumont J, Rosmorduc V, Picot N, Desai S, Bonekamp H, Figa J, Lillibridge J, Scharroo R (2009) Ostm/jason-2 products handbook. Tech. rep., CNES and EUMETSAT and JPL and NOAA/NESDIS

Dumont J, Rosmorduc V, Carrere L, Picot N, Bronner E, Couhert A, Guillot A, Desai S, Bonekamp H, Figa J, et al. (2016) Jason-3 products handbook. Tech. rep., CNES and EUMETSAT and JPL and NOAA/NESDIS

Feissel M, Mignard F (1998) The adoption of ICRS on 1 January 1998: meaning and consequences. Astronomy and Astrophysics 331:L33–L36

Friis-Christensen E, Lühr H, Hulot G (2006) Swarm: A constellation to study the Earth's magnetic field. Earth, planets and space 58(4):351–358, DOI 10.1186/BF03351933

Fu LL, Christensen EJ, Yamarone CA, Lefebvre M, Menard Y, Dorrer M, Escudier P (1994) TOPEX/POSEIDON mission overview. Journal of Geophysical Research: Oceans 99(C12):24369–24381, DOI 10.1029/94JC01761

Ge H, Li B, Ge M, Zang N, Nie L, Shen Y, Schuh H (2018) Initial assessment of precise point positioning with LEO enhanced Global Navigation Satellite Systems (LeGNSS). Remote Sens 10(7), DOI 10.3390/rs10070984

Ge M, Gendt G, Dick G, Zhang P, Reigber C (2005) Impact of GPS satellite antenna offsets on scale changes in global network solutions. Geophysical Research Letters 32(6):L06310, DOI 10.1029/2004GL022224

Geng JH, Shi C, Zhao QL, Ge MR, Liu JN (2008) Integrated adjustment of LEO and GPS in precision orbit determination. International Association of Geodesy Symposia 132:133–137, DOI 10.1007/978-3-540-74584-6_20

Giorgi G, Schmidt TD, Trainotti C, Mata-Calvo R, Fuchs C, Hoque MM, Berdermann J, Furthner J, Günther C, Schuldt T, et al. (2019) Advanced technologies for satellite navigation and geodesy. Advances in Space Research 64(6):1256–1273, DOI 10.1016/j.asr.2019.06.01

Glaser S, Michalak G, Männel B, König R, Neumayer K, Schuh H (2020) Reference system origin and scale realization within the future GNSS constellation "Kepler". Submitted to Journal of Geodesy

Guo X, Geng J, Chen X, Zhao Q (2020) Enhanced orbit determination for formation-flying satellites through integrated single- and double-difference GPS ambiguity resolution. GPS Solutions 24(1):14, DOI 10.1007/s10291-019-0932-1, URL `http://link.springer.com/10.1007/s10291-019-0932-1`, publisher: Springer

Gutierrez P (2018) Brexit and Galileo - Plenty of Rumblings, but Where's the Beef? Online article on insidegnss.com

Hackel S, Steigenberger P, Hugentobler U, Uhlemann M, Montenbruck O (2015) Galileo orbit determination using combined GNSS and SLR observations. GPS Solutions 19(1):15–25, DOI 10.1007/s10291-013-0361-5

Haines B, Bar-Sever Y, Bertiger W, Desai S, Willis P (2004) One-centimeter orbit determination for Jason-1: New GPS-based strategies. Marine Geodesy DOI 10.1080/01490410490465300

Haines BJ, Bar-Sever YE, Bertiger WI, Desai SD, Harvey N, Sibois AE, Weiss JP (2015) Realizing a terrestrial reference frame using the Global Positioning System. Journal of Geophysical Research: Solid Earth 120(8):5911–5939, DOI 10.1002/2015JB012225

Heflin M, Jefferson D, Zumberge J, Webb F, Argus D (2002) Comparison of a GPS-defined global reference frame with ITRF2000. GPS Solutions 6(1-2):72–75, DOI 10.1007/s10291-002-0015-5

Huang W, Männel B, Sakic P, Ge M, Schuh H (2020) Integrated processing of ground- and space-based GPS observations: improving GPS satellite orbits observed with sparse ground networks. Journal of Geodesy 94(10):1–13, DOI 10.1007/s00190-020-01424-1

Huang W, Männel B, Brack A, Schuh H (2021) Two methods to determine scale-independent GPS PCOs and GNSS-based terrestrial scale: comparison and cross-check. GPS Solutions 25(1):4, DOI 10.1007/s10291-020-01035-5

van den IJssel J, Encarnação J, Doornbos E, Visser P (2015) Precise science orbits for the Swarm satellite constellation. Adv Sp Res 56(6):1042–1055, DOI 10.1016/J.ASR.2015.06.002

International GNSS Service (2020) GNSS Final Combined Orbit Solution Product. USA:NASA Crustal Dynamics Data Information System (CDDIS), DOI 10.5067/gnss/gnss_igsorb_001, accessed in 2020

Jäggi A, Hugentobler U, Bock H, Beutler G (2007) Precise orbit determination for GRACE using undifferenced or doubly differenced GPS data. Advances in Space Research 39(10):1612–1619, DOI 10.1016/j.asr.2007.03.012

Jäggi A, Dach R, Montenbruck O, Hugentobler U, Bock H, Beutler G (2009) Phase center modeling for LEO GPS receiver antennas and its impact on precise orbit determination. Journal of Geodesy 83(12):1145–1162, DOI 10.1007/s00190-009-0333-2

Jäggi A, Dach R, Bock H, Beutler G, Montenbruck O, Steigenberger P, Andres Y (2011) Combining terrestrial & LEO data to extend the GPS satellite antenna patterns to

nadir angles beyond 14 degree. Presentation at AGU Fall Meeting 2011, San Francisco, California.

Jäggi A, Dahle C, Arnold D, Bock H, Meyer U, Beutler G, van den IJssel J (2016) Swarm kinematic orbits and gravity fields from 18 months of GPS data. Adv Sp Res 57(1):218–233, DOI 10.1016/j.asr.2015.10.035

Johnston G, Neilan R, Craddock A, Dach R, Meertens C, Rizos C (2018) The International GNSS Service 2018 Update. In: EGU General Assembly Conference Abstracts, vol 20, p 19675

Kang Z, Tapley B, Bettadpur S, Ries J, Nagel P, Pastor R (2006) Precise orbit determination for the GRACE mission using only GPS data. J Geod 80(6):322–331, DOI 10.1007/s00190-006-0073-5

Katsigianni G, Loyer S, Perosanz F, Mercier F, Zajdel R, Sośnica K (2019) Improving Galileo orbit determination using zero-difference ambiguity fixing in a Multi-GNSS processing. Advances in Space Research 63(9):2952–2963, DOI 10.1016/j.asr.2018.08.035

Kodet J, Schreiber KU, Eckl J, Plötz C, Mähler S, Schüler T, Klügel T, Riepl S (2018) Co-location of space geodetic techniques carried out at the Geodetic Observatory Wettzell using a closure in time and a multi-technique reference target. Journal of Geodesy 92(9):1097–1112, DOI 10.1007/s00190-017-1105-z

König R, Reigber C, Zhu S (2005) Dynamic model orbits and Earth system parameters from combined GPS and LEO data. Advances in Space Research 36(3):431–437, DOI 10.1016/J.ASR.2005.03.064

Kornfeld RP, Arnold BW, Gross MA, Dahya NT, Klipstein WM, Gath PF, Bettadpur S (2019) GRACE-FO: the gravity recovery and climate experiment follow-on mission. Journal of Spacecraft and Rockets 56(3):931–951, DOI 10.2514/1.A34326

Kuang D, Bar-Sever Y, Haines B (2015) Analysis of orbital configurations for geocenter determination with GPS and low-Earth orbiters. Journal of Geodesy 89(5):471–481, DOI 10.1007/s00190-015-0792-6

Lambin J, Morrow R, Fu LL, Willis JK, Bonekamp H, Lillibridge J, Perbos J, Zaouche G, Vaze P, Bannoura W, Parisot F, Thouvenot E, Coutin-Faye S, Lindstrom E, Mignogno M (2010) The OSTM/Jason-2 Mission. Marine Geodesy DOI 10.1080/01490419.2010.491030

Lavallée DA, Van Dam T, Blewitt G, Clarke PJ (2006) Geocenter motions from GPS: A unified observation model. Journal of geophysical research: solid earth 111(B5)

Li B, Ge H, Ge M, Nie L, Shen Y, Schuh H (2018a) LEO enhanced Global Navigation Satellite System (LeGNSS) for real-time precise positioning services. Adv Sp Res DOI 10.1016/j.asr.2018.08.017

Li X, Ma F, Li X, Lv H, Bian L, Jiang Z, Zhang X (2018b) LEO constellation-augmented multi-GNSS for rapid PPP convergence. J Geod 93(5):749–764, DOI 10.1007/s00190-018-1195-2

Li X, Yuan Y, Huang J, Zhu Y, Wu J, Xiong Y, Li X, Zhang K (2019a) Galileo and QZSS precise orbit and clock determination using new satellite metadata. J Geod 93(8):1123–1136, DOI 10.1007/s00190-019-01230-4

Li X, Zhang K, Ma F, Zhang W, Zhang Q, Qin Y, Zhang H, Meng Y, Bian L (2019b) Integrated precise orbit determination of multi- GNSS and Large LEO constellations. Remote Sens 11(21), DOI 10.3390/rs11212514

Liu J, Ge M (2003) PANDA software and its preliminary result of positioning and orbit determination. Wuhan University Journal of Natural Sciences 8(2):603–609, DOI 10.1007/BF02899825

Liu M, Yuan Y, Ou J, Chai Y (2019) Research on attitude models and antenna phase center correction for jason-3 satellite orbit determination. Sensors (Switzerland) 19(10), DOI 10.3390/s19102408

Luceri V, Pirri M, Rodríguez J, Appleby G, Pavlis E, Müller H (2019) Systematic errors in SLR data and their impact on the ILRS products. Journal of Geodesy 93(11):2357–2366, DOI 10.1007/s00190-019-01319-w

Luthcke S, Zelensky N, Rowlands D, Lemoine F, Williams T (2003) The 1-centimeter orbit: Jason-1 precision orbit determination using GPS, SLR, DORIS, and altimeter data special issue: Jason-1 calibration/validation. Marine Geodesy 26(3-4):399–421, DOI 10.1080/714044529

Lyard F, Lefevre F, Letellier T, Francis O (2006) Modelling the global ocean tides: modern insights from FES2004. Ocean Dynamics 56(5-6):394–415, DOI 10.1007/s10236-006-0086-x

Ma C, Arias E, Eubanks T, Fey A, Gontier AM, Jacobs C, Sovers O, Archinal B, Charlot P (1998) The international celestial reference frame as realized by very long baseline interferometry. The Astronomical Journal 116(1):516

Malla RP, Wu SC (1989) GPS inferred geocentric reference frame for satellite positioning and navigation. Bulletin Géodésique 63(3):263–279, DOI 10.1007/BF02520476

Malys S (2012) NGA's Relationship with GPS. Tech. rep., NATIONAL GEOSPATIAL-INTELLIGENCE AGENCY SPRINGFIELD VA, URL `https://apps.dtic.mil/dtic/tr/fulltext/u2/a606522.pdf`

Männel B (2016) Co-location of Geodetic Observation Techniques in Space. PhD thesis, ETH Zurich, DOI 10.3929/ethz-a-010811791

Männel B, Rothacher M (2017) Geocenter variations derived from a combined processing of LEO- and ground-based GPS observations. Journal of Geodesy 91(8):933–944, DOI 10.1007/s00190-017-0997-y

Männel B, Brandt A, Bradke M, Sakic P, Brack A, Nischan T (2020) Status of IGS Reprocessing Activities at GFZ. In: Int. Assoc. Geod. Symp., Springer, Berlin, Heidelberg, pp 1–7, DOI 10.1007/1345_2020_98

Mao X, Visser PN, van den IJssel J (2019) Absolute and relative orbit determination for the CHAMP/GRACE constellation. Adv Sp Res DOI 10.1016/j.asr.2019.02.030

Marquis WA, Reigh DL (2015) The GPS Block IIR and IIR-M Broadcast L-band Antenna Panel: Its Pattern and Performance. Navigation: Journal of The Institute of Navigation 62(4):329–347, DOI 10.1002/navi.123

Marshall JA, Antreasian PG, Rosborough GW, Putney BH (1992) Modeling radiation forces acting on satellites for precision orbit determination. Advances in the Astronautical Sciences 76(pt 1):73–96, DOI 10.2514/3.26408

Meindl M, Beutler G, Thaller D, Dach R, Jäggi A (2013) Geocenter coordinates estimated from GNSS data as viewed by perturbation theory. Advances in Space Research 51(7):1047 – 1064, DOI https://doi.org/10.1016/j.asr.2012.10.026

Ménard Y, Fu LL, Escudier P, Parisot F, Perbos J, Vincent P, Desai S, Haines B, Kunstmann G (2003) The Jason-1 mission special issue: Jason-1 calibration/validation. Marine Geodesy 26(3-4):131–146, DOI 10.1080/714044514

Menshikov V, Solovyev G (2006) Global navigation satellite system (GLONASS). Van Nostrand's Scientific Encyclopedia DOI 10.1002/0471743984.vse8616

Montenbruck O, Gill E (2000) Satellite Orbits: Models, Methods, and Applications, 1st edn. Springer-Verlag Berlin Heidelberg, DOI 10.1007/978-3-642-58351-3

Montenbruck O, Van Helleputte T, Kroes R, Gill E (2005) Reduced dynamic orbit determination using GPS code and carrier measurements. Aerosp Sci Technol 9(3):261–271, DOI 10.1016/j.ast.2005.01.003

Montenbruck O, Garcia-Fernandez M, Yoon Y, Schön S, Jäggi A (2009) Antenna phase center calibration for precise positioning of LEO satellites. GPS Solutions 13(1):23–34, DOI 10.1007/s10291-008-0094-z

Montenbruck O, Steigenberger P, Hugentobler U (2015) Enhanced solar radiation pressure modeling for Galileo satellites. Journal of Geodesy 89(3):283–297, DOI 10.1007/s00190-014-0774-0

Montenbruck O, Hackel S, van den Ijssel J, Arnold D (2018) Reduced dynamic and kinematic precise orbit determination for the Swarm mission from 4 years of GPS tracking. GPS Solutions 22(3):79, DOI 10.1007/s10291-018-0746-6

Mozo A (2018) Receiver issues tracking Galileo SVIDs above 32. URL `https://lists.igs.org/pipermail/igsmail/2018/007675.html`, released in IGS Mail List: IGSMAIL-7679

Nothnagel A, Angermann D, Börger K, Dietrich R, Drewes H, Görres B, Hugentobler U, Ihde J, Müller J, Oberst J, et al. (2010) Space-time reference systems for monitoring global change and for precise navigation. Verlag des Bundesamtes für Kartographie und Geodäsie

Olsen PEH (2019) Swarm l1b product definition. Tech. rep., National Space Institute Technical University of Denmark

Otten M, Flohrer C, Springer T, Enderle W (2012) Multi-technique combination at observation level with NAPEOS: combining GPS, GLONASS and LEO satellites. In: EGU General Assembly Conference Abstracts, vol 14, p 7925

Pearlman MR, Degnan JJ, Bosworth JM (2002) The international laser ranging service. Advances in Space Research 30(2):135–143, DOI 10.1016/S0273-1177(02)00277-6

Petit G, Luzum B (2010) IERS conventions (2010). Tech. rep., Bureau international des poids et mesures sevres (France)

Plag HP, Pearlman M (eds) (2009) Global Geodetic Observing System. Springer-Verlag Berlin Heidelberg, DOI 10.1007/978-3-642-02687-4

Ramsey F, Ziebart M (2020) OneWeb LEO PNT: Progress or Risky Gamble? Insid GNSS

Rebischung P (2019) Possible contribution of GNSS to the definition of the ITRF2020 scale based on the Galileo satellite PCOs. URL http://www.ggos.org/media/filer_public/53/d8/53d8ed8e-d3c2-4dbd-9de8-babda253bdda/uaw_gnss_2b-rebischung_gnssorbitmodeling.pdf, Presentation at Unified Analysis Workshop , 2019, October, Paris.

Rebischung P, Schmid R (2016) IGS14/igs14.atx: a new framework for the IGS products. URL https://mediatum.ub.tum.de/doc/1341338/file.pdf, Presentation at AGU Fall Meeting, 2016, December, San Francisco, California.

Rebischung P, Griffiths J, Ray J, Schmid R, Collilieux X, Garayt B (2012) IGS08: the IGS realization of ITRF2008. GPS Solutions 16(4):483–494, DOI 10.1007/s10291-011-0248-2

Reigber C, Schmidt R, Flechtner F, König R, Meyer U, Neumayer KH, Schwintzer P, Zhu SY (2005) An earth gravity field model complete to degree and order 150 from grace: Eigen-grace02s. Journal of Geodynamics 39(1):1–10, DOI 10.1016/j.jog.2004.07.001

Ren L, Schön S (2018) PPP-based Swarm kinematic orbit determination. Ann Geophys 36(5):1227–1241, DOI 10.5194/angeo-36-1227-2018

Rodriguez-Solano J Carlos (2009) Impact of Albedo modelling in GPS orbits. Masterarbeit, Technische Universität München, München

Rothacher M (1992) Orbits of satellite systems in space geodesy. Geod.-Geophys. Arb. Schweiz, Vol. 46

Rülke A, Dietrich R, Fritsche M, Rothacher M, Steigenberger P (2008) Realization of the Terrestrial Reference System by a reprocessed global GPS network. Journal of Geophysical Research: Solid Earth 113(B8), DOI 10.1029/2007JB005231

Schlüter W, Behrend D (2007) The International VLBI Service for Geodesy and Astrometry (IVS): current capabilities and future prospects. Journal of Geodesy 81(6-8):379–387, DOI 10.1007/s00190-006-0131-z

Schmid R (2009) Zur Kombination von VLBI und GNSS. PhD thesis, Technische Universität München

Schmid R, Rothacher M (2003) Estimation of elevation-dependent satellite antenna phase center variations of GPS satellites. Journal of Geodesy 77(7-8):440–446, DOI 10.1007/s00190-003-0339-0

Schmid R, Rothacher M, Thaller D, Steigenberger P (2005) Absolute phase center corrections of satellite and receiver antennas. Impact on global GPS solutions and estimation of azimuthal phase center variations of the satellite antenna Received:. GPS Solutions 9(4):283–293, DOI 10.1007/s10291-005-0134-x

Schmid R, Steigenberger P, Gendt G, Ge M, Rothacher M (2007) Generation of a consistent absolute phase-center correction model for GPS receiver and satellite antennas. Journal of Geodesy 81(12):781–798, DOI 10.1007/s00190-007-0148-y

Schmid R, Dach R, Collilieux X, Jäggi A, Schmitz M, Dilssner F (2016) Absolute IGS antenna phase center model igs08.atx: status and potential improvements. Journal of Geodesy 90(4):343–364, DOI 10.1007/s00190-015-0876-3

Seitz M, Bloßfeld M, Angermann D, Schmid R, Gerstl M, Seitz F (2016) The new DGFI-TUM realization of the ITRS: DTRF2014 (data). DOI 10.1594/PANGAEA.864046

Sieg D, Diekmann F (2016) Options for the further orbit evolution of the Swarm mission. ESASP 740:278

Siemes C (2019) Swarm instrument positions related to GPS receiver data processing. Tech. rep., RHEA for ESA - European Space Agency, personal contact

Springer T, Beutler G, Rothacher M (1999) A new solar radiation pressure model for GPS satellites. GPS solutions 2(3):50–62, DOI 10.1007/PL00012757

Standish EM (1998) JPL planetary and lunar ephemerides, DE405/LE405. Jpl Iom 312F - 98 - 048

Steigenberger P, Fritsche M, Dach R, Schmid R, Montenbruck O, Uhlemann M, Prange L (2016) Estimation of satellite antenna phase center offsets for Galileo. Journal of Geodesy 90(8):773–785, DOI 10.1007/s00190-016-0909-6

Stupak G (2012) SDCM status and plans. In: Seventh Meeting of the International Committee on GNSS Beijing, URL `https://www.unoosa.org/pdf/icg/2012/icg-7/3-2.pdf`

Švehla D, Rothacher M (2003) Kinematic and reduced-dynamic precise orbit determination of low earth orbiters. Advances in Geosciences 1:47–56, DOI 10.5194/adgeo-1-47-2003

Švehla D, Rothacher M (2005a) Kinematic positioning of LEO and GPS satellites and IGS stations on the ground. Advances in Space Research 36(3):376–381, DOI 10.1016/j.asr.2005.04.066

Švehla D, Rothacher M (2005b) Kinematic precise orbit determination for gravity field determination. In: Int. Assoc. Geod. Symp., Springer Verlag, vol 128, pp 181–188, DOI 10.1007/3-540-27432-4_32

Tapley BD, Bettadpur S, Ries JC, Thompson PF, Watkins MM (2004) GRACE measurements of mass variability in the Earth system. Science DOI 10.1126/science.1099192

Teunissen P, Montenbruck O (2017) Springer handbook of global navigation satellite systems. Springer, DOI 10.1007/978-3-319-42928-1

Thaller D (2008) Inter-technique combination based on homogeneous normal equation systems including station coordinates, Earth orientation and troposphere parameters. PhD thesis, Technische Universität München

Vaze P, Neeck S, Bannoura W, Green J, Wade A, Mignogno M, Zaouche G, Couderc V, Thouvenot E, Parisot F (2010) The Jason-3 Mission: Completing the transition of ocean altimetry from research to operations. In: Sensors, Systems, and Next-Generation Satellites XIV, International Society for Optics and Photonics, vol 7826, p 78260Y

Villiger A (2019) IGS ANTEX file for repro 3. Released in IGS Analysis Centers Mail List: IGS-ACS-1233., URL `https://lists.igs.org/mailman/listinfo/igs-acs`

Villiger A, Dach R, Schaer S, Prange L, Zimmermann F, Kuhlmann H, Wübbena G, Schmitz M, Beutler G, Jäggi A (2020) GNSS scale determination using calibrated receiver and Galileo satellite antenna patterns. Journal of geodesy 94(9):1–13, DOI 10.1007/s00190-020-01417-0

Wang L, Zhang Q, Huang G, Yan X, Qin Z (2016) Combining Regional Monitoring Stations with Space-based Data to Determine the MEO Satellite Orbit. Acta Geodaetica et Cartographica Sinica 45(S2), DOI 10.11947/j.AGCS.2016.F031

Willis P, Fagard H, Ferrage P, Lemoine FG, Noll CE, Noomen R, Otten M, Ries JC, Rothacher M, Soudarin L, et al. (2010) The international DORIS service (IDS): toward maturity. Advances in space research 45(12):1408–1420

Wu SC, Yunck TP, Thornton CL (1991) Reduced-dynamic technique for precise orbit determination of low earth satellites. Journal of Guidance, Control, and Dynamics 14(1):24–30, DOI 10.2514/3.20600

Wu X, Ray J, van Dam T (2012) Geocenter motion and its geodetic and geophysical implications. Journal of Geodynamics 58:44–61

Wübbena G, Schmitz M, Menge F, Böder V, Seeber G (2000) Automated absolute field calibration of GPS antennas in real-time. In: ION GPS, vol 2000, pp 2512–2522

Wübbena G, Schmitz M, Garbsen D, Mader G, Spring S (2007) GPS Block II / IIA Satellite Antenna Testing using the Automated Absolute Field Calibration with Robot. In: ION-GNSS07, Fort Worth, pp 1236–1243

Zajdel R, Sośnica K, Dach R, Bury G, Prange L, Jäggi A (2019) Network Effects and Handling of the Geocenter Motion in Multi-GNSS Processing. Journal of Geophysical Research: Solid Earth 124(6):5970–5989

Zajdel R, Sośnica K, Bury G (2021) Geocenter coordinates derived from multi-GNSS: a look into the role of solar radiation pressure modeling. GPS Solutions 25(1):1–15

Zhao Q, Wang C, Guo J, Yang G, Liao M, Ma H, Liu J (2017) Enhanced orbit determination for BeiDou satellites with FengYun-3C onboard GNSS data. GPS Solutions 21(3):1179–1190, DOI 10.1007/s10291-017-0604-y

Zhao Q, Wang C, Guo J, Wang B, Liu J (2018) Precise orbit and clock determination for BeiDou-3 experimental satellites with yaw attitude analysis. GPS Solutions 22(1):4, DOI 10.1007/s10291-017-0673-y

Zhu S, Reigber C, König R (2004) Integrated adjustment of CHAMP, GRACE, and GPS data. Journal of Geodesy 78(1-2):103–108, DOI 10.1007/s00190-004-0379-0

Zhu SY, Massmann FH, Yu Y, Reigber C (2003) Satellite antenna phase center offsets and scale errors in GPS solutions. Journal of Geodesy 76(11-12):668–672, DOI 10.1007/s00190-002-0294-1

Zoulida M, Pollet A, Coulot D, Perosanz F, Loyer S, Biancale R, Rebischung P (2016) Multi-technique combination of space geodesy observations: Impact of the Jason-2 satellite on the GPS satellite orbits estimation. Advances in Space Research 58(7):1376–1389, DOI 10.1016/j.asr.2016.06.019

Appendix

Table 1: Estimated GPS PCOs in three directions in Section 5.4. The processing period is from day 115 to 365 in 2016. The data from 54 IGS stations is used. GRACE-A/B, OSTM/Jason-2, Jason-3 and Swarm-A/B/C satellites are integrated to the processing (minimum four LEOs used per day). The scale-free condition is applied to the ground stations for z-PCO estimation. The PCOs are formal-error-based weighted mean values over all processing days. PCO-z corrections with respect to *IGS08_1930.atx* and the solution given by Rebischung (2019) are listed in the last two columns as references.

Block	SVN	PRN	PCO-x [mm]	PCO-y [mm]	PCO-z [mm] estimated	PCO-z [mm] w.r.t. *IGS08_1930.atx*	PCO-z [mm] w.r.t. Rebischung (2019)
IIR-A	G041	G14	17.76	4.03	1015.16	−330.24	−129.34
IIR-A	G043	G13	13.87	−2.68	1116.44	−273.05	−71.86
IIR-A	G044	G28	19.02	12.70	820.39	−222.40	−19.11
IIR-A	G045	G21	34.34	3.91	1150.43	−254.97	−48.67
IIR-A	G046	G11	−15.66	−15.60	918.86	−222.43	−38.94
IIR-A	G051	G20	33.88	4.45	1083.46	−260.13	−70.04
IIR-A	G054	G18	45.23	−28.72	1019.61	−271.29	−68.99
IIR-A	G056	G16	40.89	−29.61	1188.59	−317.81	−120.11
IIR-B	G047	G22	35.19	−22.39	620.95	−284.84	−69.65
IIR-B	G059	G19	28.73	−24.36	514.81	−334.79	−133.39
IIR-B	G060	G23	35.48	−21.52	606.74	−201.46	0.64
IIR-B	G061	G02	35.48	−23.56	558.95	−219.64	−9.85
IIR-M	G048	G07	24.43	−20.97	705.60	−147.29	43.20
IIR-M	G050	G05	31.43	−21.19	651.22	−171.38	33.22
IIR-M	G052	G31	23.25	−20.69	708.28	−263.12	−44.22
IIR-M	G053	G17	19.49	−24.63	586.67	−240.43	−24.23
IIR-M	G055	G15	27.35	−23.31	533.07	−148.02	70.27
IIR-M	G057	G29	28.39	−28.44	622.48	−234.62	−9.32
IIR-M	G058	G12	31.55	−29.03	543.66	−297.14	−64.14
IIF	G062	G25	386.11	−223.90	1314.02	−283.28	−43.38
IIF	G063	G01	390.11	−220.90	1308.89	−252.40	−32.91
IIF	G064	G30	394.47	−233.30	1388.17	−211.82	26.07
IIF	G065	G24	395.68	−228.80	1298.76	−301.24	51.66
IIF	G066	G27	392.83	−213.94	1369.65	−230.34	7.35
IIF	G067	G06	393.33	−217.73	1299.23	−300.77	−7.77
IIF	G068	G09	388.03	−213.33	1325.04	−274.96	−37.56
IIF	G069	G03	395.68	−231.07	1287.30	−312.70	−103.30
IIF	G070	G32	398.65	−211.49	1302.50	−297.50	−72.30
IIF	G071	G26	404.65	−226.53	1347.66	−252.33	4.16
IIF	G072	G08	394.09	−221.57	1390.92	−209.07	49.52
IIF	G073	G10	392.36	−228.18	1319.93	−280.06	−35.17